



Universiteit
Leiden
The Netherlands

The physics of nanowire superconducting single-photon detectors

Renema, J.J.

Citation

Renema, J. J. (2015, March 5). *The physics of nanowire superconducting single-photon detectors*. *Casimir PhD Series*. Retrieved from <https://hdl.handle.net/1887/32149>

Version: Not Applicable (or Unknown)

License: [Leiden University Non-exclusive license](#)

Downloaded from: <https://hdl.handle.net/1887/32149>

Note: To cite this publication please use the final published version (if applicable).

Cover Page



Universiteit Leiden



The handle <http://hdl.handle.net/1887/32149> holds various files of this Leiden University dissertation.

Author: Renema, Jelmer Jan

Title: The physics of nanowire superconducting single-photon detectors

Issue Date: 2015-03-05

The Physics of Nanowire Superconducting Single-Photon Detectors

Jelmer Jan Renema

Casimir PhD series, Delft-Leiden 2015-02
ISBN 978-90-8593-210-9

An electronic version of this thesis can be found at <https://openaccess.leidenuniv.nl>
The work described in this thesis is part of the research programme of the
Foundation for Fundamental Research on Matter (FOM), which is part of
the Netherlands Organisation for Scientific Research (NWO).
Cover design by Sybren Renema. Image by Döndü Sahin.

The Physics of Nanowire Superconducting Single-Photon Detectors

Proefschrift

ter verkrijging van
de graad van Doctor aan de Universiteit Leiden,
op gezag van Rector Magnificus prof. mr. C.J.J.M. Stolker,
volgens besluit van het College voor Promoties
te verdedigen op donderdag 5 maart 2015
klokke 15:00 uur

door

Jelmer Jan Renema

Geboren te Hoogeveen
in 1986

Promotiecommissie

Promotores: Prof. dr. D. Bouwmeester
Prof. dr. A. Fiore (TU/E)

Co-promotor: Dr. M.P. van Exter

Overige leden: Prof. dr. G.N. Goltsman (MSPU, Moskou, Rusland)
Prof. dr. ir. T.M. Klapwijk (TU Delft)
Dr. J.S. Lundeen (University of Ottawa, Ottawa, Canada)
Prof. dr. E.R. Eliel
Prof. dr. J. Aarts
Dr. M.J.A. de Dood

To my parents and grandparents

Contents

1	Introduction	1
1.1	Superconducting Single-Photon Detectors	1
1.2	Detector Physics of SSPDs	3
1.3	Experimental Techniques	10
2	Modified Detector Tomography Technique Applied to a Superconducting Multiphoton Nanodetector	15
2.1	Introduction	15
2.2	NbN Nanodetectors	17
2.3	Experimental Setup	18
2.4	Effective Photon Detector Characterization	18
2.5	Result	20
2.6	Discussion	21
2.7	Conclusion	23
3	Universal Response Curve for Nanowire Superconducting Single-Photon Detectors	25
3.1	Introduction	25
3.2	Experiment	26
3.3	Tomography of Multiphoton Excitations	27
3.4	Results	29
3.5	Discussion	32
3.6	Conclusion	35
3.i	Appendix: Comparison of Experimental Data with Detection Models	36
4	Experimental Test of the Detection Models in Nanowire Superconducting Single-Photon Detectors	37
4.1	Introduction	37
4.2	Experiment	39
4.3	Results and Discussion	40
4.4	Conclusion	46
4.i	Appendix: Supplementary Material	47

4.ii	Appendix: Wavelength Measurements with an SSPD	54
5	Position-Dependent Internal Detection Probability in a Nanowire Superconducting Single-Photon Detector	59
5.1	Introduction	59
5.2	Experiment	60
5.3	Results	63
5.4	Comparison to Theory	66
5.5	Discussion and Conclusion	68
5.i	Appendix: Supplementary Material	69
5.ii	Appendix: Implications of the Position Dependence of the Threshold Current of SSPDs	86
6	The Effect of Magnetic Field on the Intrinsic Detection Efficiency of Superconducting Single-Photon Detectors	93
6.1	Introduction	94
6.2	Experiment	95
6.3	Results	95
6.4	Comparison to Theory	98
6.5	High-Field Effects	99
6.6	Conclusion and Discussion	102
7	The Size of a Hotspot in Superconducting Single-Photon Detectors	103
7.1	Introduction	103
7.2	Experimental Setup	105
7.3	Theory	106
7.4	Results	107
7.5	Discussion	112
7.6	Conclusion	113
8	Conclusion and Future Work	115
8.1	Summary	115
8.2	Detection Models	117
8.3	Future Work	118
8.4	Conclusion	119
	Samenvatting	121
	Acknowledgements	125
	Curriculum Vitae	127
	List of Publications	129
	List of Symbols and Material Parameters	131

Chapter 1

Introduction

1.1 Superconducting Single-Photon Detectors

Superconducting single-photon detectors [1] are an important technology for photodetection in the near infrared, with a wide range of applications. These detectors consist of a thin layer of superconducting material, which is nanofabricated into a wire. The typical wires which are used in applications are 4 nm thick, 100 nm wide and some tens of μm long, folded in a meander shape. Such photodetectors were first demonstrated at Moscow State Pedagogical University in 2001.

This type of photodetector has many practical advantages [2, 3]. Contrary to semiconductor-based single-photon detectors, the wavelength of photons which can be measured by the detector is not limited to the bandgap of the material but by the thickness and width of the wire, enabling detection of photons of up to 5 μm [4]. The electrical pulses corresponding to

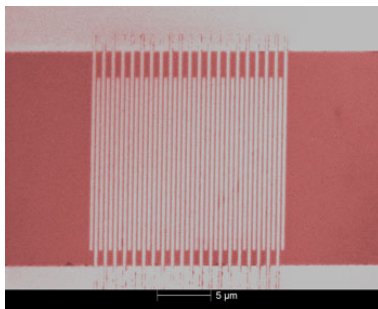


Figure 1.1: Scanning Electron Microscope image of a typical superconducting single-photon detector of the application-oriented meander type. Image courtesy of NIST.

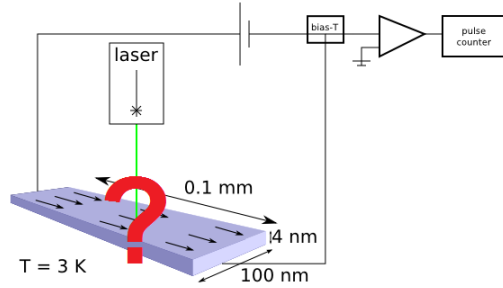


Figure 1.2: The central question of this thesis: what happens at the question mark?

a detection event have a rapidly rising flank with timing jitter in the 20-30 ps range [5], which enables accurate determination of the arrival time of the photon. These properties have many advantages in e.g. deep space communication applications, where bits are coded by the photon arrival time [6]. Moreover, these detectors have a very low dark count rate compared to avalanche photodiodes operating in the same wavelength range, and a fast reset time compared to transition edge sensors. The efficiency of such detectors can be enhanced strongly by embedding the detector inside a cavity [7].

These specifications make SSPDs excellent candidates for many technological and scientific applications. However, the detection mechanism is poorly understood. Though a considerable part of the working mechanism is well understood, much is still unclear about the central part of the detection process, where an absorbed photon is converted into a detection pulse [8].

The well-understood parts of the detection process are as follows: a photon is absorbed into the wire. This creates a cloud of quasiparticles, which obstructs the current flow, leading to a normal cross-section in the wire. This normal cross-section then grows under the influence of Joule heating, producing a voltage pulse [9]. The initial and final parts of this process are well understood: by solving Maxwell's equations for the appropriate geometry, we can investigate the absorption probability into the wire [10, 11, 12, 13]. We also understand the coupled electronic and heat diffusion equations which describe how the normal domain grows [9, 14].

The poorly understood step is how a single photon causes an obstruction across the wire. This thesis deals with that central step of the detection process, where an absorbed photon is converted into an excitation pulse. We investigate this problem by using a combination of three elements in our experiments: quantum detector tomography, multiphoton excitations and a nanodetector (our experimental sample).

The structure of this thesis is as follows: in this introductory chapter, I will set the stage by introducing the four main models of photodetection in superconducting single-photon detectors, as well the experimental techniques

used in this thesis. In Chapter 2, I will demonstrate quantum detector tomography, the main experimental method used throughout most of this thesis, which serves to accurately and completely characterize the response of an SSPD to incoming light pulses. In Chapter 3 and 4, I will apply this technique to investigate the physics of an SSPD. Chapter 3 presents results on SSPD physics which are preparatory for Chapter 4. In Chapter 4, we arrive at the central result of this thesis: we use quantum detector tomography to find which of the models of the detection event in SSPDs conforms to our experimental data.

The rest of the thesis is concerned with investigating various implications of this model. In Chapter 5, we combine experimental data and numerical simulations to investigate the position-dependence of the properties of the detection mechanism at the nanoscale level. Chapter 6 is somewhat separate from the rest of the thesis; in this chapter we investigate the effect of magnetic fields on the detection response. In Chapter 7, we investigate the size of an excitation in the detector using a two-photon technique.

This thesis is structured as a series of scientific papers, some of which have already been published. For articles already in press, we have aimed to keep as close to the original text as possible. In places where insights of earlier papers are expanded upon in later papers, we refer to the future work in footnotes.

1.2 Detector Physics of SSPDs

Discussion about the exact detection mechanism in SSPDs began soon after their invention [15]. Two key questions in the understanding of SSPDs are whether there is a role for a section of normal-state material in the detection event and whether magnetic vortices play a role. In this section, I will introduce the four models of the SSPD detection mechanism. A particularly crucial feature of these models is the *energy-current relation*, which describes the combinations of bias current and photon energy required to produce a detection event. The current required to obtain a detection event with a particular probability is called the threshold current I_{th} . Measurements of the energy-current relation are the primary method of investigation in SSPD detector physics. An excellent, more extended introduction to the various models is given in [16].

1.2.1 Normal-Core Hotspot Model

The earliest attempts to model the detection process in SSPDs focussed on the observation that the energy of the photon rapidly drops to below the level required to make any part of the wire normal after a photon absorption event. Therefore, this model focussed on a small, sharply defined, normal-state disruption of the wire, called a hotspot [1, 15] (see Figure 1.3 a). In

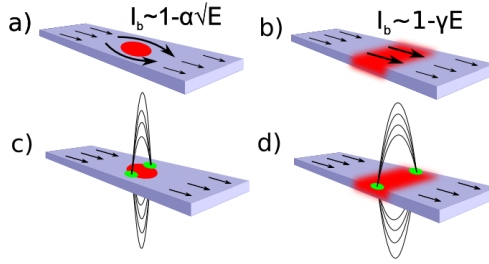


Figure 1.3: Schematic overview of the four main theories of the detection mechanism in SSPDs. (a) In the normal-core hotspot model, the photon energy creates a normal domain inside the superconductor, which the current has to bypass. (b) In the diffusion-based hotspot model, the quasiparticles diffuse outward from the point of absorption, creating a band of depleted superconductivity. (c) In the vortex nucleation model, a vortex-antivortex pair is formed in the hotspot. (d) In the vortex crossing model, either a vortex or a vortex-antivortex pair (pictured) uses an area of weakened superconductivity to cross the wire and annihilate. Picture is not to scale. From [17].

this model, the detection mechanism is as follows: after photon absorption, a normal hotspot forms, and the current is diverted around the hotspot. If the diameter of the hotspot is big enough, the critical current density will be exceeded in the cross-section containing the widest part of the hotspot and a detection event will occur through the suppression of superconductivity across the wire.

This model is essentially based on an area argument: each unit of energy contributes to making the hotspot larger, which serves to increase the diameter of the obstacle that the current must overcome. Since the system is 2D, the size scales as \sqrt{E} , and the energy-current relation is quadratic:

$$E = E_0(1 - I_{th}/I_c)^2, \quad (1.1)$$

where E is the energy of the incident photon, I_{th} is the threshold current, I_c is the critical (depairing) current and E_0 is some energy scale.

1.2.2 Diffusion-Based Hotspot Model

A more sophisticated model was put forward in 2005 by Semenov *et al.* [18], who computed the number of Cooper pairs destroyed by the initial excitation and their subsequent spatial distribution due to diffusion and recombination (see Figure 1.3 b). In this model, there is no role for the normal state in a detection event. Instead, the number of Cooper pairs in a section of the wire with a length equal to the coherence length - called a ξ -slab - is

considered. These Cooper pairs, which are reduced in number compared to the unperturbed superconductor, must still carry the current which was carried by the original number of pairs. Therefore, they must speed up. If the Cooper pairs exceed the critical velocity v_c , they break up and the wire transitions to the normal state.

This model (also called the *refined hotspot model* in literature) consists essentially of counting Cooper pairs: the effect of the presence of quasi-particles on the energy gap is neglected, for example, and all Cooper pairs in the ξ -slab are equivalent. Since the current carrying capacity of the wire is proportional to the number of remaining Cooper pairs, the energy-current relation is therefore of the form:

$$E = E_0(1 - I_{th}/I_c), \quad (1.2)$$

with all quantities having the same interpretation as in equation 1.1. In this model, a precise computation of E_0 is possible, which was found to be [18]:

$$E_0 = (N_0 \Delta^2 w d / \zeta) \sqrt{\pi D \tau}, \quad (1.3)$$

where N_0 is the density of states at the Fermi level, Δ the superconducting energy gap, w the width of the wire, d the thickness, D the diffusion coefficient of the material for quasiparticles and τ the timescale for quasiparticle multiplication. The dimensionless parameter ζ represents the efficiency with which a photon is converted from an initial excitation in the material to quasiparticles at the superconducting band-edge. It captures, for example, losses to the phonon bath. Since the value of this parameter could in principle differ from film to film, it serves essentially as a fit parameter for each set of experimental observations.

This model achieved agreement with the experimental data on some aspects. In particular, the threshold currents computed with this model show reasonable agreement with experimental results. Moreover, equation 1.3 gives direction for experiments on the dependence of the detectable photon energy on various material parameters. However, this model still has limitations. In particular, the combined temperature dependence of equations 1.2 and 1.3 has the wrong sign [8]: if the temperature is increased, the main effect is the decrease of Δ , which would imply a decrease of the energy which can be detected at a constant value of I_b/I_c . This has the interpretation that as the energy of each Cooper pair decreases, a photon of a given energy will break more of them, resulting in a more efficient detection process. However, the opposite trend (i.e. less efficient photodetection at higher temperatures) is consistently observed in experiments.

A further weakness of both the normal-core hotspot model and the diffusion-based hotspot model is that they both predict a deterministic, threshold-like response: the detector responds to all photons of a particular energy, or it doesn't. In contrast, experimentally (see Figure 1.4), it is observed that there is a slow roll-off when the bias current through the device

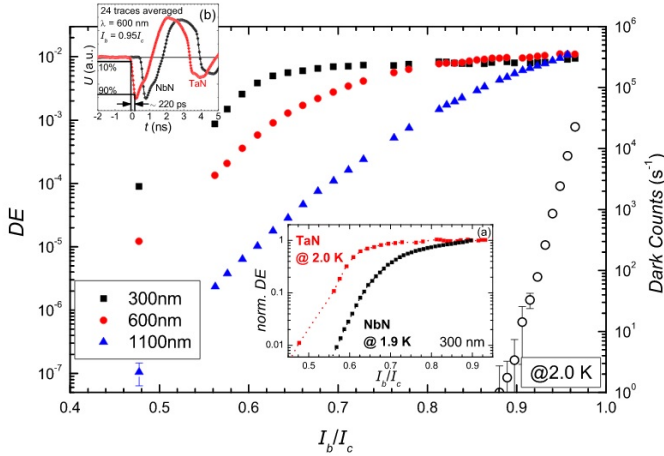


Figure 1.4: Typical count rate curves for an SSPD as a function of the applied bias current (taken from [20] of Engel *et al.*). The graph shows the detection efficiency of a TaN SSPD to three different wavelengths. At short wavelengths, the SSPD response consists of three regimes: a regime where the detection probability is exponential in the applied bias current, followed by an intermediate regime, and then a regime in which the detection probability is more or less independent of applied bias current. As the photon energy is decreased, the transition points between these regimes shift to higher bias current.

is decreased. This points to a regime in which some sort of fluctuation, either thermal or quantum mechanical in nature, occasionally assists in producing a detection event. Magnetic vortices [19] are a natural candidate for this phenomenon. We first give an extremely succinct overview of the physics of vortices in thin films, before returning to the SSPD detection models which contain vortices.

1.2.3 Vortices

Vortices are structures that can occur within a type-II superconductor, i.e. one which has $\lambda > \xi/\sqrt{2}$, with λ the penetration length and ξ the coherence length. These structures encompass a single magnetic flux quantum Φ_0 . They consist of a ring current, which if unobstructed extends over the penetration length λ , as well as a normal-state core, which has a size of the order of the coherence length ξ . Depending on the orientation of the ring current, one speaks of a vortex or an antivortex. Vortices have a magnetic interaction with their environment: vortices of equal orientation repel one another, whereas a vortex and an antivortex attract one another. A

vortex moving through a superconductor experiences friction and therefore dissipates energy into the wire.

For the present discussion, two forces which vortices can experience are relevant. First, vortices respond to the Lorentz force caused by an applied bias current. Second, in narrow wires, vortices experience an attractive force towards the edge of the wire. This is due to the fact that the ring current which surrounds the vortex cannot form without encountering the edge of the wire. In our system, the effective penetration length is different from the bulk value because $d \ll \lambda$, so we have $\Lambda_{\perp} = \lambda^2/d \approx 50 \mu\text{m}$, with λ the bulk magnetic penetration length of 500 nm [21]. Since the width of the wire is typically 100-200 nm, this effect is prominent in our system.

We can find the forces resulting from this effect by considering the method of mirror charges from electrostatics. A charge above a grounded surface is attracted to that surface because of the induced charge on the surface, which we can model as the opposite charge at the point of the mirror image of the original charge. In the same way, we can represent the effects of the boundary conditions on a vortex in a thin wire by considering a mirror-antivortex outside the wire. In the case of a very thin wire, we must also consider the mirror-image of the mirror-image on the other side of the wire, and so on. Summing up all these forces results in an effective attractive force towards the edge of the wire, called an *edge barrier* [22].

1.2.4 Diffusion-Based Vortex Model

In 2008, Semenov *et al.* [23] put forward the notion that vortex-antivortex pairs (VAP) are responsible for the slow roll-off of the detection efficiency at longer wavelengths and lower currents. In 2011, Bulaevskii *et al.* suggested that vortices are responsible for all detection events, including those at high current (see Figure 1.3 d) [24, 25]. In this model, the arrival of the photon decreases the entry barrier for vortices, which enables a vortex crossing. Bulaevskii *et al.* also calculated the current which is required to have sufficient dissipation to cause a transition to the normal state; they showed that this current is much less than the typical operating currents of SSPDs. In this model, the functional dependence of the detection probability R in the regime $R \ll 1$ is of the form [25]:

$$R \propto I_b^{\nu_h+1}, \quad (1.4)$$

where ν_h is a parameter that measures the reduction of the energy barrier for vortex entry to the absorption of a photon. Following [16, 25, 26], we apply the assumption that the energy is divided equally over the area of interest. This results in a value of ν_h of:

$$\nu_h = \nu - 4\pi\zeta E/(k_b T)(\xi/w)^2, \quad (1.5)$$

where $\nu = \varepsilon_0/(k_b T)$ is the value in the absence of photon absorption, which was found to be 40-110 for dark counts [25] and 3-8 for photon counts [26], and $k_b T$ is the Boltzman energy. The two expressions above imply an energy-current relation of the form

$$I/I_0 = \exp(C/(\nu - E/E_0 + 1)), \quad (1.6)$$

with C some constant. For comparison with the other models, this can be cast in an approximate form which is similar to the equations given above [27]:

$$E/E_0 = (1 - (I/I_c)^{4/3}). \quad (1.7)$$

A more advanced version of this model was produced by Engel and Schilling [28], who considered both the vortex physics described above and the diffusion of quasiparticles from the initial absorption spot. The complex nature of the model means that at this point, numerical simulations are the only way to obtain experimentally verifiable results. Engel and Schilling implemented a numerical simulation of quasiparticle diffusion and recombination, as well as current flow, and computed the entry energy for vortices. They showed that in this model, the energy-current relation is linear, i.e. follows equation 1.2. The fact that the energy-current relation depends on the shape of the quasiparticle cloud points - incidentally - to the importance which the quasiparticle distribution has for the detection mechanism.

One crucial difference between the diffusion-based vortex model and the two hotspot models is that the critical current in the vortex model is no longer the depairing current but the current at which vortices unbind from the edge of the wire. This current has a value of approximately $I_c \approx 0.8I_{c,dep}$. Whereas the difference between these currents might seem like a natural way of testing which of the models is correct, unfortunately these two quantities have the same temperature dependence $I \propto 1/t^{3/2}$ [24, 25], with $t \equiv (1 - T/T_c)$, with T the temperature and T_c the critical temperature, which precludes this route¹.

The first version of the diffusion-based vortex model [28] did not implement current continuity; at each cross-section of the device the current density was simply assumed to be locally proportional to the number of available Cooper pairs, normalized in such a way as to have the same current in each cross-section of the device. That is: the current was assumed to go where the Cooper pairs were, which amounts to neglecting the terms in $\partial j/\partial x$, where x is the coordinate along the cross-section of the wire. However, current crowding [29], i.e. the effect that even in a homogeneous wire, the current flows around obstacles in a non-homogeneous way, was known to be a significant effect in SSPDs [30, 31]. Implementing full current continuity as well as suppression of the superconductivity due to the presence

¹Using the Ginzburg-Landau temperature dependence

of a bias current leads to a more complete set of predictions [32], which will be the subject of Chapter 5 of this thesis.

1.2.5 Normal-State Vortex Model

A fourth model was formulated by Zotova and Vodolazov [33] (see Figure 1.3 c), who approached the problem in the context of the time-dependent Ginzburg-Landau equation. The starting point of this study was a normal-core hotspot, around which a vortex antivortex pair forms, which are then driven to the edges of the wire, causing a transition to the normal state in a manner similar to the diffusion-based scenario.

This model was revised several times. In the initial version of this model, the energy-current relation was almost equivalent to that of the normal-state hotspot model. Later [16], a correction term was added which takes into account the fact that the superconductivity inside the hotspot is not entirely suppressed. This produces deviations from the normal-core relation, which flatten the energy-current relation, bringing the model more in line with experimental results. After this, further corrections [34, 35] were added which pertain to the proximity effect induced by the normal-state region into the surrounding superconducting material. With these corrections, the normal-state vortex model predicts an almost linear energy-current relation in the regime which has been accessible to experiments so far.

The normal-state vortex model and the diffusion-based vortex model differ in three crucial aspects. First, in the diffusion-based model, vortices always enter the wire via the sides. In the normal-state model, in contrast, vortices can also enter from the edges of the normal-state hotspot, and it is predicted that for some cases, this is the energetically more favorable route. Secondly in the normal-state vortex model, the critical current of the wire is the depairing current. This means that the energy-current relation contains a strongly nonlinear part at photon energies of the order of a hundred meV, i.e. in the mid-infrared. Neither of these predictions has yet been subjected to experiment [16].

Third, the two models differ in their predictions on the influence of a magnetic field on the detection efficiency. In the diffusion-based model this dependence is strong, since vortices enter from the sides of the wire, where the current is most affected by the applied field. In the normal-state vortex model, in contrast, this dependence is weak, especially at high detection probabilities, since for most detection events the vortices nucleate near the center of the wire, where the current density is not affected by the applied field.

However, since both models contain essentially similar physics, approached in two different theoretical frameworks, it is conceivable that the two models will eventually both be refined to the point where they produce the same results.

1.2.6 Other Features of the Detection Process

In the meantime, other aspects of the detection mechanism were elucidated. The electro-thermal mechanism by which the detector resets after a detection event was investigated by Kerman *et al.* [9], who pointed out the role of kinetic inductance in the modelling of the electrical properties of this system. In a seminal work by Clem and Berggren [29], current crowding in the bends of the meander was identified as the major limitation on the critical current [31] in meander-type detectors. The photo-absorption into the wire was also investigated. It was demonstrated that the detector is polarization-sensitive: the electric field parallel to the wires is absorbed preferentially compared to field perpendicular to the wires [10, 11, 12, 13].

1.3 Experimental Techniques

In this section, I will introduce the three main features of our experiment: quantum detector tomography, multiphoton detection and the nanodetector.

1.3.1 Quantum Detector Tomography

Quantum detector tomography is an experimental procedure to measure the detection statistics of a photodetector whose response is unknown². The goal is to find the response of the detector in the number state (Fock) basis, i.e. to find out what would happen if the detector were to receive exactly n photons as an input. This experiment was first demonstrated by Lundeen *et al.* [36, 37], who performed detector tomography on an avalanche photodiode.

It would be most straightforward to probe the detection statistics directly in the Fock basis, but these states are not easily experimentally available. Therefore, it is much easier to use states which are some superposition in the number state basis, which are produced by conventional light sources. Since the detector is not sensitive to the phase of the incoming photon, we may adopt a classical picture in which we consider only the photon number probability distribution, i.e. we restrict ourselves to the diagonal elements of the density matrix. The strategy is then to measure the detection probability for many different photon number probability distributions, and apply a transformation to convert these results into the response in the number state basis.

The most convenient set of states to use for quantum detector tomography is the set of coherent states. These states, which are produced by a laser, have the convenient property that an attenuated coherent state still remains coherent. This means that it is possible to create the desired set of photon number probability distributions simply by attenuation.

²The quantum detector tomography code used throughout this thesis is available on request from the author.

The experiment is then to take a pulsed laser with a well-defined pulse energy and apply fixed attenuation and measure the detection probability. If we have sufficient statistics for this attenuation, we go to the next attenuation, and so on. By repeating this process for sufficiently many attenuations it becomes possible to find the response of the detector in the Fock basis.

It should be noted that the transformation that converts the experimental results into a description in the number state basis is not necessarily simple. The transformation can strongly amplify measurement noise, or even produce nonphysical results. In fact, a branch of mathematics is dedicated precisely to finding convenient transformations for various types of problems of this nature [38]. The usual strategy is to restrict the transformation on the basis of some additional information which was not previously considered. In the case of quantum detector tomography, this is usually done by assuming that the response to different numbers of photons doesn't change strongly for adjacent photon numbers, i.e. if we know the detection probability of n photons p_n , then our zeroth-order guess for $p_{n+1} \approx p_n$. This restriction can be applied in various mathematical guises, and turns out to be sufficient to 'tame' the transformation.

1.3.2 Multiphoton Detection

Multiphoton detection refers to the phenomenon that two photons absorbed simultaneously in the detector can lead to a detection event. These detection events occur at lower currents than single-photon detection events, even when a single photon does not. This effect was noticed early on in the development of SSPDs [1] (see Figure 1.5), but didn't find any applications until Bitauld *et al.* [39] showed multiphoton nanoscale imaging and Zhou *et al.* [40] showed that this effect could be used to build an ultrasensitive higher-order autocorrelator.

We use multiphoton detection as a tool for probing the detection mechanism. Multiphoton detection has two strong advantages compared to single-photon detection when it comes to experiments into the physics of the detection mechanism.

The first advantage is that it enables the experimenter to excite the detector with a range of energies in a single experiment, at a single wavelength. This means that the relation between bias current and photon energy can be measured in a single experimental configuration, without changing the wavelength of the incident light. Changing the wavelength of the incident light usually means changing the intensity, and the size of the illumination spot, leading to different illumination conditions [16]. Using multiphoton excitation sidesteps this problem.

The second advantage is that multiphoton excitation allows for a much larger range of photon energies to be used than in single-photon excitation. Typically, a source is only tunable in a particular wavelength range, and this dynamic range can be hugely extended by using multiphoton excitations.

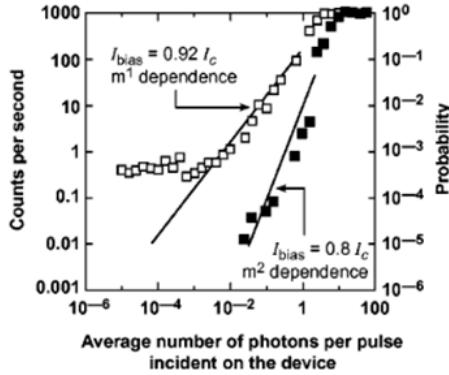


Figure 1.5: The earliest measurement on two-photon processes in SSPDs. The solid black squares represent the detector operating in a two-photon mode, which occurs at lower bias current. The quadratic dependence of the count rate on the input photon number is a signature of a two-photon process. From [1].

Also, the sample substrate, the windows of the cryostat, or even the air of the laboratory may all be absorbing at particular energies of interest. Using multiphoton excitations solves this issue.

1.3.3 Nanodetector

The nanodetector is a particular geometry for SSPDs (see Figure 1.6), first developed by Bitault *et al.* [39], which is convenient for experiments on SSPD physics. In this geometry, the usual meander is reduced to a single line contact between two tapered banks. In a variant of this design, there is a short (a few hundred nm) bridge between the two banks. Only the central part of this device (the line contact or the bridge) is photodetecting, the banks merely serve as contact points for the bias current. An inductor which serves to balance the reset time of the detector with its cooling time is connected in series to the detector, to prevent latching [9].

For fundamental studies, this geometry has three main advantages: robustness, simplicity and enhanced multiphoton response. First, this geometry is less sensitive to fabrication errors. It is difficult to make a long wire with uniform edges. Any notch, bulge or other imperfection in the wire (the phenomenological term for such imperfections is *constrictions* [41]) will be more strongly photodetecting than the rest of the wire, leading to experimental results which are difficult to interpret.

Secondly, the nanodetector doesn't contain any bends. In previous experiments, indications were found that bends behave differently than straight sections of wire [26, 42]. Normally, samples are considered which contain

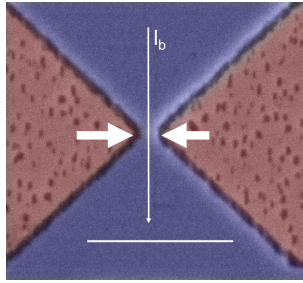


Figure 1.6: False-colour SEM image of our detector. The blue area indicates the NbN layer, the red areas indicate places where the layer has been etched away. The two thick arrows indicate the active part of the detector. The vertical arrow indicates the direction of the current flow. The horizontal white line is a $1 \mu\text{m}$ scale bar. Image courtesy of Döndü Sahin.

both bends and straight sections. It can be unclear whether photodetection results from the bends or not. Moreover, for phenomena such as the critical current of an SSPD, the bends are the dominant feature [31], obscuring the intrinsic response of the wire.

A third advantage of a nanodetector is that it has a relatively enhanced multiphoton response. In a meander geometry, it is necessary for two photons to be absorbed within some distance from each other in order to trigger a two-photon detection event [43, 44]. However, each photon individually will also have a finite, but strongly reduced possibility of triggering the detector. For a sufficiently long wire, however, this effect will dominate over the two-photon effect. In a more compact geometry, all absorbed photons contribute to photodetection. This is therefore a suitable geometry in which to study multiphoton detection events.

Chapter 2

Modified Detector Tomography Technique Applied to a Superconducting Multiphoton Nanodetector

We present a complete method to characterize multiphoton detectors with a small overall detection efficiency. We do this by separating the nonlinear action of the multiphoton detection event from linear losses in the detector. Such a characterization is a necessary step for quantum information protocols with single and multiphoton detectors and can provide quantitative information to understand the underlying physics of a given detector. This characterization is applied to a superconducting multiphoton nanodetector, consisting of an NbN nanowire with a bow-tie shaped subwavelength constriction. Depending on the bias current, this detector has regimes with single and multiphoton sensitivity. We present the first full experimental characterization of such a detector¹.

2.1 Introduction

Multiphoton detection is a vital tool for optical quantum computing [45]. Such multiphoton detection can take many forms, two important examples

¹This chapter is based on J.J. Renema *et al.*, Opt. Exp. **20** (3), 2806-2813 (2012).

of which are *photon-number resolved detection*, where the detector is able to distinguish precisely the number of photons, and *threshold detection*, where the detector is merely able to distinguish between the cases 'N photons or more' and 'fewer than N photons' [37].

The common factor in all multiphoton detectors is that they are based on a nonlinear mechanism such that the response of the detector depends in some nontrivial way on the number of photons impinging on the detector. There is typically also a finite probability that a photon impinging on the detector does not participate in the detection process at all. Such losses can be modeled as attenuation of the input state impinging on an ideal (i.e. 100% efficient) detector [37].

A well-established tool to characterize any quantum detector is detector tomography, for which the mathematical framework is that of Positive Operator Valued Measures (POVM) [36, 37, 43]. In this characterization technique, the goal is to find the probability that the detector clicks, given that N photons are incident on the detector. These probabilities can be determined by illuminating the detector with a set of coherent states, and measuring the probability that the detector clicks as function of the input power. The power of detector tomography is that it allows us to characterize the detector using only coherent states as a probe. To do this, it takes into account the distribution of photon numbers in a coherent state and gives the probability of the detector responding to N photons.

Without introducing further assumptions, detector tomography is not immediately applicable in the situation where there is a large and unknown loss component in the detector. In this regime, the outcome would be heavily influenced by the probabilities dictated by the linear losses. To characterize the multiphoton behaviour of the nonlinear detection mechanism, the range of test states would have to be large (of the order η_{sde}^{-1} , where η_{sde} is the system detection efficiency), which would result in an overwhelming number of free parameters leading to a strongly overdetermined system.

In this work, we present a method to separate the nonlinear detection mechanism from the linear loss. We apply this method to the case of an NbN nanodetector, where we obtain the first full experimental characterization of such a detector.

This characterization has two applications. First of all, it gives the complete statistics of the response of the detector to any incoming state, which is of interest when a detector is used in a quantum communication or quantum information experiment. Secondly, since this characterization is model-independent, it can be used to investigate the physics of the detection mechanism. This latter application is especially important in detectors where the detection mechanism is not fully understood, as is the case for an NbN nanodetector [8].

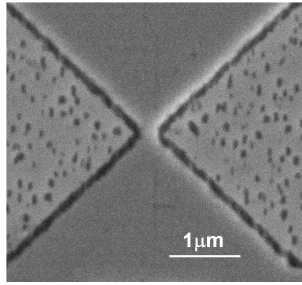


Figure 2.1: SEM image of the NbN nanodetector. The smooth gray area is the NbN, with the constriction in the middle. From this image, the width of the constriction was estimated to be 150 nm.

2.2 NbN Nanodetectors

NbN nanodetectors consist of a bow-tie shaped constriction in an NbN nanowire [39]. The width of this constriction can be as small as 50 nm. This detector functions on the same detection principle as the well-known NbN meanders [1]. A detection event happens when one or more photons induce a break in the superconductivity and cause the formation of a resistive bridge across the detector [8], causing a voltage pulse which is detected by the readout electronics. In the nanodetector, since the bias current density is only high around the constriction, this detector has subwavelength resolution [39]. Furthermore, it is possible to lower the bias current to such a value that multiple photons are required to provide a perturbation that is strong enough to break the superconductivity. Operation in this regime results in a subwavelength multiphoton detector. Such a detector may allow for subwavelength mapping of optical fields and high-resolution near-field multiphoton microscopy.

The operation of the NbN nanodetector differs from that of an ideal N -photon threshold detector, as was already observed in the first paper announcing the construction of such a device [39]. In order for these detectors to be used in e.g. subwavelength mapping of N -photon optical fields, it is vital that their response to different photon numbers is well understood [46].

A complete characterization of the detector may also be of fundamental interest for the study of the more well-known NbN nanowire meander detectors [1]. Due to the well-localized sensitive area of the detector, the multiphoton regime is more apparent and more easily understood in a nanodetector as compared to an NbN meander, where two impinging photons are most likely absorbed in different areas of the detector. Furthermore, it has been suggested that unintended constrictions form an important limitation on the performance of an NbN meander [41]. In these respects, NbN nanodetectors may serve as models for the response of NbN meanders.

2.3 Experimental Setup

The NbN nanodetector used in this experiment was manufactured on an NbN film deposited by DC magnetron sputtering on a GaAs substrate [47]. A nanodetector was patterned out of the NbN film by means of electron beam lithography (EBL) and reactive ion etching (RIE). The width of the constriction was estimated to be 150 nm (see Figure 2.1). The detector was cooled in a VeriCold cryocooler with a final Joule-Thompson stage to 1.17 K. The detector critical current was measured to be $29 \mu\text{A}$.

We illuminate the sample with a Fianium supercontinuum laser with a repetition rate of 20 MHz and a pulse width of 6 ps, which was filtered to have a center wavelength of 1500 nm, with a spectral width of 10 nm. The detector was illuminated through a single-mode lensed fiber producing a nominal spot size of $3 \mu\text{m}$ at 1500 nm. The readout electronics consist of a bias-tee (Minicircuits ZNBT-60-1W+), an amplifier chain and a pulse counter.

Each experiment consists of a large series (>20) of experimental runs, each at constant light power, where the current through the detector is swept by means of voltage biasing, resulting in steps of $0.2 \mu\text{A}$, up to the critical current. Power stability during each run was monitored by a power meter which receives a pick-off beam from a beam splitter in the fiber leading to the experiment. Finally, the 2-dimensional set of count rates $C(I_b, N)$ is rearranged and normalized by the repetition rate of the laser to yield the detection probability per pulse $R(N)$ at fixed bias current I_b .

For each experiment, the power was varied so as to obtain the complete detector response curve from detection probability $R = 10^{-6}$ to $R = 1$. This required varying the input power over 5 orders of magnitude, typically from 20 pW to $5 \mu\text{W}$ input power into the cryostat. At a repetition rate of 20 MHz the largest input power corresponds to $N = 2 * 10^6$ incident photons per pulse. Since the detection efficiency of our detector is low (order 10^{-4}), it was not necessary to introduce further attenuation, as is usually done in detector tomography experiments [37].

2.4 Effective Photon Detector Characterization

To understand the optical response of the NbN nanodetector, our starting point is detector tomography, which has been developed in [36, 37, 48] in the framework of the POVM formalism. This technique provides an assumption-free method to characterize the response of an unknown detector system using a set of coherent states as inputs. We limit ourselves to the case where there are only two possible responses: click or no click. The idea is to translate the response of the detector from the basis in which it can be measured (the coherent state basis) into the basis in which we want to know it, which is the Fock (number) state basis [36]. For an input state described

by a density matrix ρ , the probability R to observe a detection event is:

$$R_{click} = \text{Tr}(\Pi_{click}\rho) \quad (2.1)$$

$$\Pi_{click} = \sum_{i=0} p_i |i\rangle\langle i|, \quad (2.2)$$

where Π_{click} is the POVM of having a detection event, and p_i is the probability of a detection event occurring given a Fock state with i photons as input.

Keeping in mind that for coherent states, the probability distribution of photon numbers is completely determined by the mean photon number of the state, we can write:

$$R_{click}(N) = \sum_{i=0} p_i c_i(N), \quad (2.3)$$

where $c_i = e^{-N} \frac{N^i}{i!}$ is the weight of the i -th basis state in the probe coherent state and N is the mean photon number. By measuring the detection probability R as a function of the input mean photon number N of the coherent state, we can use $c_i(N)$ to reconstruct the set of probabilities p_i , either by a maximum likelihood algorithm [37] or a simple curve fit [49]. Since we are dealing with a detector that saturates, i.e. that always has a detection event at high input power, the problem is simplified by reasoning from the case that the detector doesn't have a detection event [50]. Since there are only two possible outcomes, this gives:

$$R_{click}(N) = 1 - R_{no\ click}(N) \quad (2.4)$$

$$= 1 - e^{-N} \sum_{i=0} (1 - p_i) \frac{N^i}{i!}, \quad (2.5)$$

where N is the mean photon number. The case $p_0 = 0, p_{i>0} = 1$ is applicable to any one-photon threshold detector, such as an APD with unity detection efficiency [37].

In this chapter, we introduce an extension of detector tomography designed for use in situations where there is a large linear loss, as is the case with NbN nanodetectors. The goal of this model, which we call Effective Photon Detector Characterization (EPDC), is to separate linear losses from the nonlinear action of the detector, which is of physical interest. To account for this loss, we introduce a *linear loss parameter* η that describes the probability of for each photon to participate in the nonlinear process. Since coherent states remain coherent under attenuation, the EPDC function then becomes:

$$R_{click,EPDC}(N) = 1 - e^{-\eta N} \sum_{i=0} (1 - p_i) \frac{(\eta N)^i}{i!}, \quad (2.6)$$

where $\{p_i\}$ and η are the free parameters². Since the POVM description is complete [36, 50] and we have added a parameter, we have now created a function that is overdetermined by one parameter. However, we can choose a solution based on physical grounds. Since we know our detector has threshold-like behaviour, it is reasonable to assume that for some large number of photons i_{max} the probability $p_{i_{max}}$ with which the detector will have a detection event is arbitrarily close to 1. Furthermore, once we have found such an i_{max} , we can assume that $p_{j>i_{max}} = 1$ for all $j > i_{max}$, since otherwise we would have the unphysical case that adding photons makes it less likely that a detection event occurs. We can then create a series of candidate solutions by fitting equation 2.6 to our measured count rates as a function of input photon number, truncating the sum at various values i_{max} . This gives a series of candidate solutions parameterized by $\{\eta, p_0 \dots p_{i_{max}}\}$. The solution we pick is the one that fits our data and has the minimum i_{max} , since this is the one that requires the fewest parameters to explain our data³.

The big advantage of this approach is that we describe the entire linear loss with a single parameter, thereby separating the linear losses from the nonlinear action of the detector, and drastically reducing the number of fit parameters. Typically, the nonlinear action of the detector, quantified by the p_i , is the quantity of interest for multiphoton detection. This approach is particularly relevant for detectors with a large linear loss component, since if this loss is not taken into account separately it would dominate the characterization of the detector.

2.5 Result

The points in Figure 2.2 show the measured count rate points as a function of input power from our NbN nanodetector at three different bias currents. The lines represent the fits, with the colour indicating the value of i_{max} (see legend). For each fit the reduced χ^2 are shown in the bar diagrams in the insets of the figure. We take the fit that explains the data with the smallest number of parameters as the most physically realistic solution. This choice is indicated by the arrows in the bar diagrams. By repeating this algorithm over a range of bias currents, we can completely characterize how the response of the detector to a given number of photons varies with the bias current.

In Figure 2.3, the results from the Effective Photon Detector Characterisation are shown as a function of bias current. At each bias current, the obtained p_i and η describe the operation of the detector, independent of

²We note that we have made the implicit assumption that $R_{N \rightarrow \infty} = 1$. This is not always the case, but equation 2.6 can be rewritten to accommodate this.

³We will see in Chapter 4, Appendix I that the notion of 'fits the data with minimal parameters' can be formalized by means of the Akaike Information Criterion.

power. We therefore conclude that we have obtained a complete description of the detector behaviour.

2.6 Discussion

The p_i obtained from the fit represent the nonlinear action of our detection system, which is the physical property of interest. Since there are no other nonlinear elements in the detection system, we can unambiguously attribute the behaviour of the p_i to the NbN nanodetector. It should be noted that the result presented here is consistent with earlier results on these detectors [39], e.g. we reproduce the finding that the transitions between the various detection regimes (where the detector behaves approximately as an N-photon detector) are equally spaced in the current domain.

From equation 2.3, we can see that the response of the detector is given by terms of the form $p_i c_i(N)$, where $c_i(N)$ is the probability of having N photons. From this we can see that each p_i will be most dominant in the range of powers where the probability of having the corresponding number of photons is highest. For example, at $17 \mu\text{A}$ the detector has $p_1 = 0.06$ and $p_2 = 0.37$, meaning that at low powers ($\eta N < 0.16$), where the one-photon contribution from the state is dominant, the detector will respond mostly to single photons, but at higher powers ($\eta N > 0.16$) the response will be dominated by the two-photon events. This quantifies the change of detection regimes reported in measurements of count rate as a function of power [39].

The fitted linear detection efficiency η fluctuates between $(9.6 \pm 0.2) * 10^{-5}$ and $(14.7 \pm 0.6) * 10^{-5}$. Normalizing to the estimated effective area of the detector of 100 nm by 150 nm and the beam size, we obtain an intrinsic detection efficiency of 8%. While it should be noted that this is only a rough estimate, it is higher than the value of 1% reported in [39]. We attribute this to the lower temperature of the experiment, at which NbN detectors are known to be more efficient [8].

It should be noted that since we combine all linear losses into a single parameter, we are unable to distinguish losses after the absorption event from those before the absorption event, provided they are linear. It is known for NbN meanders that not every absorbed photon causes a detection event [41]. However, since our measured linear loss does not depend on the bias current, it is reasonable to attribute it to optical loss and not to losses inside the detector. With the caveat that there may be a constant linear loss inside the detector, we can therefore conclude that the set of p_i completely describes the behaviour of the detector.

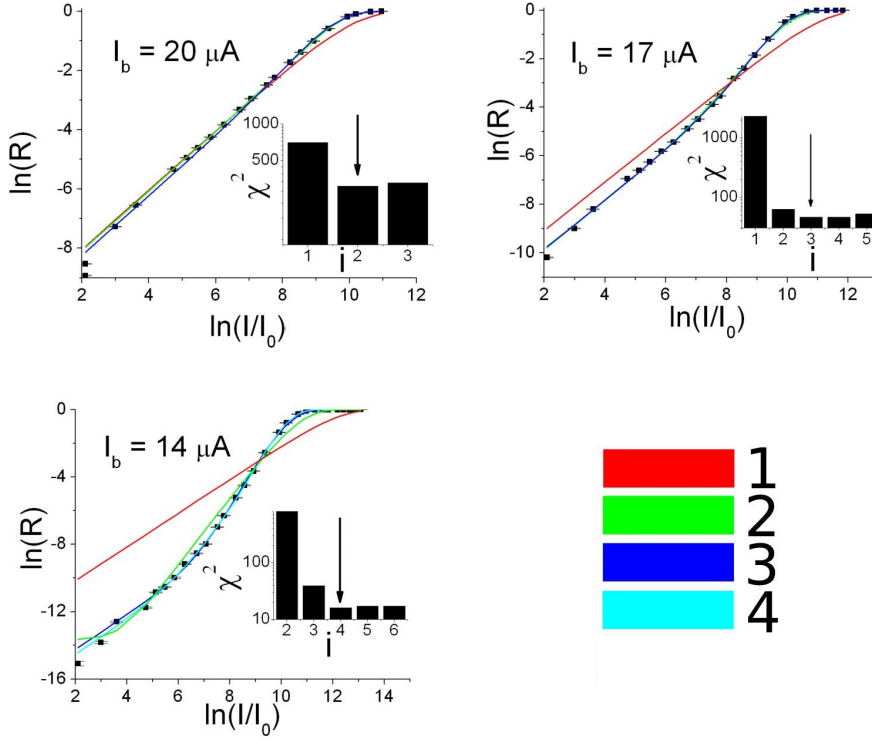


Figure 2.2: Measurement of the NbN nanodetector count rate as function of input power at $I_b = 20 \mu\text{A}$, $I_b = 17 \mu\text{A}$ and $I_b = 14 \mu\text{A}$, fitted with the EPDC model (equation 2.6). The black squares represents the data points with error bars, the other lines represent fits, with the number of free parameters represented by the color of the line (see legend). Note that many of these lines overlap with each other and with the data. Insert: reduced χ^2 of the fits as a function of number of parameters. For $I_b = 14 \mu\text{A}$ we have omitted the case $i = 1$, where $\chi_{reduced}^2 > 10^4$. The arrows indicate the best fit. Note that in all three cases there are multiple fits which have similar reduced χ^2 , we reject the ones with superfluous free parameters for physical reasons.

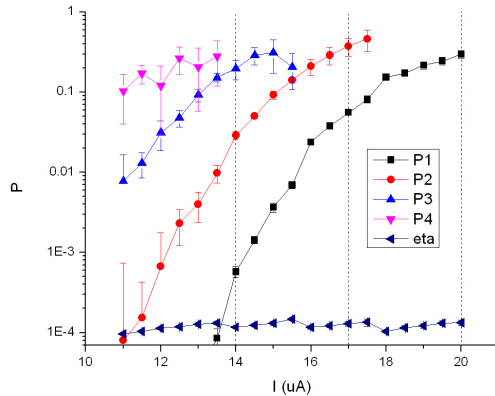


Figure 2.3: Nonlinear parameters and linear detection efficiency as function of bias current. This figure was obtained by repeatedly applying the method outlined in Section 2.4 at various bias currents. The three dashed lines indicate the bias currents from Figure 2.2.

2.7 Conclusion

We have introduced an extension of detector tomography which is applicable in the presence of a large linear loss. This detector characterization is of interest when using a quantum detector in a quantum optics or quantum communication experiment, since it gives a full prediction of the response of the detector to any incoming state. Furthermore, we have completely characterized the response of a superconducting nanodetector, over several operating regimes of the detector. This represents the first complete characterization of this type of detector, which is necessary for the use of this detector in the context of multiphoton subwavelength detection.

A second application of this characterization method is that it provides quantitative information about the response of the detector. Such a quantitative characterization can also be used to test theoretical predictions of the response of the detector as a function of bias current [18], enabling further insight into the physics of the detection event in NbN photodetectors.

The idea of our formalism is to separate this linear loss from the nonlinear action of the detector. For the detector under study in this chapter, this formalism completely describes the response of the detector. In contrast to earlier methods [44, 51] that assume a priori knowledge of the underlying detector physics, detector characterization based on the POVM formalism can be applied to any detector system without making assumptions about the operating principle of the detector [36, 43]. Therefore, the strength of the characterization applied here is that we can extract model-independent

parameters that can be used to gain insight in the physics of photon detection with NbN detectors.

Finally, we comment on the applicability of our algorithm to other detectors: Effective Photon Detector Characterization shares the feature with detector tomography that it is as assumption-free as possible; making it possible to characterize a detector without any prior knowledge or model of the operational mechanism of the detector. The EPDC method has the added requirement that the detector saturates (i.e. always produces the same outcome) at some high input photon number. To our knowledge, this behaviour is generic to all quantum detectors constructed to date [2, 51, 52, 53, 54]. It therefore does not represent an practical limitation.

Chapter 3

Universal Response Curve for Nanowire Superconducting Single-Photon Detectors

Using detector tomography, we investigate the detection mechanism in NbN-based superconducting single-photon detectors (SSPDs). We demonstrate that the detection probability uniquely depends on a particular linear combination of bias current and energy, for a large variation of bias currents, input energies and detection probabilities, producing a universal detection curve. We obtain this result by studying multiphoton excitations in a nanodetector with a sparsity-based tomographic method that allows factoring out of the optical absorption. We discuss the implication of our model system for the understanding of meander-type SSPDs¹.

3.1 Introduction

Nanowire Superconducting Single-Photon Detectors (SSPDs) [1] have high detection efficiency [55], low dark counts, low jitter and a broadband absorption spectrum [56]. This makes them suitable for many applications including quantum optics [57, 58, 59, 60], quantum key distribution [5, 61], optical coherence domain reflectometry [62] and interplanetary communication [6]. These detectors typically consist of a thin nanowire (~ 4 nm x 100 nm) of superconducting material, such as NbN [1], TaN [20], NbTiN [63], Nb

¹This chapter is based on J.J. Renema *et al.*, Phys. Rev. B **87** (17), 174526 (2013).

[64], or WSi [55], which is typically fabricated in a meander shape to cover an active area of $25\text{-}1600\ \mu\text{m}^2$ [65]. The absorption of a single photon in the nanowire results in the creation of a region with a non-equilibrium concentration of quasiparticles. When the nanowire is biased close to the critical current, this perturbation causes a transition from the superconducting to the resistive state, producing a voltage pulse in the external circuit.

While progress has been made in understanding the detection process, many crucial features of the process are still unknown. In this chapter, we investigate the detection process by means of a model system: an NbN nanodetector [39] (see Figure 3.1). This detector has a single cross section of wire as its active element, defined by a bow-tie shaped constriction. We investigate this system with sparsity-based detector tomography. The tomographic method does not require a model of the device, which makes it ideally suited as a tool for investigating the working principle of a detector of which the working mechanism is not fully understood yet.

It has long been known that at lower bias current, the detector operates in a regime where multiple photons are necessary to break the superconductivity [1, 66]. In a nanodetector, the geometry is such that many multiphoton processes play a strong role [39, 67]. This enables us to probe the response of the device to excitations at different energies simultaneously. The role of detector tomography is to extract the effects of the various multiphoton excitations.

In this chapter, we investigate the detection process by combining tomography and a nanodetector. With this combination, we can probe the system in a way that is independent of the incoupling efficiency of light into the detector. Moreover, because we tune the energy of the excitation via the number of photons at the same wavelength, we are insensitive to wavelength-dependent effects in the setup. This combination allows us to focus on the fundamentals of the detection process. We demonstrate that for intrinsic detection probabilities ranging from 0.3 to 10^{-4} , the detection probability depends only on a specific linear combination of bias current and excitation energy. Thus, we obtain a universal detection curve for our model system of an SSPD: for each bias current and excitation (photon) energy, the detection probability is given by a point on this single curve. This universal curve stretches from the regime where photodetection is almost deterministic (given that the photon is absorbed into the active area) to the regime where fluctuations in the wire are thought to play a role in assisting the detection process.

3.2 Experiment

All experiments in this work were performed on a nanodetector (see Figure 3.1). The nanodetector consists of 4 nm thin NbN wire on a GaAs substrate, shaped into a 150 nm wide bow-tie geometry. The device was fabricated via

a combination of DC magnetron sputtering [47], electron-beam lithography, reactive ion etching and evaporation of the metal contacts [39]. In Chapter 2 and ref. [39] it was shown that such a detector has multiphoton regimes based on the bias current. The physical mechanism behind these multiphoton regimes is that at relatively low bias currents, multiple photons are required to supply a sufficient perturbation for the superconductivity to be broken.

The device was cooled in a two-stage pulse-tube / Joule-Thompson cryocooler to a temperature of approximately 1.2K. The nanodetector was illuminated using a lensed fiber mounted on cryogenic nanomanipulators. At this temperature, the overall system detection efficiency for single photons was 1.5×10^{-4} around our working point at $I_b = 20 \mu\text{A}$ ($I_c = 29 \mu\text{A}$). This low efficiency is attributable to the mismatch between the device active area and the size of the illumination spot. The device was operated in a voltage bias regime, using a low-noise voltage source (Yokogawa GS200) in series with a 10Ω resistor. The detector was biased through the DC port of a bias tee, and the RF signal was amplified in a 45 dB amplifier chain.

The device was illuminated with a Fianium Supercontinuum laser, whose pulse duration was specified to be 7 ps. It is crucial for this experiment that the pulse duration is shorter than the lifetime of an excitation, which was measured to be several tens of picoseconds [40, 68, 69]. If the pulse duration is longer than that, it is possible to have a pulse which produces two excitations which are far enough apart in time that one has died out before the second is created; this will therefore not result in a multiphoton excitation.

We confirmed that our laser produces coherent states, measuring $g^{(2)}(\tau = 0) = 0.98 \pm 0.01$ in a separate experiment. Furthermore, we measured that the intensity fluctuations in the laser are below 2%. Hence, the laser is suitable for tomography [37]. The detector was illuminated with narrowband light at wavelengths of 1000 nm, 1300 nm and 1500 nm ($\Delta\lambda = 10$ nm). In our experiment, we vary the intensity and wavelength of the input light, at various bias currents. At each of these settings, we record the count rates in a 0.1 s time window and repeat the experiment 10 times per measurement setting. In the current regime investigated in the present experiment, the detector has negligible dark counts ($< 1 / \text{s}$).

3.3 Tomography of Multiphoton Excitations

In order to distinguish the effects of the various photon numbers in the laser pulses, we make use of a sparsity-based tomographic protocol. We give here a brief summary of this protocol (for a full description, see Chapter 2, where we introduced this technique). We illuminate the detector with a range of coherent states, and record the detection probability R_{click} . We make use of two properties of coherent states: first, that a coherent state under attenuation remains coherent, second that the decomposition of the coherent

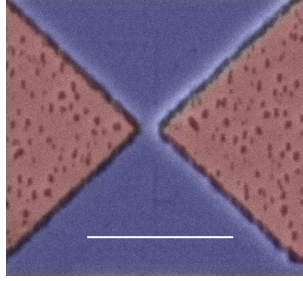


Figure 3.1: False-color SEM image of the detector. The active part of the detector is the narrow bridge in the centre of the image. The blue parts represent the thin layer of NbN, the red parts are the GaAs substrate. The scale bar has a length of $1 \mu\text{m}$.

state in the Fock basis is completely determined by the mean photon number, which can be determined by measuring the intensity².

Each illumination intensity probes the detector with a different linear combination of photon number states, introducing different combinations of multiphoton excitations. In particular, we model the detection probability R_{click} by:

$$R_{click} = 1 - e^{-\eta N} \sum_{n=0}^{\infty} (1 - p_n) \frac{(\eta N)^n}{n!}, \quad (3.1)$$

where η is the incoupling efficiency (linear loss) and N is the mean photon number of the incident coherent state. The linear efficiency appears separately, since our protocol enables us to distinguish linear processes - such as incoupling to the NbN film - from nonlinear processes [67]. The p_n are the quantities of interest in further analysis: they describe the probability of a detection event, given the absorption of n photons in the active area of the detector.

Figure 3.2 illustrates this protocol as applied to a single experimental run for a given bias current. We vary the incident power, observe the detection probability, and apply the tomographic protocol to find the contributions from the various multiphoton excitations. The black squares indicate the measured count probability, approaching 1 as the detector saturates. The red, green and blue lines indicate the contribution from one photon, two photons and higher photon numbers, respectively. Only a limited number of multiphoton excitations are resolvable, and this number depends on bias current. The rest is lumped into a remainder term containing the limit of high photon numbers and is not used in further analysis. The fact that at various powers different multiphoton processes are dominant enables us to recover them all from a single experiment. Furthermore, since the linear

²Since we have a phase-insensitive detector, the phase of the coherent state amplitude is irrelevant, and we set it to zero throughout this chapter for simplicity.

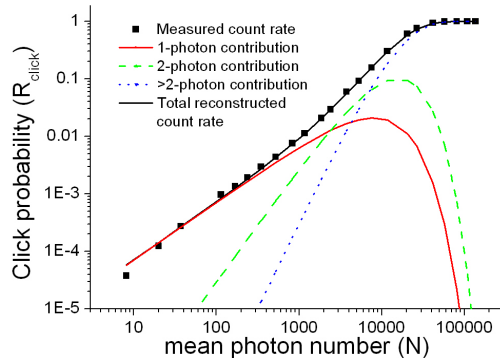


Figure 3.2: Illustration of the tomographic protocol. The black squares indicate the measured count rate as a function of input power, at $\lambda = 1500$ nm and $I_b = 17 \mu\text{A}$. The red (solid) and green (dashed) lines show the contribution to the count rate of single photons and photon pairs, respectively. The blue (dotted) line shows the contribution of higher numbers of photons. The black line shows the sum of all the photon contributions, indicating that our tomographic reconstruction successfully reproduces the observed count rates. From this fit, we reconstruct the set of detection probabilities p_n and the linear efficiency η , which together fully describe the behaviour of the detector.

efficiency η only rescales the effective incident photon number, but does not alter its shape (corresponding to a simple shift in Figure 3.2), we are also able to distinguish finite incoupling effects from effects due to multiphoton excitations.

3.4 Results

Figure 3.3 shows the reconstructed detection probabilities p_n , as a function of bias current and three different wavelengths. For each wavelength and current, we independently perform the tomographic procedure outlined in Section 3.3 and obtain a full set of parameters p_n . We observe that as the current is lowered, the detector makes a transition from being a one-photon threshold detector to a two-photon threshold detector, and so on. Furthermore, we observe that the response curves at different photon numbers and wavelengths have the same shape. We note that as the excitation energy becomes higher and the photon number larger, the points on our curves become more scattered, indicating that the tomography procedure becomes less accurate.

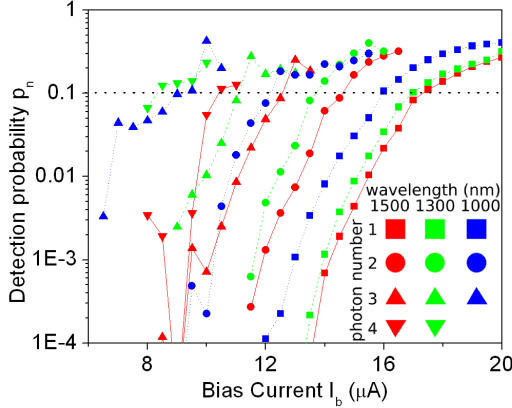


Figure 3.3: Current dependence of the nonlinear parameters p_n , as a function of wavelength and photon number. The probability p_n of a detection event at a given wavelength and photon number is plotted as a function of the current. The plots are color-coded by wavelength. The shape of the symbols indicates the photon number (see legend). The connecting lines are a guide to the eye. The dotted line indicates the threshold level ($p = 0.1$) used to obtain Figure 3.4.

Figure 3.4 shows the bias current required to reach a detection probability of 10%, as a function of total excitation energy. In order to obtain this figure, we took a surface of constant $p_n(E, I_b) = 0.1$ in Figure 3.3 (indicated by a dotted line), and plotted the bias current at which the detector has 10% probability of responding to an energy E , where $E = nh\nu$ is the total energy of the n photons absorbed by the detector. This figure demonstrates that there is a scaling law between bias current and overall excitation energy. We determine the scaling constant γ to be $\gamma = -2.9 \pm 0.1 \mu\text{A}/\text{eV}$ ($= -1.8 \times 10^{13} \text{ Wb}^{-1}$ in SI units) for our detector. Furthermore, this figure shows that the detection probability is independent of the way in which the excitation is composed of different photons: only the overall energy determines the detection probability. We note that we have used only a small fraction of the data present in Figure 3.3 to obtain the data presented in Figure 3.4.

We compare three models from literature to our data. We find that over the range of the experiment, all three models are consistent with our data. The three models are a hotspot-based model, a hotspot-based model in which diffusion plays a large role and a fluctuation-assisted model. These models distinguish themselves not only by different detection mechanisms, but also by different scaling between bias current and energy at constant detection efficiency.

Figure 3.5 presents the main result of this chapter: a universal detection

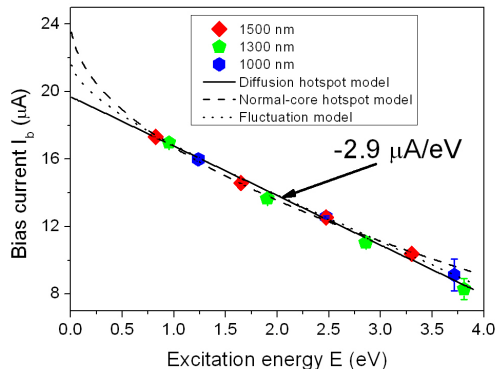


Figure 3.4: Scaling law for the nanodetector. From the data in Figure 3.3, we find all points that have $p_n(E, I_b) = 0.1$ (indicated by the dotted line in that figure), where E is the overall excitation energy. In this graph, we plot the values of I_b and E that satisfy this condition. This graph shows that bias current and overall excitation energy have an approximately linear dependence. The fact that points at various photon numbers all fall on the same line demonstrates that the nanodetector is only sensitive to the overall energy of the excitation. The three lines show the fits of the three microscopic models to the data. Apart from the two rightmost points, the errors on these data points are ~ 100 nA.

curve for a single line-segment of an NbN SSPD. In Figure 3.5, we apply the scaling law, which was derived from the points around $p = 0.1$ to the entire data set. We find that all the curves of detection probability as a function of rescaled bias current superimpose over more than 3 orders of magnitude in the detection probability. This shows that the photoresponse of our detector depends only on this specific combination $I_b + \gamma E$ of bias current and excitation energy. We stress that this universal curve can only be obtained through detector tomography, which allows separation of the effects of multiphoton excitation and finite linear efficiency.

The data presented in Figure 3.5 shows that the scaling behaviour which we obtained at $p_i = 0.1$ in Figure 3.4 is universal for all values of p . Since we have used only the points in Figure 3.3 which lie around to obtain the result in Figure 3.4, we do not a priori expect the curves to superimpose when we apply the scaling law to the entire dataset. In such a procedure, only the points which are used to obtain the scaling factor are guaranteed to superimpose. Since the curve is universal over more than 4 orders of magnitude in the detection probability, we have demonstrated that our results are independent of the arbitrary choice of the 10% criterion. The criterion only matters for the accuracy with which the curves can be superimposed:

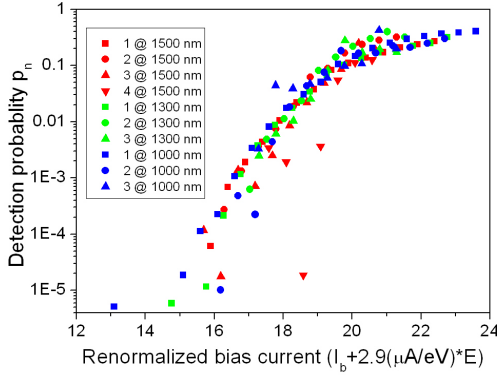


Figure 3.5: Universal response curve for the nanodetector. To obtain these curves, we rescale the curves reported in Figure 3.3 by the scaling law demonstrated in Figure 3.4.

we find from theoretical simulations that the tomographic reconstruction is most accurate between $p_n = 0.1$ and $p_n = 10^{-4}$. This justifies the choice of our criterion.

3.5 Discussion

In this section, we first compare our experimental method with that of previous studies on SSPDs. Then, we discuss our experimental findings on the universal curve, quasiparticle conversion efficiency. Lastly, we discuss the phenomenon of dark counts in our detector.

3.5.1 Comparison with Previous Work

Previous investigations of the SSPDs detection mechanism were of a semiclassical nature, where only the efficiency and dark count rate were measured. By observing the exponent of the power-law dependence of count rate on input power, one can also infer the photon number detection regime semiclassically. However, such a characterization is limited to the observation that the detector is operating in a particular detection regime; a measurement of p_i (i.e. how strongly the detector is in a particular regime) requires detector tomography. Since the width of each multiphoton regime is $\sim 2 \mu A$ for our experiment, the accuracy of the semiclassical method is rather limited. In order to characterize multiphoton processes beyond that resolution, detector tomography is an absolute requirement.

Most previous work focussed on meander detectors, which is the geometry that is normally used in practical applications of SSPDs. In a meander,

two photons that are absorbed in different places along the wire do not constitute a two-photon event, yet they may still produce one-photon events individually. By using a nanodetector, we sidestep any question of how the photons distribute themselves along the length of the wire, which was a major issue in measuring multiphoton effects in meander-type SSPDs [43, 44].

Our present work probes the detection mechanism at various energies simultaneously. We are insensitive to incoupling losses, since they affect the various multiphoton processes equally. Furthermore, since we can perform excitations at different energies with the same wavelength, we are insensitive to any wavelength-dependent effects in the experiment, including wavelength-dependent absorption in the NbN layer.

3.5.2 Universal Curve

The universal curve which we demonstrate in Figure 3.5 is not predicted by any of the current SSPD photodetection models. Typically, such models focus on calculating a single threshold bias current I_{th} , above which the energy of a photon is large enough to deterministically break the superconductivity. Above that current, the efficiency of the detector should be constant. We have shown in the present work that scaling behaviour extends not just to a single threshold current, but to all combinations of currents and excitations in the present experiment. Scaling behaviour applies whether one is in the regime of high efficiency or not. This points to the fact that a single theory should describe detection events in SSPDs, both in the high- and low-efficiency regimes.

3.5.3 Quasiparticle Conversion Efficiency

The fact that only the overall energy of the excitation determines the response of the photodetector can be interpreted in terms of the cascade process that is generated by the initial excitation. This process, which is thought to involve both electrons and phonons in the film, and in which the mutual exchange of energy between the electron and phonon subsystem plays a key role, is still poorly understood. In the present work, we probe this cascade process with different initial excitations, and show that it is only the overall energy which determines the total number of quasiparticles which are produced at the superconducting band-edge. The fact that four excitations of a quarter of the energy produce the same number of quasiparticles as a single excitation with the full energy is evidence that the conversion efficiency by which the energy of the first quasiparticles is distributed over many others is independent of the initial energy.

3.5.4 Dark Counts

We now turn to the phenomenon of dark counts. The most straightforward model is the following: one simply considers a dark count as an excitation with $E = 0$. Extrapolating the linear scaling law from Figure 3.4 to $E = 0$ yields a current of $19 \mu\text{A}$. However, at this current we do not observe a dark count probability of 10% as one would expect from the simple model; we only observe appreciable dark counts around the critical current of $29 \mu\text{A}$. The same discrepancy applies to the other two models. We can therefore say that the picture of a dark count as a zero-energy photodetection event is not supported by our data for any current detection model of SSPDs. The anomalous behaviour of dark counts is a reminder of the danger of assuming a detection model, further demonstrating the relevance of our tomographic method. In particular in this case, the tomographic method gives the first hints of substantial differences in detection mechanism between dark counts and photon counts. We note that the nature of dark counts is still open to debate [24, 70, 71].

3.5.5 Outlook

The present work opens up the possibility of testing the various models of photodetection. This could be done by performing the present experiment in the mid-infrared. For this energy range the predictions of the various models differ significantly (see Figure 3.4). For example, at an excitation wavelength of $5 \mu\text{m}$, corresponding to 0.25 eV , the difference between the predictions of the various models is easily measurable; it is of the order of $1 \mu\text{A}$.

Multiphoton excitation has the practical advantage that the bandwidth of energy excitations which is offered can be extended by a factor equal to the number of photons in the highest excitation (in our case, 4). This has applications in the situation where light of a particular wavelength is difficult to couple onto a cryogenic sample. In particular, the present work opens up the possibility of studying NbN detector behaviour in an energy range that corresponds to the near and medium UV range, using visible and NIR optics.

In a previous publication [40], we have introduced the notion of the non-linear response function (NRF) $\eta(I_b, C)$, which measures the instantaneous detection probability, given that a bias current of I_b is present, and that there are C quasiparticles in the detector. The overall detection probability is then given by $R = \int_t \eta(t) I(t) dt$, where I is the instantaneous intensity. This function can be probed by various means such as a pump-probe experiment. The description in terms of a NRF is well-matched to a tomographic experiment, as both are model-independent descriptions.

The holy grail of tomographic research on SSPDs would be to find the instantaneous detection probability as a function of the number of quasiparticles present at that instant. In the present experiment, we have achieved

a step towards this goal: we have demonstrated the NRF to be of the form $\eta(I_b + \gamma E)$ over the energy range of the experiment, for short-pulse excitations.

3.6 Conclusion

In conclusion, we have studied the physics of photodetection in a superconducting single-photon detector. We have shown that the probability of detection is based on the overall energy of the excitation. Furthermore, we have demonstrated a scaling law between overall excitation energy and bias current. From this, we find a universal response curve that depends only on a given combination of bias current and excitation energy. Thereby, we have shown that the known behaviour of the detector extends into the multiphoton range. These results demonstrate that the tomographic method is a useful tool for investigating the fundamental physics of detection events in NbN SSPDs.

3.i Appendix: Comparison of Experimental Data with Detection Models³

We compare our experimental results to the various detection models of superconducting single-photon detectors. We consider three models: the normal-core model, the diffusion-based model and an early version of a vortex-based model, namely the VAP model of Semenov *et al.*⁴. We parameterize these models as: $E = w^2/C^2(1 - I_b/I_c)^2$ for the normal-core hotspot model, $I = I_0 - \gamma E$ for the diffusion model and $A = (\Delta - \alpha\sqrt{E})(I_0 - \beta I_b)$ [72] for the VAP model, to maintain consistency with the literature.

We apply these three detection models to the results in Figure 3.4, and compare the results with the values from the literature. For the normal-core hotspot model, we find $C = 47 \pm 1 \text{ eV}^{-1/2}/\text{nm}$, which should be compared to the values of $C = 11 - 20 \text{ eV}^{-1/2}/\text{nm}$ found in other experiments [56]. For the diffusion hotspot model, we apply the expression from Ref. [8], to find a theoretical value of $\gamma = -2.5 \mu\text{A}/\text{eV}$ for our sample and $\gamma = -3.5 \mu\text{A}/\text{eV}$ for the samples in that reference, which should be compared with the value of $\gamma = -2.9 \pm 0.1 \mu\text{A}/\text{eV}$ obtained experimentally. For the fluctuation model, we find $\alpha = 2.8 \times 10^{-4} \pm 0.05 \times 10^{-4} \sqrt{\text{eV}}$, which should be compared to a literature value of $\alpha = 6 \times 10^{-4} \sqrt{\text{eV}}$, for the experiment reported in Ref. [23]. We note, however, that comparisons between different detectors are problematic. In particular, the conversion efficiency of the initial excitation to quasiparticles at the gap edge is a free parameter which varies from detector to detector [8].

The error analysis on the quantities given in the previous paragraph was based on the 50 nA accuracy of the current readout of our experiment, combined with error propagation on the interpolation formula used to obtain the intersection with the line $p_i = 0.1$. For low i , the former error dominates. At higher i , we are limited by the quality of our tomographic reconstruction. We calculate $\chi^{(2)}$ per degree of freedom to be 2.2, 2.9, and 2.1 for the normal-core hotspot, diffusion hotspot and VAP models, respectively. These numbers do not enable us to conclusively rule out any of the models.

³This material is based on the appendix to J.J. Renema *et al.*, Phys. Rev. B **87** (17), 174526 (2013).

⁴We retain the comparison with the VAP model for historical consistency with the article on which this chapter is based. Since we will see that this dataset is of insufficient dynamic range to rule out any of the models, comparison with more advanced vortex models will not provide additional information and is postponed to Chapter 4.

Chapter 4

Experimental Test of the Detection Models in Nanowire Superconducting Single-Photon Detectors

We report an experimental test of the photodetection mechanism in a nanowire Superconducting Single-Photon Detector (SSPD). Detector tomography allows us to explore the 0.8-8 eV energy range via multiphoton excitations. High accuracy results enable detailed comparison of the experimental data with theories for the mechanism of photon detection. We show that the temperature dependence of the efficiency of the SSPD is determined not by the critical current but by the current associated with vortex unbinding. We find that both quasiparticle diffusion and vortices play a role in the detection event¹.

4.1 Introduction

Superconducting nanowire single-photon detectors (SSPDs or SNSPDs) [1, 2] are currently the most promising detection systems in the infrared, achieving detection efficiencies of up to 93% at 1550 nm [55]. Despite these technological advances, the fundamentals of the working principle of these detectors are poorly understood and under active investigation, both theoretically [18, 24, 25, 33, 70, 71, 73, 74] and experimentally [8, 16, 15, 23, 56, 75, 76, 77, 78, 79, 80, 81].

¹This chapter is based on J.J. Renema *et al.* Phys. Rev. Lett., **112** (11), 117604 (2014).

A typical SSPD consists of a film of a superconducting material such as NbN or WSi, a few nm thin, nanofabricated into a meandering wire geometry. When biased sufficiently close to the critical current of the superconductor, the energy of one or several photons can be enough to trigger a local transition to the resistive state, resulting in a detection event. The energy of the absorbed photon is distributed through an avalanche-like process, creating a nonequilibrium population of quasiparticles. This quasiparticle population then disrupts the supercurrent flow, resulting eventually in a detection event.

In this chapter, we address the nature of this disruption, which lies at the heart of the photodetection mechanism in SSPDs. At present, there are three important open questions. First: it is unknown whether the detection event occurs when the energy of the incident photon causes a cylindrical volume inside the wire to transition to the normal state (see Figure 4.1a) [1], or whether it is enough for the superconductivity to be weakened but not destroyed by the depletion of Cooper pairs over a more extended region (see Figure 4.1b) [18].

The second open question is whether magnetic vortices play any role in the detection mechanism. There are two varieties of vortex-based models. The first is an extension of the normal-core model, in which a vortex-antivortex pair forms at the point where the photon is absorbed (Figure 4.1c) [33]. In the second, the weakening of superconductivity lowers the energy barrier for either a vortex crossing [24, 82] or a vortex-antivortex pair crossing (Figure 4.1d).

The last open question pertains to the temperature dependence of the photoresponse of SSPDs. Intuitively, one would expect the SSPD to be less efficient at lower temperatures, as the detector works by breaking superconductivity and the energy gap of a superconductor decreases with increasing temperature. However, the opposite effect is consistently observed [8]. Apart from a study of the temperature dependence of the diffusion constant [73], no real headway has been made in this problem.

Our experimental results provide answers to all three questions. In short, we show that both quasiparticle diffusion and vortices play a role in the detection event. We achieve the first result by measuring the functional dependence between the bias current and the photon energy required for a constant detection probability. The observed linear functional dependence is incompatible with the original hotspot model and demonstrates the importance of diffusion. Our evidence for the role of vortices lies in the observation of a reference current which sets the efficiency of the detection mechanism and which is unequal to the critical current and also has a different temperature dependence. At the temperature where the reference current crosses the critical current, the efficiency of the detector degrades. We find that the temperature dependence of the reference current matches that of the current at which vortices can unbind from the sides of the detector.

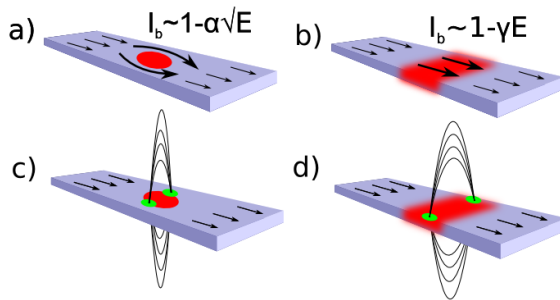


Figure 4.1: Sketches of the four main detection models. *a)* In the normal core-hotspot model, the photon energy creates a normal domain inside the superconductor, which the current has to bypass. *b)* In the diffusion-based hotspot model, the quasiparticles diffuse outward from the point of absorption, creating a band of depleted superconductivity. *c)* In the vortex nucleation model, a vortex-antivortex pair is formed in the hotspot. *d)* In the vortex crossing model, either a vortex or a vortex-antivortex pair (*pictured*) uses an area of weakened superconductivity to cross the wire and annihilate. Picture is not to scale.

4.2 Experiment

We perform the majority of our experiments on a 220 nm wide bow-tie nanodetector [39]. The detector is patterned from a 5 nm thick NbN film deposited on a GaAs substrate. The detector is fabricated by electron beam lithography and reactive ion etching. Photodetection takes place in the narrow ($w_0 = 220$ nm wide) part of the bow tie, where the current density is highest.

Compared to Chapter 3 and previous experiments [8, 16], we significantly extend the energy range over which we probe the detector. The energy range in our experiment runs from 0.75 eV to 8.26 eV, corresponding to $\lambda_{\text{eff}} = 1650$ nm - 130 nm, whereas the energy range in Chapter 3 ran from 1500 nm - 325 nm. We achieve this extension of the energy range by using multiphoton excitations, which are resolved by detector tomography [36, 49, 67, 83]. Detector tomography is a method of quantum detector characterization that relies on illuminating a photon detector with a series of known quantum states and observing the photoresponse. In our case, we use coherent states from a broadband supercontinuum laser, which is spectrally filtered². These states have known photon number distributions which are set by the classical laser intensity, which can be easily varied. From this, we determine the response to each individual number of photons, i.e. the Fock-

²More details may be found in the Appendix to this chapter.

basis response³. The strength of our modified detector tomography is that it allows us to separate the incoupling and absorption efficiency η , i.e. the probability to absorb a photon, from the internal detection probability p_n , i.e. the probability of a detection event given the absorption of n photons. A detailed description of our method can be found in Chapter 2, and in the Appendix to this chapter.

4.3 Results and Discussion

Figure 4.2 shows the measured combinations of bias current I_b and photon energy $E = n(hc/\lambda)$ for which the detection probability equals 1% after absorption of n photons. We achieve this result by performing detector tomography at twelve different wavelengths, and finding the current at which n photons (indicated in the legend) have the required probability to cause a detection event.

To validate our experimental method of using multiphoton excitations to probe the detection mechanism, we measured at wavelengths that are harmonics (e.g. $\lambda = 1500$ nm and $\lambda = 500$ nm). We consistently find that the results of these measurements overlap over the entire measurement range, and have indicated these points with arrows in Figure 4.2. This demonstrates that, irrespective of which detection model is correct, the observed probabilities p_n depend only on bias current and overall excitation energy $E = n(hc/\lambda)$. This is an independent justification of the use of multiphoton excitations to test the detection mechanism.

We can parametrize our complete set of measurements by the expression $I = I_0 - \gamma E$, where I is the observed current required to achieve $p_n = 0.01$, and E is the overall energy of the excitation. The slope γ describes the interchange between bias current and photon energy. By extrapolating to $E = 0$, we find a current I_0 that is unequal to the critical current I_c and which we name the *reference current*, since it functions as the baseline from which the detector response may be determined. At $T = 3.2$ K, we find $I_0/I_c = 0.75$. This experimental result does not change significantly with the choice of threshold criterion. The linear relation persists; a 10% threshold criterion⁴ gives $I_0/I_c = 0.79$.

In the regime $I_0 < I_b < I_c$, all multiphoton detection probabilities p_n of the detector are constant. However, we find that the linear efficiency η increases in this regime. We attribute this to the fact that in our bow-tie structure, a larger area of the detector is above I_0 . It is known that for efficient meander detectors, there is a plateau region where the detector response is constant with current [55]. We note that dark counts occur in

³See Chapter 2 for extensive discussion

⁴With the results presented in Chapter 5, we will be able to investigate in Appendix II of that chapter what the precise consequences are of choosing a threshold criterion $p_n \ll 1$ on the observed energy-current relation.

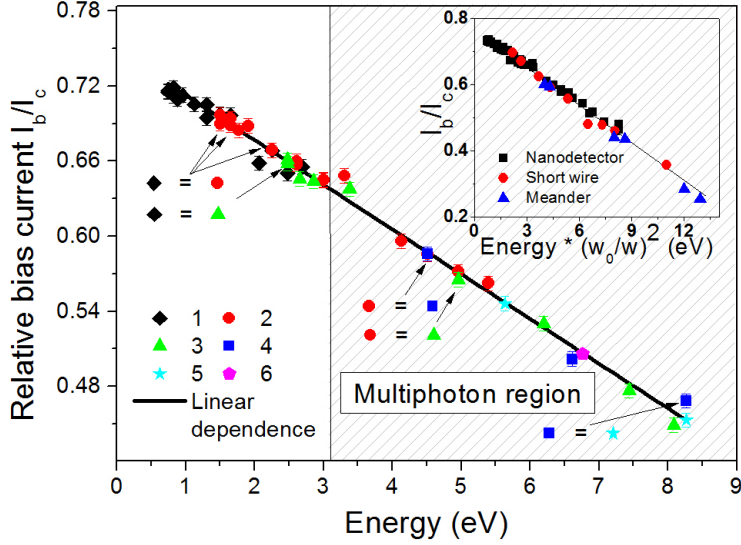


Figure 4.2: Quantum tomography of superconducting single-photon detectors. We plot the bias current required to obtain a 1% probability of a given detection event, as a function of the overall energy of the multiphoton excitation. The points are the experimental data; their shape and colour indicate the number of photons associated with each excitation. The arrows indicate those points where two photon energies coincide. The line shows a linear interchange between bias current and excitation energy. The shaded area indicates the regime that is only accessible with multiphoton excitations. *Inset*: comparison of a nanodetector, a short (200 nm) wire, and a meander. We find that the response of the wire and meander coincides with that of the nanodetector, taking into account the difference in width between these three detectors by normalization to the width w_0 of the nanodetector.

our system when $I_b \approx I_c$. Around I_0 , we do not measure any dark counts in a 30 s interval. This demonstrates - suprisingly enough - that extrapolation to $E = 0$ does not yield the dark count rate.

Figure 4.2 demonstrates that the relation between bias current and photon energy required to have a constant detection probability is linear over one order of magnitude in energy. This result demonstrates that the detection process is not associated with any normal-state region that is formed in the SSPD. For a normal-core model, the energy dependence would be quadratic, as can be seen from a simple geometric argument that relates the lateral size of the obstruction made by the normal core to the photon energy [16]. For a model in which there is no normal state, the current-carrying capacity of the wire is linearly dependent on the number of remaining Cooper pairs and therefore on the photon energy.

We will now demonstrate that we can use our nanodetector as a model system of an SSPD. We compare our results with those on a $w = 150$ nm wide, 400 nm long wire and a conventional $w = 100$ nm meander detector⁵. The inset of Figure 4.2 shows a comparison of our three detectors. We take into account the width w of the detector by normalizing the energy scale to the width of the nanodetector, which enters through both the critical current and through the intrinsic $1/w$ scaling of the detection mechanism [16]. For our nanodetector, wire, and meander, the results superimpose. This demonstrates that our nanodetector functions as a model of an SSPD.

Figure 4.3 shows the experimental observations at $\lambda = 600$ nm, for the $n = 1$ to $n = 4$ photon regime. By restricting ourselves to one wavelength, we can improve the accuracy of our experiment by removing all systematic errors associated with changing wavelength⁶. This data is representative for the accuracy of our experimental runs at other wavelengths. We fit a general expression $I = I_0 - \gamma E^\alpha$ to this selection. As noted above, we expect to find $\alpha = 0.5$ for the normal-core hotspot model and $\alpha = 1$ for a diffusion-type model. For the vortex-based models, the expressions are more complex, but can be approximated by $\alpha = 0.5$ for the vortex nucleation model⁷, and by equation 1.6 for the vortex crossing model⁸[16, 24, 25, 33].

We find experimentally $\alpha = 1.00 \pm 0.06$, indicating good agreement with the diffusion model. We note, however, that since the most straightforward variant of the diffusion model predicts $I_0 = I_c$, this cannot be the whole story. We must therefore look for additional effects to explain the detection mechanism in SSPDs.

⁵More details may be found in the Appendix to this chapter.

⁶We will see in Appendix II of this chapter that at least some of those systematic errors may be associated with crossing the GaAs bandgap at $\lambda = 816$ nm.

⁷For the vortex nucleation model, we have set $\gamma = 0$ in the terminology of [16] throughout. This is a reasonable approximation for our experimental situation.

⁸In our original article, we claimed that the vortex nucleation model can be approximated as $\alpha = 0.75$. This is incorrect. We present here both the original fit for ($\alpha = 0.75$) and the fit to equation 1.6, which is the correct function. We note that this error does not alter the conclusions of this chapter.

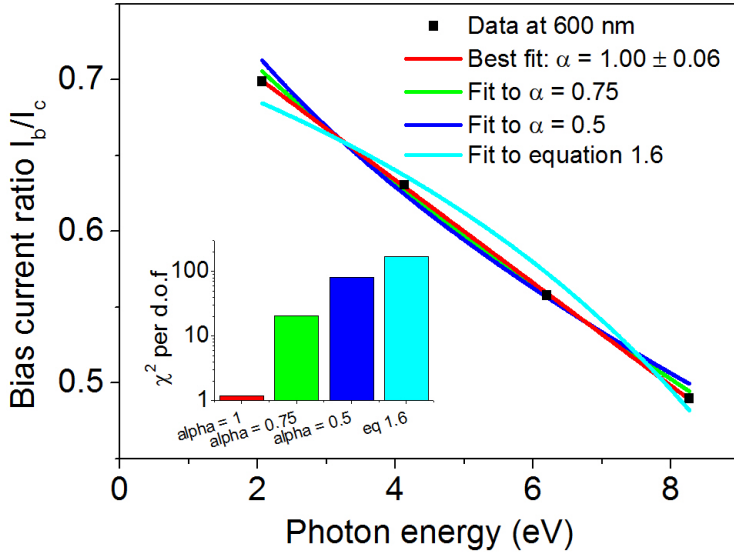


Figure 4.3: Experimental results on quantum detector tomography at $\lambda = 600$ nm. We show a single run of the experiment from Figure 4.2. To this data, which is free of the systematic error associated with changing wavelength, we fit a general expression $I = I_0 - \gamma E^\alpha$, where the value of α determines which model we are in. We find $\alpha = 1.00 \pm 0.06$, indicating good agreement with the linear (diffusion) model. We plot fits to $\alpha = 0.5$ and $\alpha = 0.75$ for comparison, as well as to equation 1.6. *Inset:* χ^2 of the four fits. We find that scenarios with a nonlinear energy-current relation are strongly inconsistent with our experimental data.

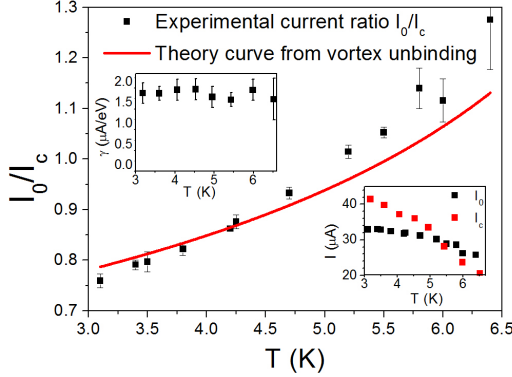


Figure 4.4: Temperature dependence of the fundamental current I_0 in the nanodetector, relative to the critical current. The red curve shows the temperature dependence of the ratio of the current associated with the vortex energy barrier (the barrier that a vortex has to overcome to enter the device), and the Ginzburg-Landau critical current [24, 25]. *Top inset:* Temperature dependence of the energy-current interchange ratio γ . This parameter, and the overall linear efficiency η are both temperature independent to within our experimental accuracy. *Bottom inset:* Temperature dependence of I_0 and I_c , separately. I_c follows the temperature dependence of the Ginzburg-Landau depairing current.

In Figure 4.4, we show the temperature dependence of the observed reference current I_0 , measured on the nanodetector, normalized to the experimental critical current. We obtain this plot by performing an experiment as shown in Figure 4.2 at various temperatures. We find experimentally that only the current scale I_0 is temperature dependent; the incoupling efficiency η and energy-current slope γ are independent of temperature. The temperature dependence of I_0 therefore completely describes the temperature behaviour of the device. I_c follows the Ginzburg-Landau temperature dependence, which is consistent with the result found on Nb bridges [84]. The key result from Figure 4.4 is that the temperature dependence of the reference current is different from that of the critical current.

We first discuss the implications of our results for the practical use of SSPDs. Around $T = 5.5$ K, we find $I_0 \approx I_c$. This means that above this temperature, there are energies for which the detector no longer operates fully as a single-photon detector. This observation explains the strong reduction in performance that detectors experience around this temperature. Note that with the usual semiclassical characterization, one can always find a regime where measured count rates are linear with input power by going to sufficiently low power, even at $p_1 \ll 1$. The transition from single to

multiphoton detection that we have found can therefore only be observed by the use of detector tomography.

Our experimental I_c follows the Ginzburg-Landau $I_c(T) = I_c(0)(1 - T/T_c)^{3/2}$ dependence of the depairing current, i.e. the current at which the Cooper pair binding energy is reduced to zero. The reference current I_0 has a different temperature dependence. As vortices are the other major effect in type-II superconductors, it is natural to consider whether the observed current scale pertains to vortices. Vortices are affected by the Lorentz force, and an unpinned vortex would be driven across the width of the strip by the bias current. We must therefore consider dynamic vortex scenarios.

Based on the above considerations, we compare the reference current to the current scale that governs the height of the energy barrier for a vortex crossing [24, 25]. The ratio I_0/I_c contains an explicit temperature dependence through the superconducting coherence length $\xi(T) \sim (1 - T/T_c)^{-0.5}$ ($T_c = 9.6$ K). In Figure 4.4, we plot this temperature dependence. The existence of an alternate current $I_0 \neq I_c$ in SSPDs, and the observation that the temperature dependence of this current follows the temperature dependence of the binding energy of a vortex is evidence for the fact that the detection mechanism is vortex-based and that the temperature dependence is set by this energy.

SSPDs can also be used in the keV regime, either for detecting X-ray photons [85] or for detecting ions. The experiment by Suzuki *et al.* [75] on ion detection in 800 nm wide, 10 nm thick detectors has clearly demonstrated that the normal-core hotspot model is correct in the keV range. This is understandable, as a single injection of a large amount of energy will be enough to break all the Cooper pairs at a single position along the wire, leading to a normal-core scenario. There must therefore be a typical energy where the diffusion-based scenario gives way to a normal-core scenario. By fitting only low-energy events and extrapolation to high energies, we can check whether all our results are described by a single model. We find that this is the case, and therefore conclude that this transition occurs at an energy higher than 8 eV, for our system.

The overall conclusions which may be drawn from our results are that both vortices and diffusion play a role in the detection event. Returning to Figure 4.1, we may therefore conclude that scenario d) is the one that corresponds closest to reality. We note, however, that the particular vortex crossing model proposed by Bulaevskii *et al.* has a energy-current dependence that does not correspond to our experimental observations. This point was addressed in a recent article by Engel *et al.* [28], which combines diffusion and vortex crossing in a numerical simulation. However, both the numerical simulation and the theoretical work predict $I_0 = I_c$ for the limit $T \rightarrow 0$. More theoretical work is needed to explain our results.

4.4 Conclusion

We have demonstrated experimentally that the dependence between the excitation energy and bias current required to produce a detection event in a superconducting single-photon detector is linear. The exact linear dependence in the experiment is consistent with a detection model that relies on the diffusion of quasiparticles produced by the initial excitation. Other models produce behaviour that deviates significantly from linear dependence.

We find a current scale which characterizes the response of the detector which is unequal to the critical current of the device. When the temperature is increased, we find that the observed current scale exceeds the critical current at the same temperature where the SSPD response degrades. We observe no temperature dependence in the other observed parameters, which together provide a complete description of the detector. We therefore conclude that we have localized the problem of temperature dependence of SSPDs to a single current scale. The observed temperature dependence matches reasonably well with a theory describing the crossing of a single vortex. From our results, it is clear that at optical frequencies, quasiparticle diffusion and vortex unbinding are the two main ingredients in any model of SSPD behaviour.

4.i Appendix: Supplementary Material⁹

4.i.1 Detector Tomography

Detector tomography provides the probability of a detection event without relying on any assumptions about the detector. We therefore do not need to consider the inner workings of each model, but treat them agnostically, i.e. no assumptions about the properties of the detector or the parameters of the models go into our experimental results. This is particularly necessary in the present situation, where there is no consensus on which physics is relevant for the photodetection process.

Our method relies on observing nonlinearities in the detection probability of the device as a function of input power. For this reason, we are completely insensitive to the amount of overlap between the light beam and the active area of the detector [67]. This is a requirement, because our detector is subwavelength, and therefore the spatial overlap between our detector and the input mode is necessarily small. Detector tomography enables us to simultaneously measure the fraction of detection events caused by each multiphoton process. We model the detection efficiency by:

$$R_{click} = 1 - e^{-\eta N} \sum_{n=0}^{n_{max}} (1 - p_n) \frac{(\eta N)^n}{n!}, \quad (4.1)$$

where R_{click} is the observed detection rate and N is the mean photon number of the incident coherent state. n_{max} is the photon regime which the detector is operating in, which is determined by model selection (see below). η is the linear efficiency (which is discarded in further analysis) and the p_n are the quantities of interest: they represent the probability of a detection event, given that n photons are absorbed in the detector.

4.i.2 Determination of the Photon Regime

The parameter n_{max} in equation 4.1 sets the maximum number of photons that is still participating in the detection process in some nontrivial way, i.e. which photon regime the detector is in. We determine n_{max} by making a series of fits to each n (up to $n = 6$) and computing the goodness-of-fit statistic χ^2 per degree of freedom. For a good fit, we should find $\chi^2 \approx 1$. First, we reject all fits with $\chi^2 \gg 1$. Then, we pick the fit that has minimal χ^2 . Based on model selection theory, we should use the Akaike Information Criterion $AIC = \chi^2 + 2n_{max}$ to pick the model which describes the data with fewest parameters [86]. In practice, we find that well-fitting models all have the same χ^2 and badly fitting models produce much larger χ^2 . Therefore,

⁹This section is based on the Supplementary Material to J.J. Renema *et al.*, Phys. Rev. Lett., **112** (11), 117604 (2014).

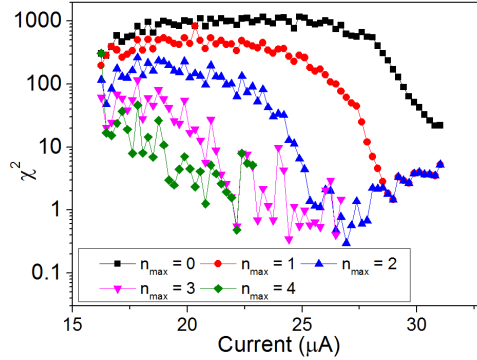


Figure 4.5: Goodness-of-fit parameter χ^2 as a function of bias current. This experiment was performed on the nanodetector. $\chi^2 \approx 1$ indicates a good fit. Each line corresponds to a model where the detector is in a particular multiphoton regime. From this graph, we determine the multiphoton regime which the detector is in. To find the appropriate photon regime, we select the curve with minimal χ^2 that has the lowest n_{max} .

minimizing the AIC is equivalent to finding the first model with a low χ^2 , which is the procedure that we described in Chapter 2.

Figure 4.5 shows a typical result (in this case for a measurement at $\lambda = 600$ nm) of χ^2 for the various models as a function of bias current. The top curve (black squares) shows the detector modelled as a one-photon detector, i.e. $p_i = 1$ for $i \geq 1$ (i.e. $n_{max} = 0$). For currents above $28.5 \mu\text{A}$, the detector can be described by a model with $p_i = 1$ for $i \geq 2$ (i.e. $n_{max} = 1$). When we decrease the current below $28.5 \mu\text{A}$, the detector is well described by a model with $p_i = 1$ for $i \geq 3$ (i.e. $n_{max} = 2$), and so on.

4.i.3 Experiment

The detectors were illuminated with a Fianium broadband laser, with a specified pulse duration of 7 ps and a repetition rate of 20 MHz. In the present experiment, we used optical wavelengths from 460 nm to 1650 nm. For each experimental run, we selected a band of $\Delta\lambda = 10$ nm via dichroic mirrors, high and low edgepass filtering and bandpass filtering with a dielectric filter.

It was reported that operating the detector at high count rates compared to its intrinsic reset time can result in a spurious nonlinear response [87]. To avoid this issue, we discard all data where the fraction of pulses that results in a detection event is higher than $e^{-2} \approx 0.14$.

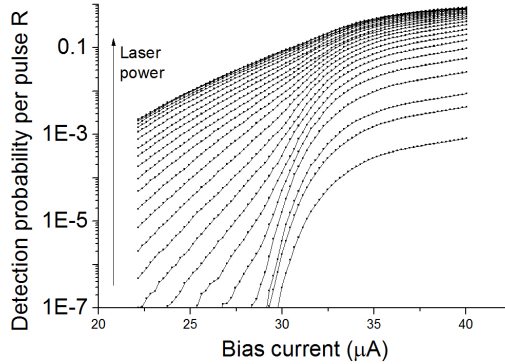


Figure 4.6: Raw experimental data for a single measurement run at 1400 nm. We plot the observed detection probability per pulse as a function of bias current, for various laser intensities. Note that the laser powers are not spaced uniformly.

4.i.4 Example

To illustrate our measurement procedure, we demonstrate our data processing on the experimental run at $\lambda = 1400$ nm. In Figure 4.6, we plot our raw data. We measure the detection probability as a function of bias current at various laser powers.

This figure is best understood by reasoning outwards from the low-power graph at the bottom-right. At low powers, we measure the usual response which is also seen in SSPDs: at low currents, we find a region where the detection rate increases rapidly when the bias current is increased, whereas at high currents the response is more or less independent of bias current. For SSPDs, the flatness of this plateau is sometimes taken as an informal measure of the quality of the device. In our case, this rule of thumb is not applicable since we have an intrinsically nonuniform geometry. We discuss this point further in a separate section of this Appendix.

When we increase the laser power, two effects occur. At low currents, we observe detection events with a superlinear dependence on power, indicating that we are in a multiphoton regime. Secondly, at high currents we observe saturation of the detector.

Figure 4.7 shows the data processing. We convert the bias-current dependent curves into power-dependent curves. The arrow indicates the direction of increasing bias current. We fit equation 4.1 to these curves, and then apply model selection as described above. We consistently find that we are able to fit our entire data set with equation 4.1, obtaining values for η , and p_i for each bias current.

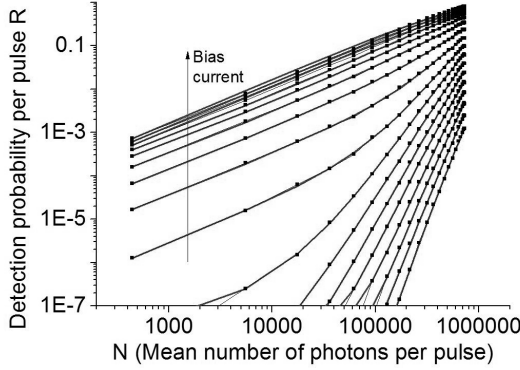


Figure 4.7: Experimental data as a function of mean photon number per pulse. The black points show the experimental data from figure 4.6, but plotted as a function of photon number. The black curves show fits to equation 4.1. We select the optimal fit via model selection.

In Figure 4.8, we plot the measured values of p_i as a function of bias current. Furthermore, as a comparison, we plot the scaled low-power detection probability. The fact that the low-power count rate and p_1 have very similar functional dependencies on I_b serves as a consistency check. At higher photon numbers, the relation between observed count rates and p_i is nonlinear, as can be seen from equation 4.1.

The dashed line represents the threshold criterion used for the figures in the main text. We note that the threshold criterion is far away in current from the current where our model selection switches from one model to the next. Therefore, the accuracy with which we can determine the threshold current is independent of the precise method of model selection.

4.1.5 Error Analysis

The accuracy with which we can measure p_i is crucial to our argument regarding the linearity of the energy versus bias current relation at constant p_i . We perform error analysis in three different ways. First, we obtain estimated errors from the fit to equation 4.1, which give us errors on the point $p_i = 0.01$ through standard error propagation techniques. We validate these errors in two ways. First, we perform a calculation where we split a data set where we integrated for 30 s at each measurement setting into three blocks of 10 s. We analyze these blocks separately and compare the spread in observed p_i . Secondly, we perform several subsequent experiments under exactly the same conditions, and compare the spread in p_i . From this analysis, we conclude that $\Delta I_b = 50$ nA is a reasonable estimate of our

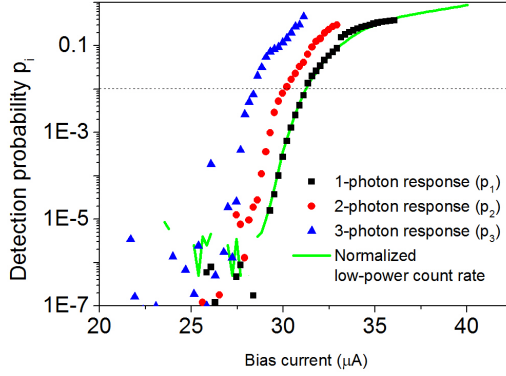


Figure 4.8: Detection probabilities for absorbed photons as a function of bias current.

error in determining the point where $p_i = 0.01$. The fact that the error on subsequent experiments is not larger than that of a series of interleaved measurements is proof that our set up is stable over the required measurement times.

4.i.6 Samples

The properties of our three samples at 3.2 K are:

	nanodetector	wire	meander
Width w (nm)	220	150	100
Thickness (nm)	5	4.7	5
Length	-	200 nm	105 μm
I_c (μA)	44	28	23
I_0 (μA)	33.9	21.5	17.6
γ ($\mu\text{A}/\text{eV}$)	1.6	2.7	4.4

4.i.7 Localization of the Detection Response¹⁰

Since our detector is inherently inhomogeneous in width, it is necessary to consider whether photon absorption events in the areas far away from the center of our detector can be responsible for detection events. We demonstrate that this is not the case by estimating first the size of an excitation at the center of the detector, and then demonstrating that excitations which are further away than that do not cause detection events.

¹⁰See also Chapter 7.

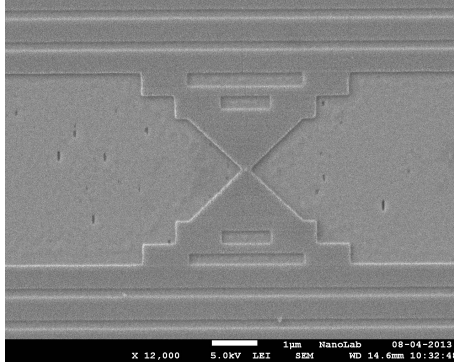


Figure 4.9: SEM image of a detector nominally identical to the one used in this experiment. The active area of this device is in the very center of this image. The white bar represents a distance of 1 μm .

First, estimates of the timescale involved in the detection process range from $\tau = 2.7$ ps [28] to $\tau = 20$ ps [40]. Combined with a diffusion coefficient of $D = 0.5$ cm^2/s , this gives an excitation size of $x = 10\text{-}30$ nm. We note that the lower estimate is close to the resolution with which our constriction is defined. For photons which are absorbed further away than that, the current density is much lower due to the large taper angle of 45 degrees. For example, if the detector is operated at $I_b/I_c = 0.75$ at the constriction, the current density 50 nm away from the constriction will be only $I_b/I_c = 0.5$. Moreover, the additional width of the detector at that point means that the detection probability is correspondingly lower.

From the scaling demonstrated in the inset in Figure 4.2, we can estimate that when the detector is in the 1-photon regime for 400 nm photons on the constriction, it will be in the 4-5 photon regime for photons absorbed 50 nm away from the constriction. The orders of magnitude discrepancy in count rate associated with such a difference in photon regimes means that the contribution from areas outside the narrowest part of the constriction is negligible. This demonstrates that we are justified in considering our detector as a single line-segment.

4.i.8 Temperature Dependence of λ_c

As a consistency check, we demonstrate that our work reproduces previous experimental results that were obtained without the use of tomography. In previous work [73], the temperature dependence of the SSPD was described in terms of a cutoff wavelength λ_c , in the form of an empirical formula for the detection rate $R(\lambda) = 1/(1 + (\lambda/\lambda_c)^n)$. This cutoff wavelength was observed to be both temperature and current-dependent. At high currents, the temperature dependence is stronger.

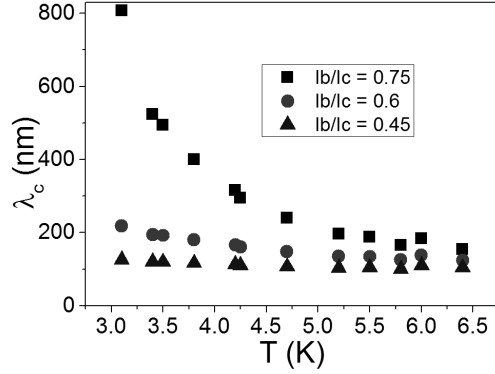


Figure 4.10: Temperature dependence of the cutoff wavelength as a function of relative bias current.

We compare our results to those of [73] by converting our energy-current dependence into a cutoff wavelength. The criterion for λ_c is equivalent to $p_i = 0.5$. We solve the equation $\alpha I_c = I_0 - \gamma E$ for $E = hc/\lambda_c$, where $\alpha = I_b/I_c$ is the bias current ratio. In Figure 4.10, we plot the result of this computation. We find that we are able to reproduce the experimental result from [73]: the observed current scale reproduces the behaviour that was observed for a TaN SSPD. In particular, at low currents, the cutoff wavelength is small (high energy) and barely dependent on temperature. At high currents and low temperatures, the cutoff wavelength increases and is in the infrared. This reproduces the earlier experimental observation that it is the IR response of the detector that is most strongly affected by elevated temperatures.

4.ii Appendix: Wavelength Measurements with an SSPD

The observation that a superconducting single-photon detector is sensitive to the overall energy of the excitation naturally gives rise to the question whether this effect can be used to measure the wavelength of an incident beam, and if so how accurately. Motivated by this question, we performed quantum detector tomography on a 150 nm wide superconducting single-photon detector in a narrow wavelength range, from $\lambda = 840$ to 900 nm, using a series $\Delta\lambda = 10$ nm FWHM filters in steps of 20 nm. We increased the integration time in our experiment to 10 s per point, which leads to increased accuracy in our measurements. Furthermore, we enhanced the count rate somewhat (from $\ll 1$ MHz to ~ 0.5 MHz) which increases the overall accuracy with which we can determine p_1 .

The natural application of such a device would be as a spectrometer, as was already proposed in 2007 by Reiger *et al.* [88]. The operating principle of an SSPD-based spectrometer would be that the bias current is swept, and the counts recorded. Using the fact that the threshold current (i.e. the current at which one observes detection events) is different for each wavelength, one could in principle reconstruct the spectrum from the observed count rate dependence on bias current.

There are several good reasons to be skeptical about the practicality of such a device. First of all, it has energy resolution only in a statistical sense. Unlike a grating-based spectrometer, there is no intrinsic information gained about each photon individually, only about the whole in a statistical sense. This means first of all that the amount of signal is abysmal (the device operates by deliberately not detecting a large portion of the incident photons) and secondly that sources which are varying in time cannot be characterized. A second reason is that it is unclear how narrowly-spaced wavelengths would be separated. The spectral width $\Delta\lambda$ of our illumination in this experiment is already larger than the observed accuracy. While we will show that we can measure the central wavelength of our incident laser beam with an accuracy of a few nm, it is unclear how two adjacent wavelengths would be separated. In [88], this was done for light of $\lambda = 900$ nm and $\lambda = 530$ nm, but this resolution is far away from any practical significance.

For these reasons, we include our results on this topic in this thesis more as a demonstration of the abilities of our methods and as an exploration of the ultimate accuracy of our system than as a concrete route to any practical application. However, since SSPDs operate across a broad range of wavelengths (from X-ray to mid-IR) and are robust for space applications, we cannot exclude that there is some application, perhaps in astronomy, at some exotic wavelength where the results presented here will prove useful.

We show the result of our quantum detector tomography experiment in Figure 4.11. We report data for four wavelengths: 900 nm, 880 nm, 860 nm

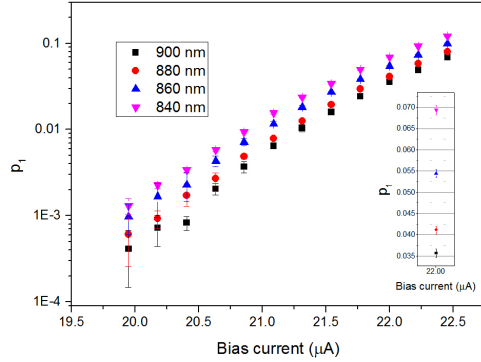


Figure 4.11: Quantum detector tomography of a superconducting single-photon detector at a series of narrowly spaced wavelengths

and 840 nm. We find the usual effects for SSPDs: lower photon energy as well as lower bias current lead to lower detection probability. In the inset of Figure 4.11, we show a zoom-in on one experimental point, demonstrating the observed values of p_1 at a bias current of $22.0 \mu\text{A}$. The error bars in the figure correspond to the error estimate from our tomographic fits.

In Figure 4.12, we show the accuracy which is computed from the experimental data presented in Figure 4.11. We define this accuracy as $2(p_1(\lambda_1) - p_1(\lambda_2))/(\sigma_{p_1(\lambda_1)} + \sigma_{p_1(\lambda_2)})$, where σ is the error with which we determine the value of p_1 for a particular wavelength. That is: we measure how many error bars away two adjacent points are. This is a measure of how accurately we can determine the center wavelength of a particular quasi-monochromatic light source.

We find that this accuracy depends on the applied bias current. This is a consequence of our measurement technique: since we use the same range of powers for the tomography experiment at each current, we achieve lower count rates and hence higher errors when p_1 is lower. However, in an application where an unknown source has to be characterized, the intensity of that source typically cannot be increased by the experimenter, and at any given intensity the count rate at low bias currents will be lower. We therefore conclude that these error estimates describe a reasonable scenario.

We note that we have improved on the result presented in [88] by more than an order of magnitude. Two orders of magnitude (i.e. an accuracy of a few Angstrom) could easily be reached by decreasing the width of the wire, which makes the energy-current relation more steep, thereby improving energy resolution at a given bias current resolution.

In the inset of Figure 4.12, we plot the extrapolated accuracy with which we can determine a central wavelength as a function of that wavelength.

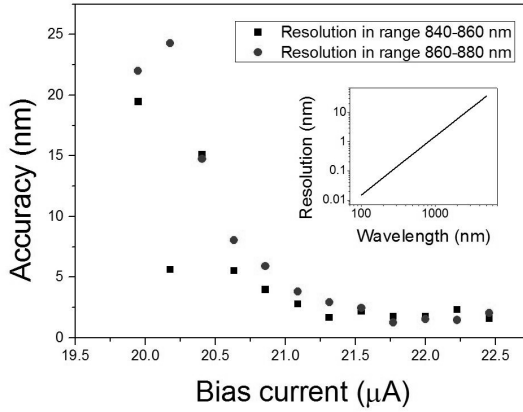


Figure 4.12: Observed wavelength accuracy as a function of bias current. We find that for higher bias currents the accuracy becomes better. The high-accuracy plateau between 21.5 and 22.5 μA corresponds to a accuracy of 1.4 nm. *Inset:* Extrapolated wavelength accuracy.

Since we expect our energy resolution to be constant, we obtain a wavelength resolution proportional to $1/\lambda^2$. We expect this wavelength resolution to break down at the point where the excitation becomes energetic enough for the normal state to start playing a role in the detection mechanism, which is predicted to happen at a photon energy in the UV [28]. In this energy range, the linear dependence will give way to a sub-linear dependence, reducing the resolution.

Lastly, we note one additional effect which becomes visible when zoomed in to this particular wavelength range: there is a step in the energy-current relation between 840 and 800 nm. While more work is clearly needed to explain this effect, it is intriguing that the first point which breaks the trend occurs at 820 nm. We note that our 820 ± 5 nm light coincides with the bandgap of GaAs at low temperatures, which is at 816 nm. We speculate that this effect is related to the absorption of light in our substrate, but note that this effect cannot be explained by invoking only the heating of the sample due to the increased absorption: as noted in the main text, this would decrease the amount of current required for a detection event rather than increase it. Noting that perhaps this effect is responsible for some of the spread between wavelengths $\Delta I = 250 \mu\text{A}$ in Figure 4.2, we pass over this point without further interpretation.

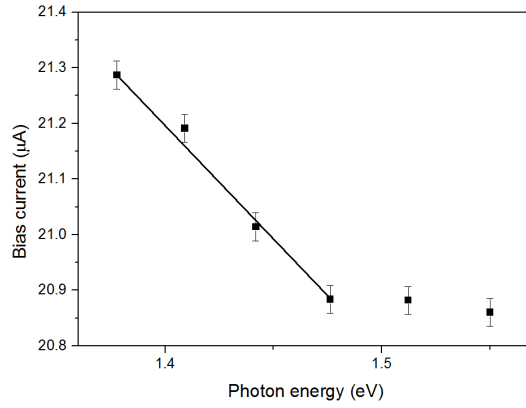


Figure 4.13: Experimental observation of a step in the energy-current relation, around 820 nm. We speculate that this effect is due to crossing the bandgap of GaAs at 816 nm.

Chapter 5

Position-Dependent Internal Detection Probability in a Nanowire Superconducting Single-Photon Detector

We probe the local nature of the detection probability in nanowire superconducting single-photon detectors at the nanoscale. By using detector tomography, we demonstrate that the detection probability depends on the distance from the edge of the wire at which a photon is absorbed. We probe this effect with a ~ 10 nm resolution. We find that there is qualitative agreement with the diffusion-based vortex crossing model but not with other models.

5.1 Introduction

Nanowire superconducting single-photon detectors typically consist of a 60-100 nm wide, current-carrying, thin, superconducting film [1]. These photodetectors have favourable properties such as high efficiency, low dark count rate and fast reset time [89], and are therefore a key resource for various technologies, such as quantum key distribution [90], interplanetary communication [6] and cancer research [91]. Recently, large steps have been made in the understanding of the internal working mechanism of such detectors.

While the picture is not yet complete, the current understanding of detection events in superconducting single-photon detectors is as follows: an absorbed photon breaks Cooper pairs through an avalanche process, causing a cloud of quasiparticles a few tens of nm in size to form in the superconducting film. This in turn causes the current to be diverted through the

unaffected parts of the wire. If the diverted current is sufficiently strong this causes a magnetic vortex to unbind from the edge of the detector. Under the influence of the Lorentz force, this vortex is pulled across the wire, dissipating enough energy to cause a transition to the normal state, leading to a detection event [17, 24, 25, 28, 33, 34, 72]¹. One unexpected implication of such models is a nanoscale variation of the internal detection efficiency (IDE), i.e. the probability that an absorbed photon is detected: the amount of bias current required to detect a photon of a given energy depends on the position in the cross section of the wire where the photon is absorbed [32, 34].

To observe this effect, one must introduce a variation in the absorption probability as function of position. This can be done by changing polarizations of the light incident on the detector, since light polarized orthogonal to the wire is preferentially absorbed in the center of the wire (see Figure 5.1). However, this introduces a complication: apart from a possible difference in internal efficiency once a photon is absorbed, the two polarizations are also not absorbed with equal efficiency in the first place [10, 11, 12, 13, 92].

In this work, we investigate the local IDE by using a tomographic method to separate the overall absorption probability from the IDE. We find and quantify a polarization-dependent IDE. Our results are consistent with previous qualitative observations [10, 93, 94]. We conclude that the field distribution inside the detector determines the position of the photon absorption event and that the local IDE depends on where the photon is absorbed.

We explore this effect experimentally by measuring the polarization dependence of the internal detection efficiency as a function of wavelength and bias current. From these data we reconstruct the position dependent internal detection efficiency of a 150 nm wide NbN wire with ~ 10 nm spatial resolution. We compare these data to an ab initio numerical calculation in the context of a diffusion-based vortex crossing model. From the good qualitative agreement with experimental data we conclude that, while this model may require some refinement, it contains the essential microscopic physics of the photon detection event in SSPDs.

5.2 Experiment

To measure the internal detection probability of the detector, we use quantum detector tomography (QDT)² [17, 36, 37, 43, 44, 48, 49, 60, 67, 72, 95]. QDT relies on illuminating the detector with a series of known quantum states of light - in our case coherent states - which together function as a probe of the detection statistics. By comparing the response of the detector to different photon numbers in the coherent light state, we can separate the one-photon detection probability p_1 from the overall probability η that a photon is ab-

¹See Chapter 4.

²See Chapter 2.

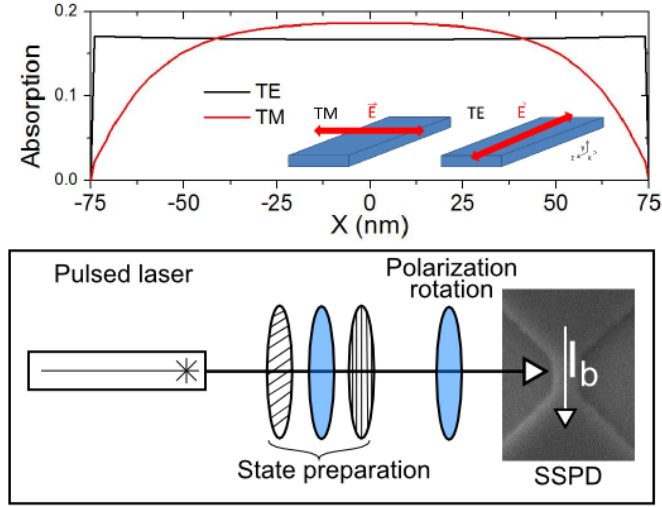


Figure 5.1: Sketch of our experiment. *Top*: Absorption as a function of position in the wire for parallel (TE) and perpendicular (TM) polarizations, calculated with an FDTD method (see text). *Inset*: Sketch showing the TE and TM polarizations. The red arrow represents the polarization of the electric field. *Bottom*: Experimental setup. Our laser pulses are tuned in intensity by a variable attenuator consisting of two crossed polarizers and a $\lambda/2$ wave plate. Polarization is set by an additional $\lambda/2$ wave plate. The image is a SEM micrograph of a detector nominally identical to the one used in this experiment.

sorbed³. From the fact that η is almost independent of bias current [67] and that it corresponds to the area of our detector, we identify p_1 with the IDE.

We perform our experiments on a 100 nm long, 150 nm wide NbN bridge patterned on a 5 nm-thick NbN sputtered on a GaAs substrate [47]. We read out the detector with the usual measurement setup based on a bias-tee to separate high-frequency detection pulses from the DC bias current, followed by a series of RF amplifiers and a pulse counter. At each combination of bias current, photon energy and polarization, we record the detector count rate as a function of input intensity. Our probe states were prepared by a broadband pulsed laser (Fianium, repetition rate 20 MHz) out of which we select a narrow wavelength band with dielectric filters⁴. We prepare the desired intensity and polarization by first attenuating the light with a combination of two crossed polarizers and a half-wave plate, and then setting the polarization with an additional wave plate (see Figure 5.1)⁵.

³For more information, see Appendix I.

⁴For a more extensive description of our setup, see Chapter 4, Appendix I.

⁵While in principle it is possible to achieve the desired combination of polarizations

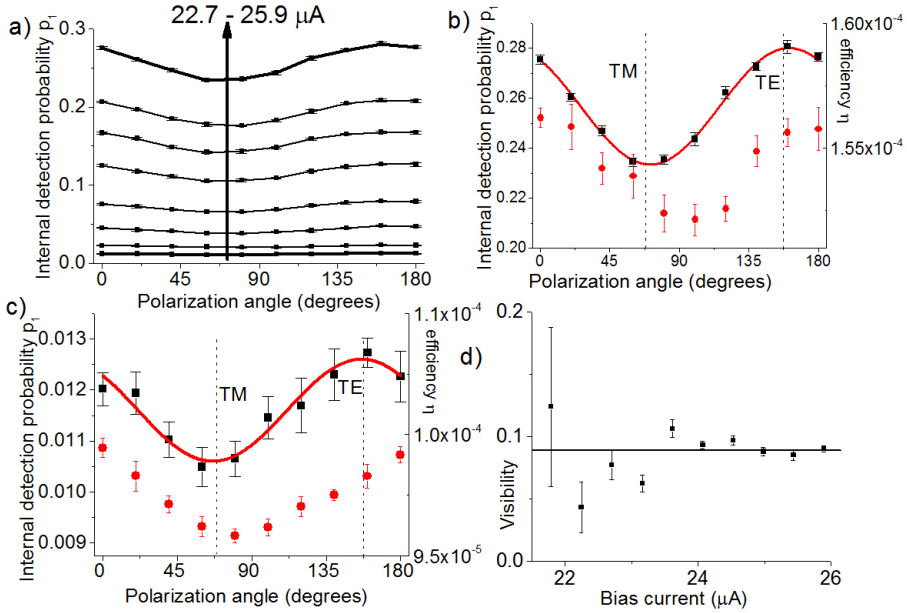


Figure 5.2: Experimental results on the polarization dependence of the internal detection probability at an excitation wavelength of 1500 nm. *a)* Internal detection probability p_1 as a function of input polarization, for different bias currents (0.5 μA apart). *b),c)* Zoom-ins on two typical experimental results (marked in thicker lines in *a)*) at different bias currents. We plot the internal detection probability p_1 (squares) as well as the absorption efficiency η (circles). The red lines are sine fits with a fixed period of 180 degrees. *d)* Visibility of the observed oscillation in p_1 as a function of bias current. We find that our results are consistent with a constant visibility of $V = 0.09$.

5.3 Results

Figure 5.2 shows that the internal detection probability of our device is dependent on polarization. We plot the internal detection efficiency p_1 as a function of the polarization of light with $\lambda = 1500$ nm. Each curve represents a different bias current, in steps of $0.5 \mu\text{A}$. We find that over the current range where our experiment has sufficient signal to noise ratio, the visibility $V = (p_{max} - p_{min}) / (p_{max} + p_{min})$ is independent of bias current. For this wavelength, we find $V = 0.09$. The error bars in Figure 5.2 are derived from a series of repeated experiments which are analyzed independently, for which we plot the mean and standard deviation⁶.

Our experiments show that the internal detection efficiency and external detection efficiency oscillate in phase when the polarization is rotated, with a minimum at TM polarization and a maximum at TE polarization. This demonstrates that absorption of TM-polarized photons is less likely to result in a detection. This polarization is absorbed in the middle of the wire. Our result therefore confirms the preliminary result of Anant *et al.* [10]: at a given bias current, the edges of the detector are therefore more efficiently photodetecting than the center of the wire.

In order to quantify the variations in local IDE we must compute the IDE as a function of polarization. We do this by multiplying the local optical absorption probability with the local IDE. We do this for each wavelength at which we measure the polarization-dependent detection probability.

Our strategy is to take the absorption profiles as given - since they are well studied - and to take the internal detection efficiency (IDE) profile as a free parameter and fit it to our experimental data. The rest of this chapter is structured as follows: first, we will describe the computation of the two profiles, resulting in a fit to our experimental data. Then, we will compare the resulting internal detection efficiency profile to one that we calculated from an ab initio theory.

To calculate the absorption distributions, we perform a series of numerical simulations at the wavelengths at which we conducted our experiments of the polarization-dependent absorption in the detector structure using a finite-difference time domain (FDTD) method (RSOFT Fullwave). We consider a 2D model of a 150 nm wide, 5 nm thick NbN wire on a semi-infinite GaAs substrate and an 80 nm thick HSQ layer on top of the NbN wire. The refractive index of NbN deposited film on GaAs is derived from spectroscopic ellipsometry measurements [96]. In these calculations we neglect the effect of the tapered parts of the bridge because they have little influence on the absorption in the central, photodetecting section⁷. In Figure 5.1, the result

and intensities using two independently rotating polarizers, we found that the effects of wedge in the polarizers preclude this solution.

⁶We will analyze the change in linear efficiency from $\eta = 1.6 * 10^{-4}$ to $\eta = 1.1 * 10^{-4}$ in Chapter 7.

⁷See Appendix I for details.

of this calculation is shown for $\lambda = 1500$ nm.

For the internal detection probability, we use the fact that the energy-current relation was measured to be of the form $I_{th} = I_0 - \gamma E$, [28, 17, 72] where I_{th} is the threshold current (i.e. the current where the detection efficiency is equal to some reference value), I_0 is the reference current⁸, E is the photon energy and γ is an experimental ratio which describes the interchange between bias current and photon energy. We postulate that this relation holds microscopically, i.e. $j_{th}(x) = j_0 - \gamma'(x)E$. Moreover, we must posit a relation between threshold current and detection probability. For this, we postulate the relation $P(x) = \min\{1, \exp(j_b - j_{th})/j^*\}$, with $P(x)$ the local detection probability, j_b the bias current density,⁹ and $j^* = 0.9$ GA/m² the low-detection probability scale which can be read off from the experimental data when converted to a bias current. This relation is motivated by the idea that at $P(x) < 1$ the detection process consists of tunneling through the energy barrier binding the vortices to the edge of the wire [23, 33]. With this set of assumptions, we are able to compute the polarization visibility for different wavelengths, with the $\gamma'(x)$ profile specified at 10 nm intervals as fit parameters.

Figure 5.3 shows the calculated and measured visibility of the polarization-dependent internal efficiency as a function of wavelength. We find that at long wavelengths there is a greater difference between the measured IDE for the two polarizations. The line in Figure 5.3 shows the result of our fit of the internal detection profile to the data. From the local IDE and the optical absorption probability, we compute the overall IDE. We find that we are able to reproduce the observed internal efficiencies with our fit. The left inset of Figure 5.3 shows the dependence of the polarization-dependent IDE visibility on current. We find that theoretically, the IDE visibility is independent of current, which is reasonable agreement with our experimental data.

The right inset shows the overall value of the single-photon internal detection efficiency, integrated across the wire. We observe that our curve predicts the right current for the roll-off at low detection probabilities, and that it reproduces the slow saturation of the detector at high currents. In this regime, parts of the detector are fully photodetecting, while other parts are still in a fluctuation-assisted regime [35]. The variations between the experimental data and the calculated values are less than a factor of 2. We stress that the two insets of Figure 5.3 are direct results of the internal detection efficiency profile inferred from the polarization measurements. We therefore conclude that our proposed internal detection probability profile is consistent with all of the observed properties of our detector.

⁸see Chapter 4.

⁹Throughout this Chapter, we assume homogeneous current flow, so the relation $j = I_b/(wd)$ holds.

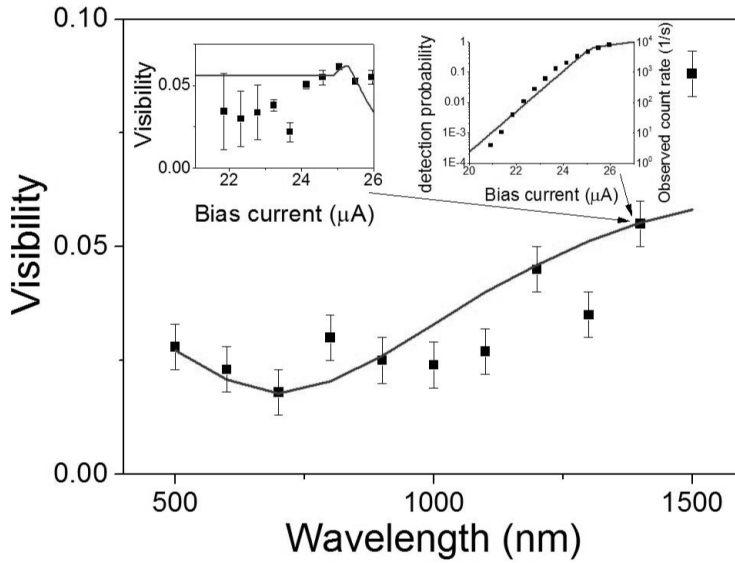


Figure 5.3: Wavelength-dependent visibility of the internal detection efficiency (p_1). The black squares show the experimental data. The line shows a fit of the internal efficiency profile, based on the diffusion-based vortex crossing model. *Left inset:* Measured (squares) and computed (line) visibility of the polarization-dependent oscillation as a function of bias current. *Right inset:* Observed (squares) and computed (line) values the integrated single-photon internal detection probability p_1 .

5.4 Comparison to Theory

Figure 5.4 shows the internal threshold current profile which comes from the fit to the wavelength-dependent polarization visibility data, for a wavelength of 1000 nm (see also Figure 5.3). For comparison with other experiments, we plot the overall bias current required to make a particular part of the wire fully photodetecting. We estimate the systematic error on the threshold current that is induced by uncertainty in the calculation of the optical absorption profiles¹⁰, shown in Figure 5.4 as a grey band around our data, which is particularly prominent around 50 nm. We find that this effect is negligible compared to the statistical error. Moreover, it shows an independent, *ab initio* calculation of the threshold current based on the model described below. We find reasonably good agreement between our observed experimental results and the theoretical values. From this, we conclude that our model is sufficiently detailed to model the detection process in SSPDs.

Our *ab initio* calculations of the position-dependent detection probability are based on a numerical model¹¹ that allows one to determine the threshold current for the detection of an absorbed photon of a given wavelength [28] and a recently proposed extension [32]. Based on a simple model of quasiparticle generation and diffusion, we determine the local reduction of the order parameter after the photon has been absorbed. Solving the continuity equation for the applied bias current for this inhomogeneous situation, we are then able to calculate the time evolution of the vortex-entry barrier. The minimum bias current that leads to a vanishing barrier height is defined as the threshold current for photon detection, as this will unavoidably lead to a vortex entering the strip. Its subsequent movement across the strip under the action of the bias current then leads to the formation of the initial normal conducting domain triggering the detection event.

We compute the threshold current for various photon energies and absorption positions across the strip and we find a linear relation between photon energy and threshold current for each position. This vindicates the assumption that the linear relation between current and photon energy holds on a microscopic level¹².

Our *ab initio* calculation gives a physical explanation for the enhanced efficiency at the edges of the wire in terms of our microscopic model. Comparing a photon absorption in the center of the wire to one at the edge, there are two differences. First, for an absorption event at the edge, the current density at the edge of the wire is reduced, due to the reduction in the number of superconducting electrons n_s . However, this is more than compensated by the reduction of the vortex self-energy, which is proportional to n_s . Vortices enter more easily when the superconductivity is weakened at their entry point, and that makes the detector more efficient at the edges.

¹⁰See Appendix I for details.

¹¹These simulations were performed by Andreas Engel at the University of Zurich.

¹²See Appendix I for details.

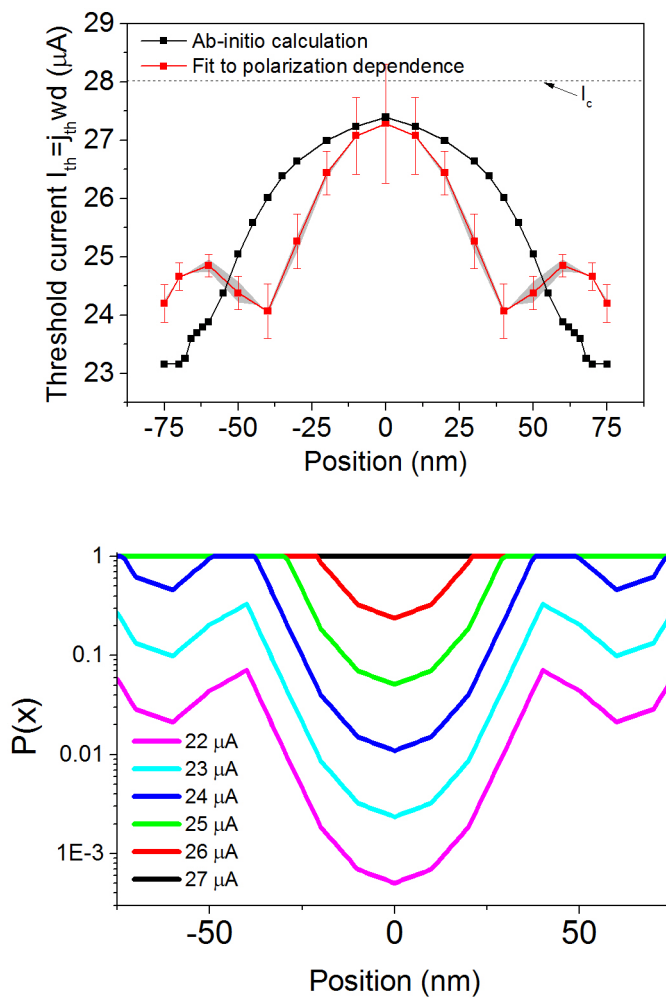


Figure 5.4: *Top panel:* Threshold current as a function of position across the detector, for our fit and our ab initio calculation, for a wavelength of $\lambda = 1000$ nm. The red curve shows the fit from Figure 5.3, the black curve shows our ab initio calculation. The grey band shows the systematic error coming from the uncertainty in the film thickness. The dashed line indicates the critical current. *Bottom panel:* Calculated position-dependent detection probability density as a function of bias current ($1 \mu\text{A}$ intervals). At a bias current where the edges of the wire are fully photodetecting, the detection probability in the middle of the wire is less than 1%.

The bottom panel of Figure 5.4 shows the consequences of the variation of the internal detection efficiency, evaluated for a photon with wavelength $\lambda = 1000$ nm. We plot the detection probability as a function of position for different bias currents. The effect of the position-dependent detection efficiency is quite strong: for a current of $25 \mu\text{A}$, photons absorbed at the very edge of the detector have 100% probability of causing a detection event, whereas photons absorbed at the center of the wire have only 3% probability.

5.5 Discussion and Conclusion

We note that there is some disagreement in literature about the shape of the internal detection probability curve. The alternative model of Zotova *et al.* [34], which is based on the Ginzburg-Landau formalism, naturally takes into account vortex entry. However, it disregards quasiparticle diffusion and implements a hotspot with hard boundaries. The results from this model disagree qualitatively with our experimental results: there, a W-shaped threshold current profile is predicted, with threshold currents at the edges almost as high as in the center of the wire. The discrepancy between their model and ours occurs precisely at the point where their 'hard' hotspot touches the edge of the wire. We speculate that both models, if refined more, will likely converge in their predictions.

In conclusion, we have demonstrated via detector tomography that the internal detection probability of an SSPD depends on the distance from the edge of the nanowire at which the photon is absorbed. We have probed this effect with a resolution of approximately 10 nm. This effect occurs in addition to the well-known effect that photons of parallel polarization are more efficiently absorbed in the wire. From the wavelength dependence of this effect we have derived a spatial profile for the local internal detection efficiency, which is in good agreement with theoretical calculations done in the context of the diffusion-based vortex crossing model. From this, we conclude that this model contains the essential features for a complete microscopic picture of the detection model in SSPDs. These results pave the way for quantitative theoretical results on the detection mechanism in SSPDs.

5.i Appendix: Supplementary Material

5.i.1 Quantum Detector Tomography

The purpose of this section is to review quantum detector tomography as a technique, and to demonstrate that we can separate the change in internal detection probability associated with a change in polarization from the change in overall efficiency. This section consists of three parts. First, we review the basics of quantum detector tomography. Then, we investigate the input power dynamic range requirements of our experiment. Lastly, we demonstrate that our experiment is accurate enough that we can reject the alternate hypotheses that our results are entirely attributable to a change in only either the internal or external detection efficiency.

5.i.1.1 Tomography Basics¹³

The goal of quantum detector tomography is to find the photodetection statistics of an unknown detector in the number state basis, i.e. to find the probability of a particular detection outcome given that n photons are incident on the detector. To probe these statistics, a collection of known quantum states of light is used. The detector is probed sufficiently many times with each state to accurately determine the probability of each possible experimental outcome (i.e. a detection event) for each input state. Since the probability distribution of photons in the states is known and the probability of each outcome has been measured, it is possible to determine the probability of each outcome given a certain number of photons.

In experimental practice, it is convenient to use the coherent states for this, which have a Poisson-distributed probability of photon numbers: $\Pi_i(N) = e^{-N} N^i / i!$, where N is the mean photon number, which can be determined classically, and i indexes the Fock states. These states are readily produced by a laser, and the mean photon number can be adjusted by attenuation, giving straightforward access to a sufficiently large set of quantum states. We denote the probability of the k -th experimental outcome to the j -th test state $R_k(N_j)$. The probability for i photons to produce the k -th experimental outcome $p_{k,i}$, which is the desired quantity, can then be found by solving the matrix equation:

$$R_k(N_j) = \Pi_i(N_j) p_{k,i}. \quad (5.1)$$

An SSPD has only two outcomes, a detection event (click) or the lack of a detection event (no click), and because overall probabilities must sum to 1, it is sufficient to consider only one of these. In Chapter 2, we modified equation 5.1 to make it usable in the case where only a very small fraction of the photons participates in the detection process. We did this by introducing

¹³See also Chapter 2.

a separate quantity η which describes the overall linear efficiency of the detection process. We arrive at:

$$R_{click}(N) = 1 - e^{-\eta N} \sum_{n=0}^{n < n_{max}} (1 - p_n) \frac{(\eta N)^n}{n!}, \quad (5.2)$$

where R_{click} is the observed detection rate as a function of input power, η is the overall efficiency with which photons participate in the detection process, and p_n represents the probability that the n -photon absorption event results in a photodetection event.

To fix the additional degree of freedom introduced by the linear efficiency, we must introduce an additional assumption. The essential assumption behind our modified version of quantum detector tomography is that there is some unknown but large photon number for which the count rate tends to a known, constant value¹⁴, in our case $R_{click}(N \rightarrow \infty) = 1$. For an SSPD, the assumption is well justified by the fact that high-energy excitations are known to be more efficiently detected than low-energy ones. It is therefore not unreasonable to assume that we have $p_n = 1$ for sufficiently large n_{max} . At these powers, we can fix η , and find the nonunity $p_{n < n_{max}}$ from the low count rate values.

The resulting procedure is illustrated in Figure 5.5, where we plot a data set from Chapter 2 to demonstrate the procedure. At high powers, we assume $p_n = 1$, which enables us to fix η . At lower light powers this description becomes inadequate, and we must adjust p_n to fit our data. The threshold value n_{max} for which $p_{n \geq n_{max}} = 1$ can be found via model selection. In the present experiment, we are working in the regime where only nonlinearities at the single-photon level play a role, so $n_{max} = 2$ throughout. The only exception is the multiphoton experiment reported on in Section 5.6.2.

5.i.1.2 Dynamic Range

From the discussion above, it is clear that sufficient dynamic range in input powers is the essential requirement for quantum detector tomography. In order for the procedure to work, sufficiently high powers must be taken into account to obtain an adequate measurement of the saturation behaviour of the detector. In order to ascertain whether this is the case in our experiment, we perform the following numerical procedure: we carry out detector tomography on our entire ensemble of data points. Then, we remove the data point at highest power, perform tomography again, and repeat this procedure. If we have sufficient dynamic range in our experiment, we expect to find that our results are independent of the specific choice of probe states.

¹⁴We note that in Chapter 2 [67], we claimed that the requirement is saturation, i.e. $R_{N \rightarrow \infty} = 1$. While this is by far the most natural case, in principle it is possible for a detector to have $R_{N \rightarrow \infty} \neq 1$, for example the one-element detection probability of a multi-element detector, which has $R_{N \rightarrow \infty} = 0$. Equation 5.1 can be trivially rewritten to accommodate this case.

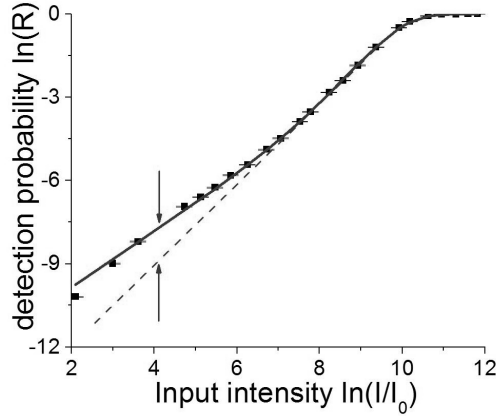


Figure 5.5: Sketch of quantum detector tomography (data taken from Chapter 2). We measure the response of an SSPD at various input powers. The solid line shows the fit to equation 5.2 for this data set. The dashed line shows the low-power extrapolation from the high-power data.

Figure 5.6 shows that this is indeed the case. We plot the internal detection probability p_1 as a function of the dynamic range in our probe states, for one data set of our experiment (1500 nm). We find that for dynamic ranges > 150 , our result is independent of which subset of our data we choose. This data set is representative of our full set of experimental results; we typically find values between 100 and 300 for the minimum dynamic range requirement. This demonstrates the robustness of our result.

5.i.1.3 Constant p_1 and Constant η

Lastly, we demonstrate that we are able to reject the alternative hypotheses that our experimental results can be explained by only a polarization-induced modulation in either p_1 or η . To ascertain this, we perform the following analysis: at each set of experimental settings (input wavelength, input power, bias current, polarization) we record a series of independent measurements. Then, we process these measurements separately. This gives us a measure of the statistical spread of our results.

In Figure 5.7, we plot the result of this procedure for one data set at 826 nm. Each set of symbols of the same colour represents ten realizations of the same experimental setting, and the spread within each colour is therefore a measure of the statistical spread in our experiment. We find that there is negative covariance between internal and external efficiency. However, the spread which this covariance causes is much smaller than the typical polarization-induced shift in either p_1 or η . The two dashed lines indicate the

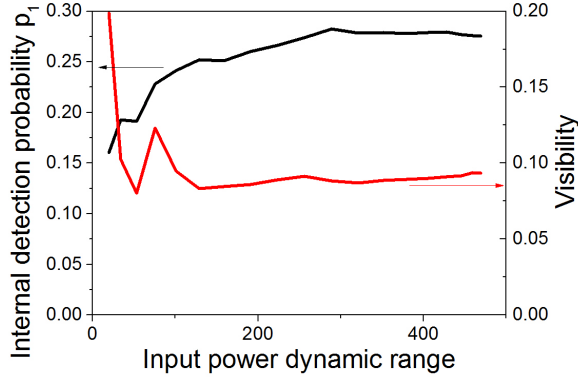


Figure 5.6: Quantum detector tomography at different dynamic ranges in the input power. We plot the internal detection probability as a function of bias current for a given polarization at fixed bias current, at an excitation wavelength of 1500 nm. The red curve shows the observed visibility for the data set to which this polarization belongs as a function of dynamic range. We find that for a dynamic range > 150 , the observed visibility is independent of the chosen range. This indicates that at sufficient dynamic range, our results are independent of the choice of input powers.

alternative hypotheses in which only either p_1 or η is polarization-dependent. It can be seen that a large part of our data is far away from these two lines. From this, we conclude that both internal and external effects are necessary to explain our measurements.

5.i.2 Multiphoton Polarization Effects

Detection events in SSPDs can also occur via multiphoton excitation [1, 67]. We performed an experiment at 826 nm where we illuminate the detector with sufficient power to cause two-photon processes at lower bias current. Figure 5.8 shows the results of this experiment. We find that also for multiphoton processes, the internal detection efficiency is position-dependent. We find that the visibility is a factor 2-3 higher for the 2-photon excitations than for the single-photon excitations.

We can offer two partial explanations for the enhanced visibility. First, we demonstrated in Chapter 2 that multiphoton excitations are equivalent - at least in their energy-current dependence - to single-photon excitations of the same energy. From our simulations of the internal detection efficiency, we find that the difference in threshold current between the edges of the wire and the center decreases with increasing photon energy. We therefore expect two 826 nm photons to respond similarly to a single 413 nm photon

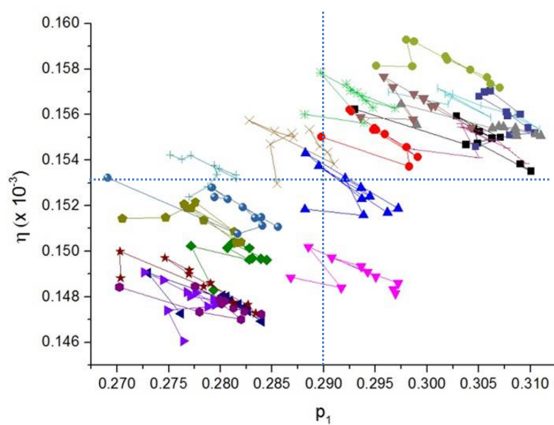


Figure 5.7: Experimental test of the statistical relevance of our result. Each set of symbols represents a single experimental setting, the spread between them is a measure of the statistical uncertainty in our experiment. There is a negative covariance between p_1 and η within each experimental setting, as expected.

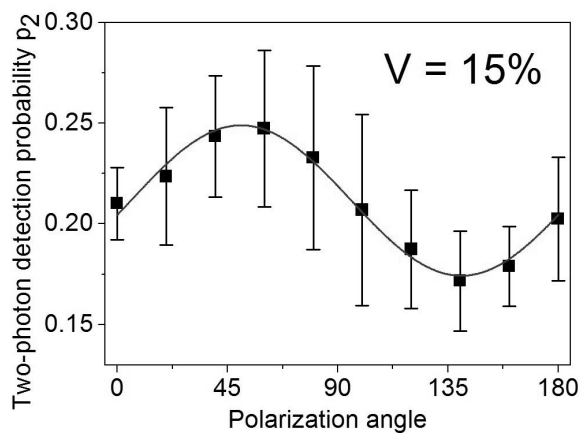


Figure 5.8: Multiphoton polarization-dependent absorption. We plot the two-photon detection probability p_2 as a function of polarization angle. The line shows a sine fit with a fixed period of 180 degrees to the data.

and experience a greater difference in detection efficiency. A second effect is that, qualitatively, we expect the two-photon absorption probability to be more sharply peaked at the edges of the wire. However, a full quantitative investigation of this multiphoton effect would involve computation of the internal detection efficiency for each possible two-photon absorption scenario, which is beyond the scope of the present work.

5.i.3 Numerical Detection Model

The simulation of the quasiparticle distribution after the absorption of a photon is based on the model described in [28]. Here, we will repeat the main features and assumptions of this model. It is assumed that the photon excites one electron with energy hc/λ . This electron moves in the film with a diffusion constant D_e . It thermalizes via inelastic scattering with other electrons/Cooper-pairs and the lattice. Neglecting details of this thermalization process, an exponential increase of excess quasiparticles is assumed with a time constant τ_{qp} and an overall efficiency ς [15]. The excess quasiparticles themselves are also subject to diffusion with a temperature dependent diffusion constant $D_{qp} < D_e$ and eventually recombine to form Cooper-pairs on a time-scale $\tau_r \gg \tau_{qp}$. This can be described by the following coupled differential equations [28]:

$$\frac{\partial C_e(r, t)}{\partial t} = D_e \nabla^2 C_e(r, t) \quad (5.3)$$

$$\begin{aligned} \frac{\partial C_{qp}(r, t)}{\partial t} &= D_{qp} \nabla^2 C_{qp}(r, t) - C_{qp}/\tau_r \\ &+ \frac{\varsigma \hbar \nu}{\Delta \tau_{qp}} \exp(-t/\tau_{qp}) C_e(r, t), \end{aligned} \quad (5.4)$$

with Δ the superconducting gap, $C_e(r, t)$ the probability density to find the excited electron at position r at time t after photon absorption and $C_{qp}(r, t)$ the quasiparticle density.

An estimation of the Ginzburg-Landau relaxation time results in $\tau_{gp} \ll 1$ ps. Therefore, we assume the current redistribution due to the spatial variation of the density of superconducting electrons $n_{se} - C_{qp}(r, t)$ to be instantaneous on time scales > 1 ps. To obtain a more realistic current-distribution than in [28], we now apply the relation that the velocity of superconducting electrons can be calculated from the gradient of the phase of the superconducting condensate [32]:

$$v_S = \frac{\hbar}{m} \nabla \varphi, \quad (5.5)$$

and the current density then becomes

$$j_s = -en_{se} \frac{\hbar}{m} \nabla \varphi. \quad (5.6)$$

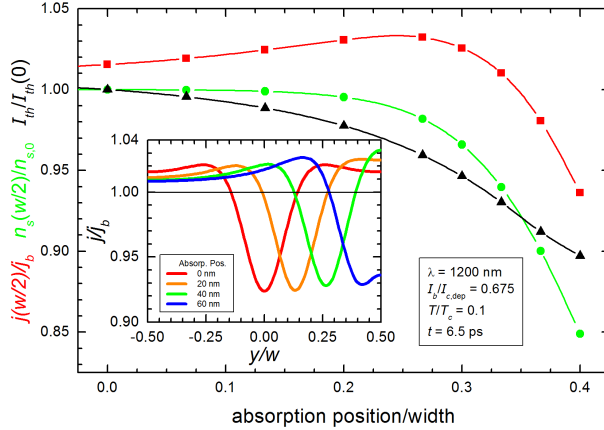


Figure 5.9: Variation of reduced current density at the edge $j(w/2)/j_b$, normalized density of superconducting electrons $n_s(w/2)/n_{s,0}$, and rescaled threshold current for photon detection as a function of the distance of the photon absorption position from the center of the wire. The variation of the threshold current near the center of the wire is dominated by the variation of the current density at the edge. For absorption events closer to the edge the reduction of the density of superconducting electrons becomes the dominating effect. In the inset we show the variation of the current density across the wire for different absorption positions.

and we have to solve the continuity equation:

$$\nabla \cdot (-en_{se}\nabla\varphi) = 0, \quad (5.7)$$

where we use the previously calculated quasiparticle distribution to obtain n_{se} . Additionally, we take into account that the density of superconducting electrons depends on the velocity v_s [97].

$$n_{se} \propto 1 - (v_s/v_c)^2/3, \quad (5.8)$$

with v_c the critical velocity at the critical-current density j_c . Thus equation 5.7 becomes nonlinear. Once we know the current distribution, the potential energy experienced by a vortex be can calculated as suggested in [29]. More details about the refined numerical model can be found in [32].

In the inset of Figure 5.9 we plot reduced current densities j/j_b across the strip for some absorption positions. At first, current densities increase with decreasing distance of the absorption position to the near edge. If the distance becomes less than 20 nm to the edge the current density near the edge is reduced, eventually below the equilibrium bias current-density j_b .

In the main graph of Figure 5.9 the reduced current density at the edge $j(w/2)/j_b$ is plotted as a function of absorption position, together with the

density of superconducting electrons at the edge $n_{s(w/2)}$ normalized to their equilibrium density $n_{s,0}$, and the threshold current scaled by the threshold current for absorption in the center $I_{th}/I_{th(0)}$. For absorption events near the center, the variation of the threshold current is mostly determined by the variation of the current density at the edge, since the density of superconducting electrons at the edge remains approximately constant. At close distances to the edge n_s is significantly reduced at the edge. This is the reason for a reduced current density at the edge, but additionally leads to a reduction of the vortex self-energy which is proportional to n_s . This second effect is stronger than the effect of the reduced current density and as a result we obtain a monotonic reduction of the threshold current for vortex entry as a function of the distance from the strip center.

We define the threshold current as that value of the bias current for which the maximum potential energy for a vortex becomes zero. In this case we expect an internal detection efficiency equal to one. With this criterion, we obtain the energy dependence of the threshold current as a function of position, which is plotted in Figure 5.10. The vortex-entry current without photon absorption is also indicated by the horizontal line. This curve is symmetric with respect to the center line of the wire due to the symmetry between vortices and antivortices in zero applied magnetic field. There is a significant reduction of the threshold current for photons absorbed near the edge of around 10% as compared to the center of the wire. We would like to point out that for each position in the wire we find a linear relation between threshold current and photon energy, consistent with previous experimental results [18] reported in Chapters 3 and 4.

As the photon energy increases and as absorption occurs closer to the edge, the relation between the density of superconducting electrons and the current distribution (equations 5.7 and 5.8) becomes more nonlinear. For absorptions very close to the edge, the nonlinear solver produces systematic errors. For all wavelengths, we do not calculate the detection current for absorption sites closer than one coherence length to the edge of the wire. For short wavelengths, the area in which this occurs increases, to approximately 12 nm from each edge at 800 nm. In our calculations, we assume that the detection current this close to the edge of the wire is weakly dependent on the absorption position and set it constant, with a value equal to the threshold current in the point closest to the edge that we can still reliably compute.

In our experiment, we are operating below this threshold current. To convert the threshold current into a local detection probability, we assume a functional dependence of the form $p(I_b) = \exp((j_{th} - j_b)/j^*)$, where $j^* = 0.9$ GA is an experimentally determined scaling current. In this way, we obtain the variation of the internal detection efficiency for a given bias current as shown in the inset of Figure 5.4

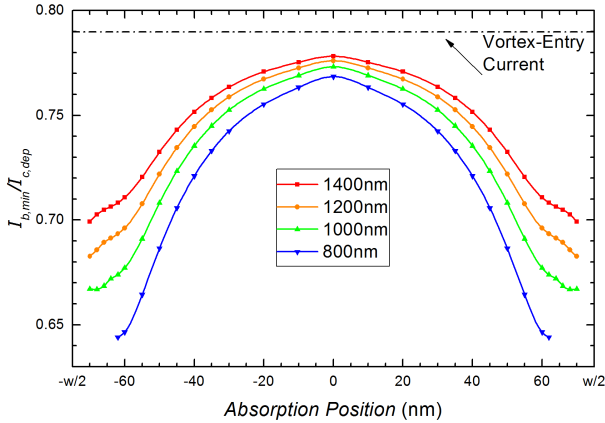


Figure 5.10: Calculated threshold current as a function of the distance of the photon absorption position from the center of the wire for different photon wavelengths. The relative reduction of the threshold current for absorption near the edge compared to absorption in the center increases with increasing photon energy for the energy range considered in this study.

5.i.4 Absorption Calculations

In this section, we demonstrate two things: first, that the absorption in the NbN wire is well approximated by considering only a 2D cross-section, i.e. that the effect from the tapers of the bridge used in our experiment is small. Second, we show that the uncertainty in the dielectric constant of our film does not strongly affect the overall absorption profiles.

We calculate the absorption of the detector for both polarizations using a finite-difference-time-domain (FDTD) programme (RSOFT Fullwave). To test whether the effect of the taper is prominent, we perform a 3D simulation at a wavelength of $\lambda = 1500$ nm, including the tapered parts and the central wire, which is 150 nm wide, 200 nm long and 5 nm thick. The results of this calculation are shown in Figure 1. The top plots of Figure 5.11 (a) and (b) are 1D absorption distributions across the wire from the center ($z = 0$ nm) to the ends of the wire, extracted from the 3D simulations. For the case of both TE and TM, the absorption distributions across the wire have roughly the same shape, irrespective of the position along the wire at which they are taken.

We compare these 3D results with a 2D simulation, in which the detector is modeled as an infinite wire. The bottom panels of Figure 5.11 (a) and (b) show the comparison of 2D (solid) and 3D (dashed) simulation, where the 3D absorption curve is the average of the absorption curves at different z positions shown in the top part of Figure 5.11. Because we are only interested in relative differences within each absorption profile, we normalized the 2D

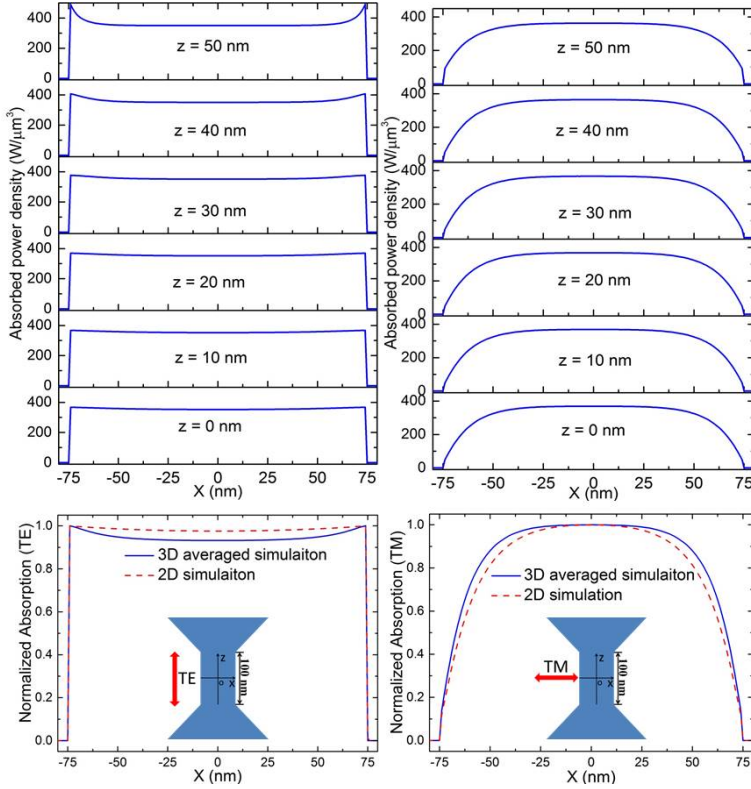


Figure 5.11: Absorption distribution in 2D and 3D, computed at a wavelength of 1500 nm for TE (left) and TM (right). In each subfigure, the top panel shows the 1D absorption density across the wire at different positions on z axis, and the bottom panel shows the averaged absorption (dashed line) of six curves on the top, as well as the result of the 2D simulation, which does not consider the tapered parts.

and the averaged 3D curves to their maximal values individually. For both the TE and TM case there is little difference between the 3D and 2D absorption profiles, which means that we are justified in using the computationally efficient 2D simulations in our main text.

The dielectric constant of NbN ϵ_{NbN} used throughout these calculations is obtained from ellipsometry measurements. If we calculate ϵ_{NbN} from these measurements, the result will depend on the assumed thickness of the film. To assess the implications of this effect, our strategy is therefore to re-calculate ϵ for different thicknesses, and observe the effect on the absorption profiles. In [96], the thickness of the film was estimated to be $4.9\text{nm} \pm 0.1\text{nm}$. We assume a more conservative error bar $\pm 0.3\text{nm}$ on the thickness, based on the thickness of a single atomic layer. Then we compute

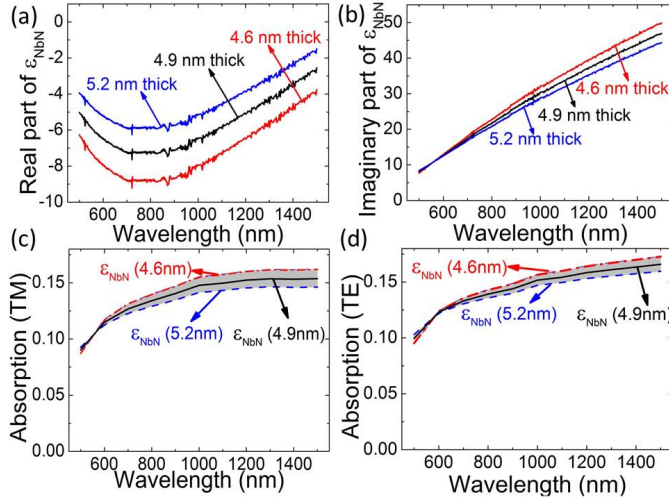


Figure 5.12: Dielectric constant of NbN obtained by considering potential errors in the thickness of the NbN film. (a) and (b) show the real and imaginary part of ϵ_{NbN} . (c) and (d) show the absorption of the 2D NbN wire with the three sets of dielectric constant of NbN, for TM and TE respectively.

the related epsilon $\epsilon_{\text{NbN}(4.6\text{ nm})}$ and $\epsilon_{\text{NbN}(5.2\text{ nm})}$ for thickness of 4.6 nm and 5.2 nm. These are shown in Figure 5.12 (a) (real part) and (b) (imaginary part). Throughout Figure 5.12, red and blue lines indicate $\epsilon_{\text{NbN}(4.6\text{ nm})}$ and $\epsilon_{\text{NbN}(5.2\text{ nm})}$ respectively. Then, we compute the absorption using these two new sets of dielectric constants. We obtain the total absorption in the NbN wire as a function of wavelength, which is shown in Figure 5.12 (c) for TE and in Fig 5.12 (d) for TM. For most wavelengths (600nm – 1500 nm), $\epsilon_{\text{NbN}(4.6\text{ nm})}$ causes higher absorption, which is due to its larger imaginary part of dielectric constant at small thickness (4.6 nm).

Variations in ϵ_{NbN} also affect the distribution of absorption across the wire. To investigate this, we calculate the position-dependent absorption with the three sets of ϵ_{NbN} for TE and TM polarization. The inset of Figure 5.13 shows these, for three representative wavelengths of 500nm (a), 1000nm (b) and 1500nm (c). We plot the ratio between TE and TM, since this is ultimately the quantity of interest. In Figure 5.13, the ratios of the TE absorption over the TM absorption for each of the three wavelengths are shown. The small variations indicate that any potential systematic error in the dielectric constant due to a different thickness of the film does not significantly influence our results in the main text.

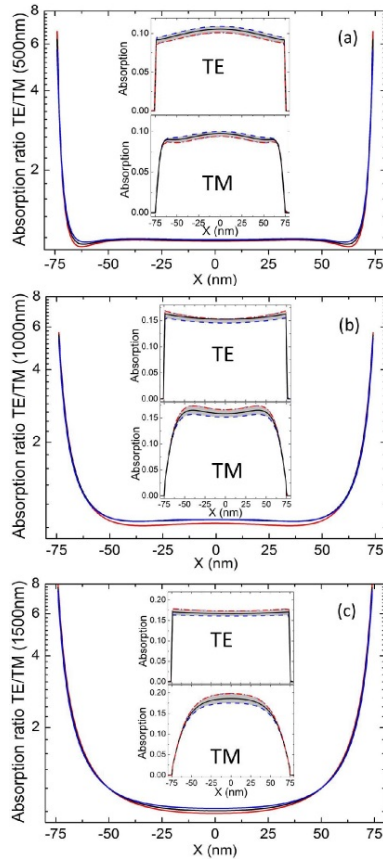


Figure 5.13: Position-dependent absorption ratio TE / TM at wavelengths of 500 nm (a), 1000 nm (b) and 1500 nm (c). In each sub-figure, three dielectric constants (red for $\epsilon_{\text{NbN}}(4.6 \text{ nm})$, black for $\epsilon_{\text{NbN}}(4.9 \text{ nm})$ and blue for $\epsilon_{\text{NbN}}(5.2 \text{ nm})$) are plotted, corresponding to three different thicknesses of the film. The insets show the absorption distributions for TE and TM illumination individually.

5.i.5 Computation of Polarization-Dependent Visibility

In this section, we outline the algorithm which we use for computing the visibility of the polarization-dependent oscillation in p_1 from a given microscopic energy-current relation $\gamma'(x)$.

- Interpolate $\gamma'(x)$ on a 1 nm grid, from the points at which it is given. We assume mirror symmetry around the point $x = 0$.
- Normalize each pair of absorption profiles $A(x)_k$, where k stands for either TE or TM, such that their integrals are the same. This is done to take out the dependence on overall absorption probability, which is not measured in p_1 .
- For each wavelength, compute $j_{th}(x) = j_0 - \gamma(x)E$. We take j_0 to be $j_{c,exp}$, in accordance with the theoretical predictions of the vortex crossing model.
- For each current, for each wavelength, compute the detection probability density $P(X) = \min\{1, \exp(j_b - j_{th})/j^*\}$, with $j^* = 0.9 \text{ GA/m}^2$.
- Compute $p_{1,k}(I, E) = \int_{-w/2}^{w/2} P(x, I, E)A(x)_k dx$.
- Compute the average value of $p_1 = (p_{1,\parallel} + p_{1,\perp})/2$
- Compute the visibility $V_{I,E} = (p_{1,\parallel} - p_{1,\perp})/(p_{1,\parallel} + p_{1,\perp})$.

In order to fit the internal threshold current profile to the experimental data, we use Tikhonov regularization [98]. That is, to the usual function that is minimized in an inversion problem

$$g(x) = \sum_i (V_i(\gamma'(x)) - V_{i,exp})^2 / \sigma_i^2, \quad (5.9)$$

where V is the observed visibility and σ is the error on each visibility, we add the extra term

$$g(x) = \sum_i (V_i(\gamma'(x)) - V_{i,exp})^2 / \sigma_i^2 + s \sum_j (\gamma'(x_j) - \gamma'(x_{j+1}))^2, \quad (5.10)$$

which has the effect of penalizing solutions where the difference between adjacent points in the curve is large. This is a standard way of regularizing (i.e. making invertible) nearly ill-posed problems. We apply only weak regularization such that the contribution to $g(x)$ from the second term is approximately 20% of the first. Furthermore, we apply the constraint that the sum $\gamma'(x)$ should be comparable to the sum of the theoretical $\gamma'(x)$ curve. We find that we can fit our data if we set $\sum_i \gamma'(x)_{exp} \Delta x_i = 1.15 \sum_i \gamma'(x)_{theo} \Delta x_i$. We varied the number of points and value of s and verified that the solution presented in the main text is robust.

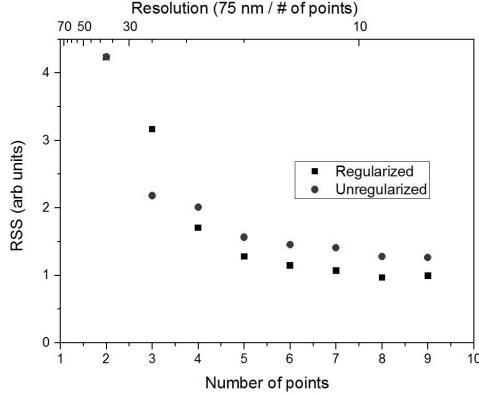


Figure 5.14: Residual sum of squares as a function of the number of points at which we define $\gamma'(x)$, i.e. the number of free parameters in our fit. We observe that beyond $\Delta x = 15$ nm, there is only a slow decrease in our goodness-of-fit parameter. This decrease stops at $\Delta x = 10$ nm. From this, we conclude that the resolution with which we can determine the local IDE is around 10 nm.

5.i.6 Resolution

In this section we will justify the resolution claimed in the main text of Chapter 5. To find the resolution with which we can reconstruct the local IDE, we perform the procedure outlined in section 5.6.5 for various spacings Δx of the points at which we specify $\gamma'(x)$. We define the resolution as that spacing beyond which adding further points does not improve the fit to our experimental data.

In Figure 5.14, we show the results of this procedure. We plot the RSS (residual sum of squares) for both the unregularized and regularized version of our fit (i.e. equations 5.9 and 5.10, respectively). We find (as expected) that the RSS of the regularized fit typically lies above that of the unregularized fit. We find that the value of the RSS decreases rapidly when increasing the number of fit parameters, dropping to 1.3 (in arbitrary units) at a value of $\Delta x = 15$ nm. At $\Delta x = 9.3$ nm, the unregularized RSS reaches a minimum of 0.96. From this, we conclude that the resolution with which we can determine the local IDE is in the range of 10 nm. In Figure 5.15, we show the corresponding fits to our experimental data, for a few representative values of Δx . It can be seen that the fits at high values of Δx do not fit the data. Around $\Delta x = 10$ nm, we achieve a good fit.

We conclude with two remarks. First, as can be seen from the top panel of Figure 5.4, the accuracy with which we can determine the values of $\gamma'(x)$ is higher at the edges of the wire than in the center. The reason for this is that

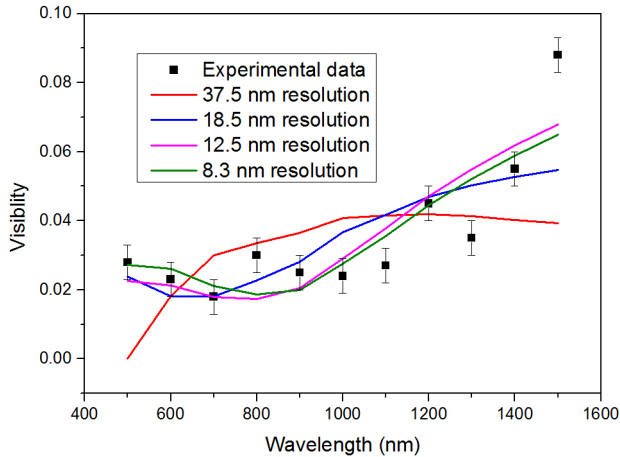


Figure 5.15: Fits of the regularized detection model to our experimental data, for various values of Δx .

the edges contribute much more to the effect of a polarization-dependent internal detection efficiency, as these parts are preferentially excited by one polarization. In the discussion above, we have largely assumed a constant spacing between points. In principle, however, the resolution could also be a function of the position along the wire. Our data is not of sufficient quality to say anything quantitative about this, but we expect that the resolution in the center would be lower than at the edges.

Second, we note that our experimental data has several outliers, which are fitted by none of the models. For a model which completely describes the data, we would be able to compute χ^2 to determine which model describes the data with the minimum number of free parameters. Unfortunately, the presence of these outliers precludes this route since we would have $\chi^2 \gg 1$.

5.i.7 Detection Probability Profiles

For completeness, we present all position-dependent quantities in our analysis combined, for three representative wavelengths. In Figures 5.16-5.18, we plot the absorption for both polarizations $A(x)$, internal detection probability $P(x)$ and the detection probability density $P(x)A(x)$ (dashed line) for 1500 nm (Figure 5.16), 1000 nm (Figure 5.17) and 500 nm (Figure 5.18). These graphs clearly illustrate why the visibility of our observed effect increases with wavelength: for short wavelengths, the difference between the two optical absorption probability densities is very small, and occurs only at the outermost 10 nm or so. In contrast, at high wavelengths the difference in

absorption probabilities is much larger, which makes the internal probability distribution more visible.

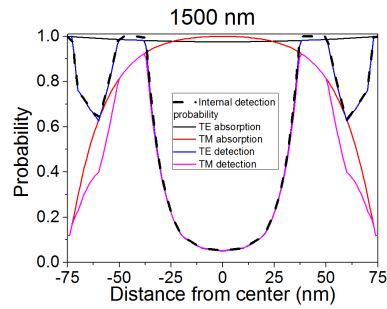


Figure 5.16: Internal detection probability, TE and TM absorption, and TE and TM detection probability, for 1500 nm illumination.

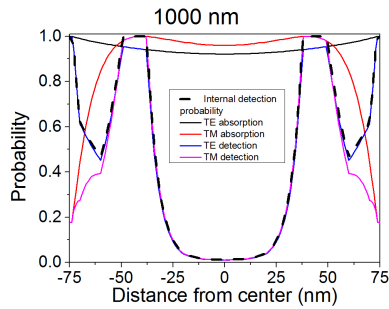


Figure 5.17: Internal detection probability, TE and TM absorption, and TE and TM detection probability, for 1000 nm illumination.

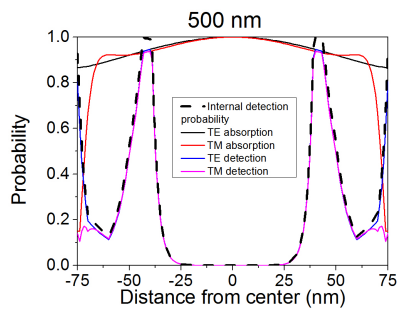


Figure 5.18: Internal detection probability, TE and TM absorption, and TE and TM detection probability, for 500 nm illumination.

5.ii Appendix: Implications of the Position Dependence of the Threshold Current of SSPDs

Nanowire superconducting single-photon detectors [1] are a crucial resource for high-efficiency, low-dark count photodetection in the infrared [3]. Such detectors are of great value for many applications, including cancer research [91], and a variety of fundamental experiments [59]. The detection mechanism of such devices is an ongoing field of study which has seen great steps in recent years [17, 24, 25, 28, 32, 33, 34, 35, 72], in part driven by the development of SSPDs made of novel materials such as MoGe [99], WSi [55], MoSi [100] and MgB₂ [101]. The current understanding is that when a photon is absorbed, a cloud of quasiparticles is formed, which diverts the current from the absorption spot. If the current is large enough, a vortex unbinds from the edge of the wire, causing a detection event.

One crucial step in the theoretical understanding was the suggestion that the threshold current of the detector, i.e. the current at which the detector becomes fully efficient, is dependent on the position along the cross-section of the wire [34, 32] where the photon is absorbed. In Chapter 5, we demonstrated a measurement of this position-dependent threshold current via a differential measurement of two absorption probability profiles induced by parallel and orthogonal polarization. This confirmed an earlier preliminary result by Anant *et al.* [10] of a position-dependent internal threshold current. Within our model, the position-dependent detection efficiency is explained by the fact that vortices enter more easily at the point where superconductivity is already weakened by the presence of quasiparticles.

We demonstrated a reconstruction of this internal threshold current with a resolution around 10 nm. This is shown in Figure 5.19, where we plot the final result from Chapter 5. We plot the position-dependent detection efficiency as established from our experiments, as well as a theoretical calculation done in the vortex crossing model.

In this Appendix, we discuss the implications of a position-dependent threshold current on other quantities which have been used to investigate the detection mechanism. We take the result in Figure 5.17 as a point of departure for our calculations. We will focus on two of them: the universal curve of the detection probability and the energy-current relation. We first review the main ingredients of our model. We then move on to discuss the implications for the two quantities mentioned above.

5.ii.1 Ingredients of the Model

Our model of detection events in superconducting single-photon detectors is inspired by previous experimental observations reported in Chapters 3 and 4 and by the numerical simulations described in [28, 32]. In these experiments, we found that the threshold current required to achieve a constant detection

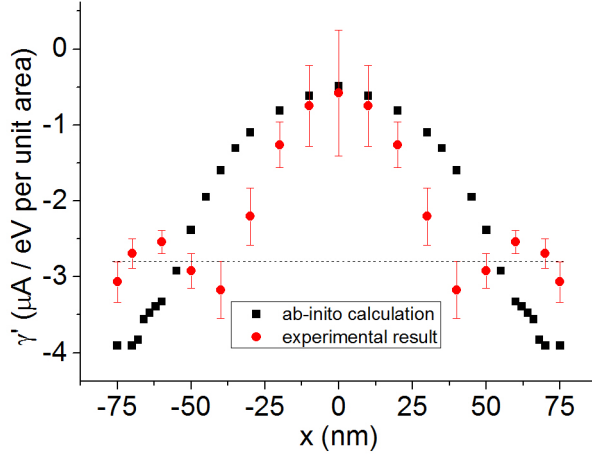


Figure 5.19: Position dependent threshold current slope in a 150 nm wide NbN SSPD. We have converted $\gamma'(x)$ to macroscopic units for easy comparison with other experimental data. The dashed line shows the threshold current which is observed for the entire wire, at low detection probabilities.

probability $I_{th} = I_0 - \gamma E$, where E is the photon energy, γ is a conversion constant - which was found to be width-dependent - and I_0 is a current scale, which was found to be $I_0 \approx 0.8I_c$ for a 1% detection probability at $T = 3.1$ K on a 220 nm wide nanodetector [17].

The numerical simulations consist of a series calculations of the threshold current as a function of photon energy and absorption position. From these calculations, we find that the linear energy-current relation extends microscopically as well, that is: $j_{th} = j_0 - \gamma'(x)E$. In this way, we introduce a position-dependent threshold current. We found in Chapter 5, however, that in order to make our calculations agree with the observed experimental data, we had to make a fit which resulted in slightly different values for $\gamma'(x)$ than were predicted by theory.

A second component of our detection model is the assumption that the detection probability decreases exponentially below the threshold current: $P(x) = \min\{1, \exp((j_b - j_{th})/j^*)\}$, where I_b is the applied bias current, j_{th} is the threshold current calculated from the local energy-current relation and j^* is a current scale that describes the detection probability below threshold. j^* is in principle an unknown quantity, but it can easily be read off from the current dependence of the detection probability at very low current. This proposed expression is justified by the notion that low-detection probability detection events are a tunneling process, similar to dark counts. Around $I_b = I_c$, the relation between bias current and energy barrier is linear [24].

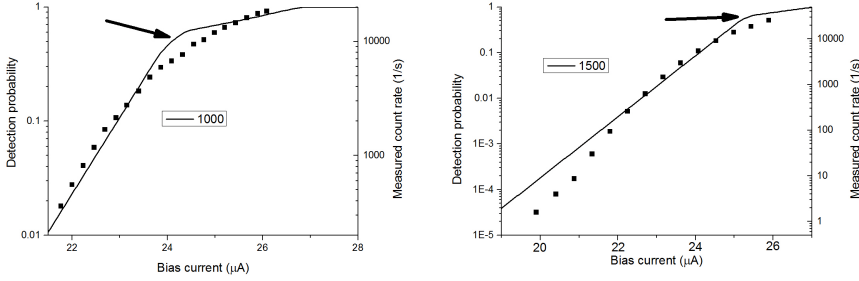


Figure 5.20: Computed versus observed detection probability as a function of bias current for 1000 nm and 1500 nm. The squares show experimental data, and the solid lines show a detection probability computed as described in the main text. The arrows indicate the point where the first sections of the wire become fully photodetecting.

This serves as justification of our proposed relation.

With these two ingredients, we can calculate the internal detection probability p_1 as a function of bias current: we first compute j_{th} for the photon energy we are interested in, then compute the local detection probability. We then compute the integral $p_1 = \int_{-w/2}^{w/2} P(x)A(x)dx$, where $A(x)$ is the absorption probability as a function of position.

We show the results of this computation in Figure 5.20 for two different wavelengths. We note that our calculated curves coincide with the experimental data to within a factor of 2 while the measured count rate changes over 2-4 orders of magnitude. Moreover, we note that the efficiency implied by these measurements ($\eta \approx 10^{-5}$) is in good agreement with the geometry of our experiment, in which a free-space beam of a few tens of μm is impinging on a 100 nm x 150 nm active area. We therefore conclude that our calculations are in reasonable agreement with our measurements.

5.ii.2 Universal Curve

In Chapter 3, the idea was put forward that there is a universal curve for photodetection in SSPDs. We observed that for photons with a wavelength between 1000 nm and 1500 nm, the detection probability as a function of bias current superimposes when they are rescaled as $p_1(I, E) = p_1(I - \gamma E)$. In this section, we will demonstrate that this is only approximately true: this relation holds only for photon states with sufficiently low energy or for sufficiently low detection probability.

Figure 5.21 shows the calculated detection probability for various wavelengths, calculated in the way described in Section 5.7.2. We clearly observe three regimes: a regime where the detection probability increases exponentially with

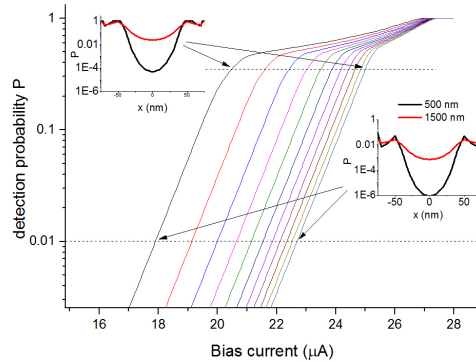


Figure 5.21: Computed detection probability as a function of bias current and photon energy, for wavelengths from 500 nm (leftmost curve) to 1500 nm (rightmost curve). *Insets:* Detection probability distribution for two wavelengths, at constant overall detection probability.

applied bias current, a regime where the detection probability increases, but much more slowly, and a regime where the detection probability is saturated at unity. These three regimes correspond to what is observed in experiments [8]. With these results, we can therefore offer an explanation of these three regimes.

In the low-detection probability regime, only the edges of the detector are photodetecting, and with low probability (see right inset of Figure 5.21). As the current is increased, gradually the edges become more efficient. Eventually, the edges of the detector saturate (see left inset of Figure 5.21) and we enter the second regime. In this regime of slowly increasing detection probability, the detection probability is increased because the area which is fully photodetecting moves inward. Eventually, the third regime is reached where the entire detector is operating with probability unity and the internal detection efficiency is constant. This result provides an explanation for the slow roll-off of the detection efficiency at low bias currents, which was previously attributed to inhomogeneities in the detector. We note that our explanation was put forward independently by Zotova and Vodolazov [34].

5.ii.3 Threshold Current

Measurements of the energy-current relation are a common way of investigating the detection mechanism [8, 16, 17, 35, 20, 73, 72]. The procedure is to take various excitation energies and bias currents and observe the iso-detection probability lines, i.e. those combinations of bias current and photon energy for which a particular predefined threshold detection probab-

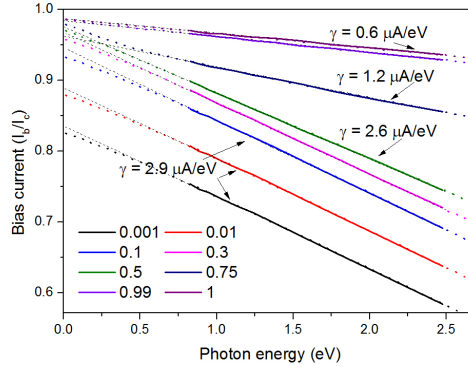


Figure 5.22: Calculated curves of constant overall detection probability for various threshold probability levels for a 150 nm wide detector. The solid lines indicate the wavelength range over which the experiment in Chapter 5 was conducted. The dashed lines indicate linear extrapolation to lower currents; the dotted lines indicate the computed threshold current at lower photon energies. The arrows and captions indicate the macroscopic values of γ found at these threshold values.

ility is achieved. Usual values are 1% to 10%. Also in use is an empirical rolloff-formula which is equivalent to a detection probability of 50% [73].

In Figure 5.22, we plot a series of computed energy-current relations. From this figure, we conclude that the energy-current relation depends on the choice of threshold criterion. However, below a threshold criterion of $p_1 = 0.3$ this dependence is very weak. This is consistent with our observations at low detection probabilities, where we observed no effect of changing the threshold criterion on the measured value of γ .

We observe that the point at which the threshold current intercepts the y-axis when extrapolated to zero energy is smaller than I_c . To compute these graphs we used a value of $I_0 = I_c$, in the threshold current formula $I_{th} = I_0 - \gamma E$, but our extrapolated values of I_0 are lower than I_c . This resolves an important discrepancy between experimental results and theory. In theoretical work, the current at which vortex crossings are possible is identified as the experimental critical current, whereas experimentally, $I_0 \approx 0.8I_{c,exp}$ was found at $T = 3.1$ K. Our computation demonstrates that both are true at the same time: the position-dependence of the detection efficiency gives rise to an effective value of I_0 that is lower than its actual value.

This effect is due to the fact that, at high photon energies, the detection probability is set almost exclusively by the single point which is most strongly photodetecting. As the photon energy is decreased, however, other parts of the wire start to participate. This means that the detection probability

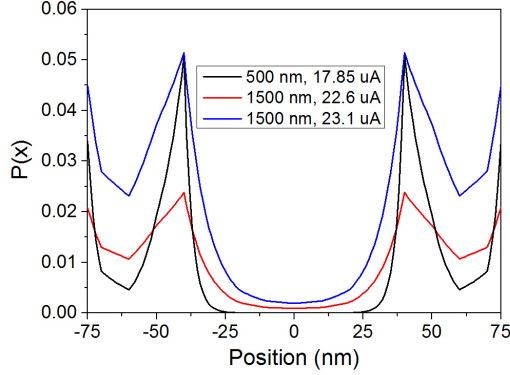


Figure 5.23: Internal detection probability for three combinations of bias currents and photon wavelengths. This figure illustrates why the overall $\gamma(x)$ measured in macroscopic experiments is smaller than the maximum value of $\gamma'(x)$. The black curve shows the detection probability profile that has an overall detection probability of 1% for light with $\lambda = 500$ nm. The red curve shows the equivalent curve for light with $\lambda = 1500$ nm. The blue curve shows the detection probability for $\lambda = 1500$ at the current at which the most strongly photodetecting point is equally efficient as in the case of 1% detection probability at 500 nm. In this last case, the overall photodetection probability is 2.2%.

in the most strongly photodetecting point in the wire actually becomes less when we go to lower photon energies and higher currents, keeping the overall detection probability constant.

Effectively, the macroscopic γ which is measured is a weighted average of the $\gamma'(x)$ curve, where obviously points with high detection probability count more strongly. This can be seen by comparing Figures 5.17 and 5.20; the value of $\gamma'(x)$ has its maximum at $\gamma'(40 \text{ nm}) = 3.2 \mu\text{A}/\text{eV}$ but the wire as a whole has $\gamma = 2.9 \mu\text{A}/\text{eV}$. This effect is illustrated in Figure 5.23, where the internal detection probability is plotted for a number of combinations of photon energy and bias current which all satisfy the 1% detection probability criterion.

The dashed lines in Figure 5.22 show computed threshold currents at very low values of excitation energy. At low values of excitation energy, the linear relation between bias current and photon energy breaks down. The detection probability at $E = 0$ has an exponential dependence on the threshold current $R(I, E = 0) \propto \exp(I_b - I_c)$. It is tempting to think that in this way, we have naturally accounted for dark counts in our model. However, experimentally we find that the extrapolated values of our linear energy-current relation are

far away from the currents at which we observe any dark counts¹⁵. E.g. for the device presented in Chapter 4, we find $I_0 = 33.8 \mu\text{A}$, for a threshold value of $p_1 = 0.01$, whereas we don't observe any dark counts until we approach the critical current $I_c = 44 \mu\text{A}$. We therefore conclude that this effect represents at best a partial solution of the dark count problem: the assumption that dark counts can be understood as photon counts at energy $E = 0$ is a natural feature of the kind of model which we present here, but is in disagreement with experimental data.

¹⁵See Chapters 3 & 4.

Chapter 6

The Effect of Magnetic Field on the Intrinsic Detection Efficiency of Superconducting Single-Photon Detectors

We experimentally investigate the effect of a magnetic field on photon detection in superconducting single-photon detectors. At low fields, the effect of a magnetic field is through the direct modification of the quasiparticle density of states of the superconductor, and magnetic field and bias current are interchangeable, as is expected for homogeneous dirty-limit superconductors. At the field where a first vortex enters the detector, the effect of the magnetic field is reduced, up until the point where the critical current of the detector starts to be determined by flux flow. From this field on, increasing the magnetic field does not alter the detection of photons anymore, whereas it does still change the rate of dark counts. This result points at an intrinsic difference in dark and photon counts, and also shows that no enhancement of the intrinsic detection efficiency of a straight SSPD wire is achievable in a magnetic field¹.

¹This chapter has been submitted to Appl. Phys. Lett.

6.1 Introduction

Nanowire superconducting single-photon detectors [1] are a crucial technology for single-photon detection in the infrared, since they can achieve detection efficiencies of up to 93% [55], with low dark count rate, low jitter, and short reset time [3]. These detectors consist of a narrow and thin wire of superconducting material, carrying a bias current.

While the broad outlines of the photodetection mechanism are known, there is as yet no complete theory describing the response of such detectors. The present understanding of photodetection in SSPDs is as follows [17, 24, 25, 28, 34, 35, 70, 72, 102]: when a photon is absorbed, a cloud of quasiparticles is created which locally reduces the current-carrying capacity of the wire. Current is expelled from the absorption spot. If this diverted current is sufficiently strong, which depends on both the initial bias current and the energy of the photon, the Lorentz force may cause the unbinding of a vortex from the edge of the wire, leading to a measurable voltage pulse. Therefore, experiments on SSPDs in a magnetic field are a natural way of investigating the detection mechanism; one might even wonder whether the efficiency of the detector could be enhanced by applying a magnetic field.

In this chapter, we study how an applied magnetic field directly affects the microscopic detection mechanism in a short section of wire. By using a single narrow active area in a bridge-like configuration, we avoid the question of current flow around curved sections of the device, which complicated the interpretation of previous experiments [81, 103]. We find that it is the direct modification of the quasiparticle density of states in the superconductor that governs the magnetic field behaviour of SSPDs. In dirty-limit superconductors (such as thin-film NbN), this density of states is modified by a bias current or a magnetic field [104]. The effect of a magnetic field is therefore a homogeneous weakening of Cooper pairing, resulting in a higher detection efficiency at constant bias current. We identify three regimes. In the low-field regime (up to ~ 50 mT) the current flow is sufficiently homogeneous. Bias current and magnetic field are completely interchangeable, as described by the Usadel equations [105]. The relevant parameters of this theory do not depend on the illumination wavelength or on temperature in our measurement range, as is expected. In the intermediate regime (50 mT - 200 mT) we still observe photon counts, but a higher current is required to achieve photodetection than predicted by the homogeneous theory. In the high-field regime (200 mT), first light and then dark counts are gradually extinguished when the field is increased. We attribute this to the presence of vortices in the wire.

We find that the enhancement of light and dark counts on a single active spot obey different field scales, pointing to a fundamental difference in the nature of the two. The field scale for the reduction of the critical current is smaller than the scale for the increase of the count rate. This leads us to conclude that no intrinsic enhancement of the detection efficiency of an

SSPD under the influence of a magnetic field is possible.

6.2 Experiment

Our experiments were performed on two different detectors: a 200 nm long bridge with a width of 150 nm (sample A), and a bow-tie shaped nanodetector [39] with a width of 220 nm (sample B). The detectors were fabricated on 5 nm thick NbN films, that were sputter-deposited on a GaAs substrate. The detectors were patterned using conventional e-beam lithography and reactive-ion etching in a SF₆/ Ar plasma [47]. After patterning, detectors had a critical temperature of 9.5 K, and a sheet resistance of $R_{\square} = 600 \Omega$.

The samples were mounted in a Physical Properties Measurement System (PPMS) in a custom insert that allows optical coupling and high-frequency electronic readout². We bias our device through a 100 Ω resistor, and measure the current and voltage over the device. We determine the critical current with a 10 Ω resistance criterion. The noise from the room-temperature broadband amplifiers in our measurement circuit reduces the critical current of our devices by approximately 1 μ A. To facilitate comparison between critical-current measurements and count rate measurements, all measurements presented here were performed with these amplifiers present in the circuit.

The orientation of the applied magnetic field was perpendicular to the film. In order to avoid hysteresis, all measurements were performed while increasing the magnetic field. After a measurement run, the field was further increased to 1 T, before ramping it down using the demagnetizing (degaussing) option of the PPMS control software, which was found to be crucial for obtaining reproducible results. The remanent field was estimated to be 1 mT, which is consistent with specifications [106].

We illuminate our detectors with a continuous-wave laser with a wavelength of 826 nm, and an optical power of 12 mW. The illumination spot is approximately 2 mm in diameter. We have no control over the polarization, but it was kept constant during the experiment. We recorded the count rate during a 1 s interval at each current.

6.3 Results

In Figure 6.1, we plot a typical experimental result. The magnetic field was increased from 0 mT to 300 mT in steps of 30 mT. We observe an exponential increase of the count rate with bias current, followed by saturation at higher currents and a final exponential increase associated with dark counts, as is usually observed for this kind of detector [89]. The presence of a magnetic

²We verified that the temperature of this custom insert was identical to the temperature measured on the block thermometer of the PPMS.

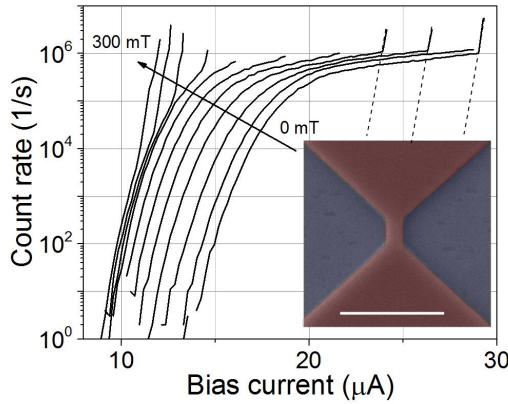


Figure 6.1: Count rate of sample A, illuminated with 826 nm light at $T = 1.8$ K, for different magnetic fields ranging from 0 mT to 300 mT, in steps of 30 mT. This measurement was not corrected for dark counts. The dashed lines are a guide to the eye indicating the part of the curve where dark counts are dominant. *Inset*: False-colour SEM image of a detector (NbN coloured red) nominally identical to sample A. The scale bar is $1 \mu\text{m}$.

field shifts the curve towards lower currents³. We note that as the field is increased, a larger part of the count rate curve is dominated by dark counts. We conclude that photon counts and dark counts obey different field scales, even in our geometry where there is a single active area.

We have compared our results to the theory of Bulaevskii *et al.*[24, 25], which considers the effect of a magnetic field on the entry barrier of vortices. This theory predicts an exponential increase of count rate as a function of applied field, at constant bias current. As in previous experiments [26, 103], we find that the prediction which this theory gives for the rate of exponential increase is an order of magnitude away from the experimental value.

In Figure 6.2, we plot those combinations of bias current and magnetic field which are required to achieve a constant count rate, from $1/\text{s}$ to $10^5/\text{s}$. For low magnetic fields $B \lesssim 50$ mT, the resulting iso-count rate curves lie on a series of concentric ellipses, which we have plotted in Figure 6.2. For sample B, we similarly find concentric ellipses (not shown). In the measurement regime reported here, the dark count rate is negligible ($\ll 1/\text{s}$).

In Figure 6.3, we turn to the temperature dependence of the magnetic-field response. We find that changing the temperature induces an overall shift in the iso-count-rate curves, but that I_Γ and B_Γ are independent of temperature. We have also verified that these parameters are independent

³From the fact that the curves have the typical shape for 1-photon detection and from the low count rate, we infer that multiphoton detection events do not play a role.

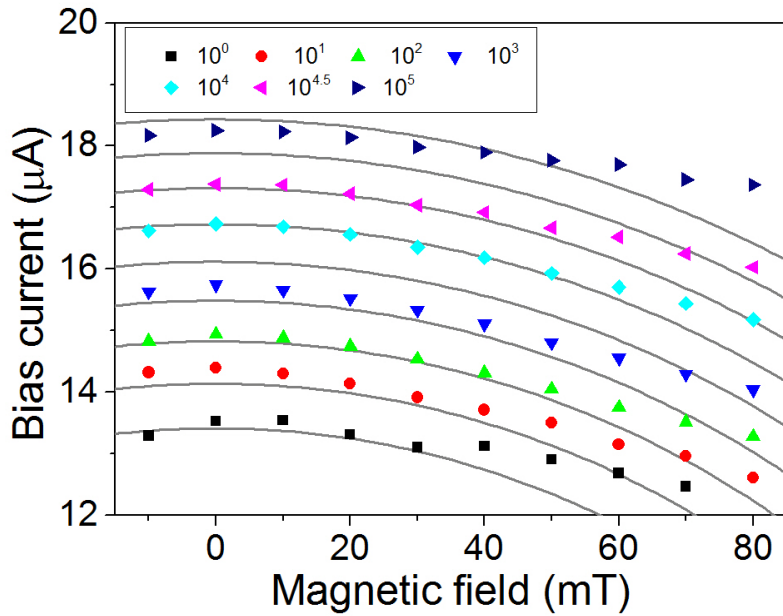


Figure 6.2: Bias current at constant count rate as a function of magnetic field for sample A. The different colours and symbols correspond to different count rates, over five orders of magnitude. We find that for low magnetic fields (up to ~ 50 mT) the required current to achieve a certain number of counts depends quadratically on applied magnetic field. The grey lines are equidistant ellipses calculated using the Usadel formalism (see text).

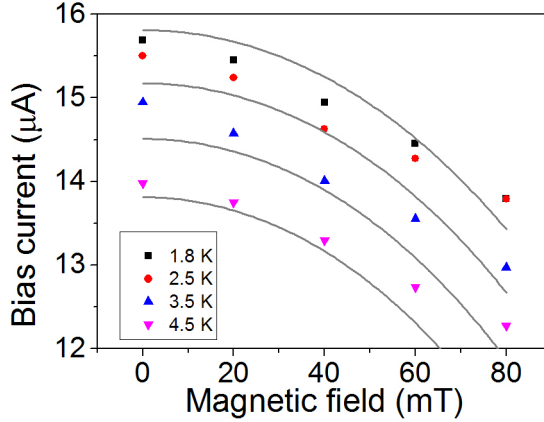


Figure 6.3: Magnetic field dependence of the count rate at different temperatures for sample A. We plot the count rate required to obtain 1000 counts / s at different temperatures. We find that I_{Γ} and B_{Γ} are independent of temperature.

of illumination wavelength by repeating the experiment with light of 405 nm and 1300 nm (not shown). The shift in count rate as a function of temperature at zero field is consistent with our previous results presented in Chapter 4, where we showed that the temperature dependence of the SSPD response is determined by the energy barrier for vortex entry.

6.4 Comparison to Theory

We analyze these observations in terms of the microscopic theory for dirty-limit superconductivity, motivated by our analysis of the modification of the electronic state due to intrinsic pair breaking in similar films [107]. For our film, $\lambda_{\perp} \gg w, d$, with λ_{\perp} the effective penetration length, and w and d the width and thickness of the wire, respectively. Therefore, we assume a homogeneous current flow through our wire. In this case, the superconducting state is described by the homogeneous Usadel equation [105]:

$$iE \sin \theta + \Delta \cos \theta - \Gamma \sin \theta \cos \theta = 0, \quad (6.1)$$

where E is the quasiparticle energy, θ is the pairing angle, Δ the superconducting pairing potential and Γ the pair breaking energy, representing a finite momentum of the Cooper pairs. A bias current I_b and a perpendicular magnetic field have a similar effect in weakening the superconducting state, as was shown experimentally by Anthore *et al.* for one-dimensional aluminium wires [104]. In this case, the depairing energy can be approximated

by:

$$\frac{\Gamma}{\Delta} = \left(\frac{\Delta}{U(\Gamma)} \frac{I_b}{I_\Gamma} \right)^2 + \left(\frac{B}{B_\Gamma} \right)^2, \quad (6.2)$$

$$\frac{U(\Gamma)}{\Delta} \approx \frac{\pi}{2} - 1.8 \frac{\Gamma}{\Delta} - \left(\frac{\Gamma}{\Delta} \right)^2, \quad (6.3)$$

where $I_\Gamma = \sqrt{2}\Delta/eR(\xi)$ and $B_\Gamma = \sqrt{6}(\hbar/ew\xi)$ are characteristic current and field scales, respectively, with $R(\xi)$ the resistance of a section of the wire one coherence length ξ long.

We note that the structure of these equations is compatible with our experimental observations at low fields: they define a series of concentric ellipses in the $I - B$ plane, connecting points with equal value of Γ/Δ . For a more quantitative analysis of I_Γ and B_Γ , we have determined the coherence length $\xi = 3.9$ nm from the slope of the upper critical field at the critical temperature. To evaluate $R(\xi) = 7.2 \Omega$, we have assumed a homogeneous sheet resistance of our NbN film. We have determined the value of $\Delta = 1.9$ meV at $T = 1.5$ K using scanning tunnelling spectroscopy on a piece of the same film that was used to fabricate the detectors. In the STM tunneling spectra, we observe slightly rounded-off coherence peaks, consistent with the presence of an intrinsic pair breaker $\Gamma \approx 100 \mu\text{eV}$, as was found previously on NbTiN and TiN films with similar resistivity [107, 108]. The presence of this pair breaker does not change the analysis that we present here. Using these values, we estimate $I_\Gamma = 180 \pm 20 \mu\text{A}$, $B_\Gamma = 2.7$ T for sample A, and $I_\Gamma = 330 \pm 20 \mu\text{A}$, $B_\Gamma = 1.8$ T for sample B. These values were used in generating the ellipses in Figure 6.2; the only remaining freedom is the dependence between the count rate C and the normalized pair breaking energy $C(\Gamma/\Delta)$.

From the excellent agreement between theory and experiment at magnetic field values $B \lesssim 50$ mT, we conclude that in this regime the count rate of the detector is determined only by a homogeneous weakening of the superconducting state, that can be described by the depairing energy Γ . This implies that the only way in which the magnetic field affects the detection mechanism is through the electronic state of the superconducting film before a photon is absorbed. This picture is reinforced by the fact that the effects of magnetic field and temperature are independent: the field response is set by the film, whereas the temperature response is set by the barrier for a vortex entering the wire when a detection event occurs.

6.5 High-Field Effects

In Figure 6.4, we plot the field dependence of a representative count rate (1000/s) and the field dependence of the critical current for a wider range of magnetic fields. We phenomenologically distinguish three regimes, independent of the chosen count rate. In the first regime, up to $B \lesssim 50$ mT, our

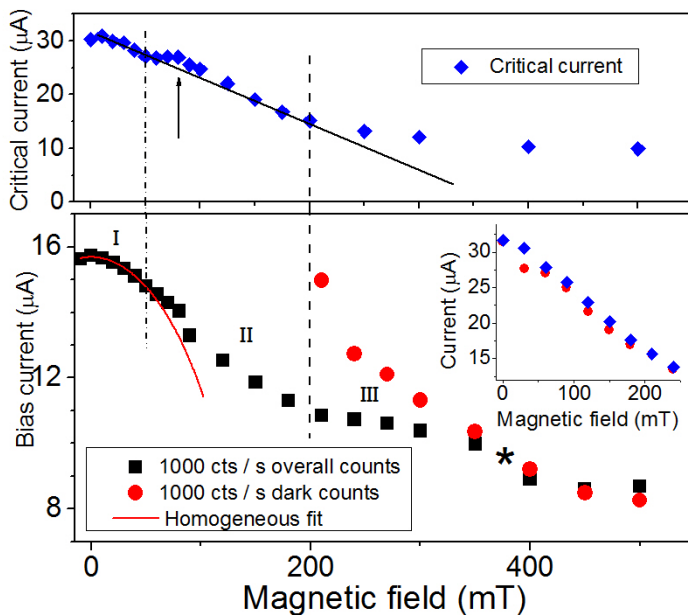


Figure 6.4: Critical current (*top*) and curve of constant count rate (*bottom*) as a function of magnetic field for sample A. The black squares indicate count rate under illumination (photon counts + dark counts), the red circles indicate dark counts and the blue diamonds indicate critical current. The asterisk marks the point where all observed counts are dark counts. The solid line in the top panel is a guide to the eye. The red curve is a plot of equation 6.2 for this count rate. We identify three regimes (see text), demarcated by the two vertical lines. *Inset:* Critical current and 1000/s dark count rate at low fields.

data follows the prediction from the homogeneous theory. In the second regime ($50 \text{ mT} < B < 200 \text{ mT}$), more current is required to produce detection events with a given probability than predicted by the homogeneous theory. In the third regime ($B > 200 \text{ mT}$), the count rate is almost independent of the applied field. However, the critical current continues to decrease and we observe throughout our measurement range that the dark counts shift with the critical current (see inset Figure 6.3). Eventually, there is a count-rate dependent point where the observed count rate is entirely comprised of dark counts, indicated in Figure 6.4. with an asterisk. At a magnetic field of approximately 1 T, no detection events are observed any more in a 1s interval.

To understand the physical meaning of the three regimes, we turn to the critical current measurements, shown in the top panel of Figure 6.4. We observe linear decay of the form $I_c(B) = I_c(0)(1 - B/B_0)$, with $B_0 = 375 \text{ mT}$, up to the point $I_c(B) = 0.5I_c(0)$. At higher fields, we obtain a power-law behavior $I_c \propto B^\alpha$, with $\alpha \approx -0.4$. In this regime we observe that there is no sharp transition to the normal state. We interpret these results in the context of the extensive literature on the field dependence of the critical current of superconducting strips, where the transition from linear to power-law behaviour is interpreted as the transition from a regime of critical current set by induced depairing to a regime where the critical current is set by flux flow [22, 109, 84, 110]. The transition from induced depairing to flux flow corresponds to the transition of regime II to regime III in Figure 6.4.

One important difference from previous results is the additional feature indicated by an arrow in the critical current measurements around 80 mT, where the critical current is enhanced relative to the linear dependence. We interpret this feature as a single vortex which is pinned in our material. All our measurements were done in a geometry that is intrinsically photodetecting, and a photodetection event entails a transition of the wire to the normal state and Joule heating. Therefore, in-field cooling occurs each time there is a detection event. At 90 mT, we meet the criterion [111] for entry of the first vortex $B \approx \Phi_0/w^2$. We conclude that while there is still an edge barrier at $B = 80 \text{ mT}$, so that vortices cannot enter, apparently the pinning is strong enough that a vortex which is already there is not expelled. We note that II'in *et al.* [112] have seen comparable enhancements of the critical current that were due to vortices, albeit in the flux-flow regime.

From this, we infer the following explanation of our results: in regime I, the current flow is sufficiently homogeneous that the response can be explained by a homogeneous degradation of the superconducting state, described by the homogeneous Usadel equation. At the beginning of regime II, a vortex enters the detector and is pinned in the material. This destroys the homogeneity. From the fact that the current which is required to obtain a detection event is higher than expected from theory, we infer that the presence of a vortex is detrimental to the detection process.

A full theory of regimes II and III is beyond the scope of the present work.

It would have to take into account the direct effect of the magnetic field on the vortex barrier, the current distribution in our sample in the presence of vortices, and the associated local changes in Δ . Any full microscopic theory of photodetection in SSPDs, even at zero magnetic field, would also need to take into account the intrinsic inhomogeneity that has been observed in similar films [113, 114], and the observed intrinsic pair breaker, as it has been shown recently that these can give rise to an unexpected response to electromagnetic radiation [115].

6.6 Conclusion and Discussion

We have demonstrated that for low fields, the response of an SSPD to an applied magnetic field is set entirely by the effect that the field has on the electronic state of the material. In this regime, there is an interchange between the bias current and the applied magnetic field, in agreement with the homogeneous theory for dirty-limit superconductivity. Since the material parameters that enter this theory (λ_{\perp}, ρ) are similar for all SSPDs found in literature, our results are not limited to NbN detectors. WSi, for example has $\rho = 200 \mu\Omega\text{cm}$ and $\lambda = 1400 \text{ nm}$ [55, 32]. For the intermediate and high-field regimes, geometry and flux pinning properties become more relevant. Therefore a more diverse behaviour might be expected.

Our experiment proves that the difference between light and dark counts in a magnetic field is not due to them originating from different points in the wire, as has been put forward by others [26, 42, 116]. We conclude that there is a difference in the nature of light and dark counts in SSPDs: photon counts scale with a field scale B_{Γ} inherent to the material, whereas dark counts scale with the change in critical current under the influence of magnetic field, which depends on geometry. This difference between light and dark counts is as of yet unexplained and carries implications for the design of SSPDs: it means that the only way in which an SSPD can be made more efficient by an applied magnetic field is by choosing a geometry where the critical current is not adversely affected by the applied field, such as a spiral [117]. For a straight wire, we conclude that no enhancement of the detection efficiency can be achieved by applying a magnetic field.

Chapter 7

The Size of a Hotspot in Superconducting Single-Photon Detectors

We report on a preliminary set of data on a two-photon experiment to measure the size of an excitation area inside a superconducting nanowire single-photon detector. We find a size of the interaction area (i.e. 'hotspot size') of 22 ± 2 nm, which increases strongly at lower applied bias current. We find that this size is constant with photon energy. We find that in our tapered samples, detection events also occur up to approximately 70 nm away from the narrowest part of our wires.

7.1 Introduction

Superconducting single-photon detectors [1] are a crucial technology for a variety of applications [89]. One such application is multiphoton detection. In particular, superconducting bridges (called nanodetectors in this context) can be used for multiphoton subwavelength imaging [39], near-field multiphoton detection [118], and the measurement of ultrasensitive higher order autocorrelations [40], when biased with a critical current which is lower than the one used for single-photon detection. Simultaneous detection of up to six photons has been reported in the literature [40, 17].

The current model of photodetection in such detectors is as follows (see Chapters 1 and 4) [17, 28, 32, 72]: after the absorption of a photon, a cloud of quasiparticles is created. This cloud diffuses, spreading over some area of the wire. The redistribution of current towards the edges of the wire may cause a vortex to unbind from the edge of the wire, if the applied bias current

is sufficient. This causes a normal-state region to appear in the wire, which grows under the influence of Joule heating from the bias current, leading to a measureable voltage pulse and a detection event [9].

One of the earliest questions raised about the working mechanism of SSPDs was the size of the excitation made by the impinging photon, known as a hotspot. This question has particular relevance for multiphoton detection: if two photons are not absorbed sufficiently close to each other, no joint photodetection event will occur [44]. Therefore, the question of the hotspot size is crucial for interpreting multiphoton experiments, and for designing detectors that have optimal multiphoton detection properties.

In earlier work, attempts were made to determine the size of this hotspot by looking at the energy-current relation. Since the normal-core hotspot model (which was in use at the time) is essentially a geometric model, attempts were made to determine the size of the hotspot, by measuring the amount of current required to produce a detection event [66, 76, 119, 120]. This way of reasoning is in clear disagreement with the role of diffusion in the current models of the detection event, since the diffusion equation is linear in the initial excitation, i.e. one would expect the hotspot size to be independent of energy, whereas in the normal-core model this size increases as the square root of the energy. Moreover, the inferred size of the hotspot depends crucially on the assumed efficiency with which the energy of the initial photon is converted into quasiparticles.

In this chapter, we report preliminary work on determining the hotspot size¹ from a direct model-free measurement. Our strategy is to compare the efficiency of a detector in the one- and two photon regime. By comparing these efficiencies, we can find the distance which two photons have to be apart in order to produce a detection event. Reasoning classically, our technique relies on the fact that the first photon may be absorbed anywhere in the wire, whereas the second photon must be absorbed within some distance $s_{h,s}$ from the first. The hotspot size can therefore be extracted by comparing the efficiency in the one and two-photon regime.

We find a hotspot size which depends on the applied bias current. In the limit of high detection probability, we find that the size $s_{h,s}$ becomes constant at 22 ± 2 nm. We perform this experiment for four NbN detectors of 0, 100, 200 and 400 nm in length. At lower currents, this size increases, reaching a value of 200 nm for our two longest detectors. From this measurement we are able to infer which part of our wire is photodetecting. We find that the effective size of our detectors is 74 nm larger than their nominal size. We attribute this to photodetection events in the tapers of the

¹We retain the terminology 'hotspot size' for consistency with previous work, even though this only has a meaning in the normal-state hotspot model, where the edges of the hotspot are sharply defined. We define the quantity which we are aiming to measure as the maximal distance with which two photons can be absorbed and still *jointly* (i.e. with a probability greater than they would have individually under the same circumstances) cause a detection event.

wire. This observation matches with previous results on the photodetecting area of zero-length bridges. We interpret these observations in terms of the diffusion-based vortex model. We discuss the implications of our results on the engineering of SSPDs as well as on their application as multiphoton detectors.

7.2 Experimental Setup

The detectors used in this experiment were patterned from a single film (5 nm NbN on GaAs) to ensure that the properties of the wires were as similar as possible. The film is deposited under an ambient temperature of 400 C, which was found to give the optimal critical current for NbN on GaAs. Under these conditions, the critical temperature of the film was 9.6 K, as opposed to 11 K for detectors grown at 440 C. The detectors were patterned using conventional e-beam lithography and reactive-ion etching in an SF₆ / Ar plasma. We fabricated detectors with lengths of 0, 100, 200 and 400 nm. For each length, we fabricated 16 nominally identical detectors, with a width of 150 nm.

In this experiment, we use a series of detectors which must differ only in the wire length. To find a group of similar detectors, we measured the critical current of these detectors in a probe station. One detector of each length was selected for further investigation for having similar critical current, between 27.4 and 27.9 μ A. These detectors were located closely together on the sample, pointing to slowly varying properties within our film. After measurement of the critical current, we measured the quantum efficiency of these samples and found this to be of the order of 10^{-4} , which is the expected value taking into account the limited overlap between our illumination spot and the active area of the detector. Moreover, from the high and constant critical current, which is comparable to earlier samples² [39], and extensive inspection of detectors fabricated in the same process by SEM [121], we have minimized the possibility that these detectors are suffering from fabrication errors.

To characterize these detectors, we perform quantum detector tomography. We apply the usual technique of two crossed polarizers with a $\lambda/2$ wave plate in between to create variable attenuation of the incident light pulses with a dynamic range of more than 3 orders of magnitude. The axis of the second polarizer was set in such a way that the count rate on the devices was maximal, which corresponds to the TE polarization. This has the added advantage of producing the most uniform excitation probability density across the wire. We use a Coherent Vitesse laser ($\lambda = 800$ nm) to perform detector tomography. This laser is well suited for this experiment because it has a pulse duration of approximately 100 fs. Since the lifetime of an excitation in an SSPD is a few tens of ps [40], in this way we avoid

²See Chapters 2-4.

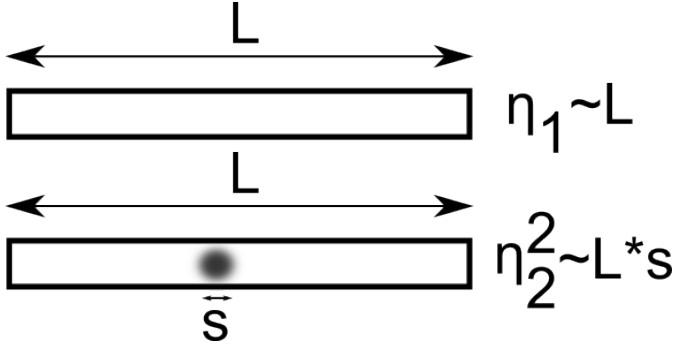


Figure 7.1: Relevant length scales in our experiment. The rectangle represents the detector, with an overall length L . The dot represents the quasi-particle excitation produced by the absorbed photon ('hotspot'), which has a length s .

introducing the temporal response of the device into the problem: our pulse duration is sufficiently short to act as a delta-like excitation compared to all relevant timescales.

7.3 Theory

In this section, we derive the expressions that we use to interpret our experimental data. For the two-photon efficiency, we compute the efficiency per photon, i.e. $\eta_{single} = \sqrt{\eta_{overall}}$, where $\eta_{overall}$ is the overall efficiency of the multiphoton process. The efficiency per photon η_{single} is the quantity that is reported by our tomography protocol.

The geometry of our experiment and the length scales involved are shown in Figure 7.1. We show two cases: first, the absorption of a single photon, which can occur anywhere in the wire, and second, the absorption of two photons. We adopt a classical picture in which we may consider the photons as arriving sequentially. We need not consider photon bunching because the probability of two photons being absorbed by the same electron is minuscule, given that there are approximately 10^7 charge carriers in a 5 nm thick NbN film 200 by 150 nm in size [122]. For a one-photon event, the overall linear efficiency of the device is just proportional to the length of the device

$$\eta_1 \propto L. \quad (7.1)$$

For a two-photon event, the two photons must be absorbed within some distance s from each other, which represents the effective interaction distance between the photons which is the quantity of interest. The first photon can be absorbed anywhere in the wire, as in the single-photon case, but the

second photon effectively sees a smaller detector, of only length s . The overall efficiency for this process is therefore:

$$\eta_2^2 \propto Ls. \quad (7.2)$$

A comparison of the one and two-photon cases yields the hotspot size.

$$s = (\eta_2/\eta_1)^2 L, \quad (7.3)$$

which contains only measurable parameters on the right hand side of the equation.

This derivation contains two crucial assumptions: first, that the absorption probability across the detector is uniform. If this were not the case, we would have to consider each position individually. We satisfy this assumption by illuminating our detector with a light spot $w_{spot} \approx 0.2$ mm, which is much larger than the device itself, which has $L = 400$ nm and $w = 150$ nm for the largest device in this study.

The second assumption is that the influence of the hotspot extends across the width of the wire. In our model, two photons absorbed at the same position along the wire, but in different positions along the cross-section are counted as having $s_{hs} = 0$, i.e. we only count the distance along the wire. The motivation for this is that it is known that the influence of the hotspot in the form of redistributed current extends across the width of the wire. This justifies our assumption.

7.4 Results

Figure 7.2 shows the experimental results, for our 100 nm long sample. Quantum detector tomography enables us to separately determine both the absorption efficiency η and the internal detection probability for a given number of n photons p_n . This is done by using the count rate measurement at high intensity as a reference, assuming $p_n = 1$ for $n > n_{max}$, where n_{max} is some photon threshold, which can be determined via model selection. By performing quantum detector tomography (QDT), we find a regime where the detector primarily responds to single photons and a regime where the detector primarily responds to two-photon events. These regimes are demarcated by the high values of the detection probability p_1 and p_2 , from $I_b = 20 - 24 \mu\text{A}$ and $I_b = 16 - 20 \mu\text{A}$, respectively. We also find the efficiency in the one and two-photon regime. These results are consistent with results reported in Chapters 2-4.

We wish to compare linear efficiencies at currents at which the nonlinear internal detection probability of the wire is the same, using the nonlinear coefficient as a measure of the location of the one- and two-photon regimes. We measure the distance between the one- and two-photon regime and observe that this value is independent of the chosen threshold criterion, i.e.

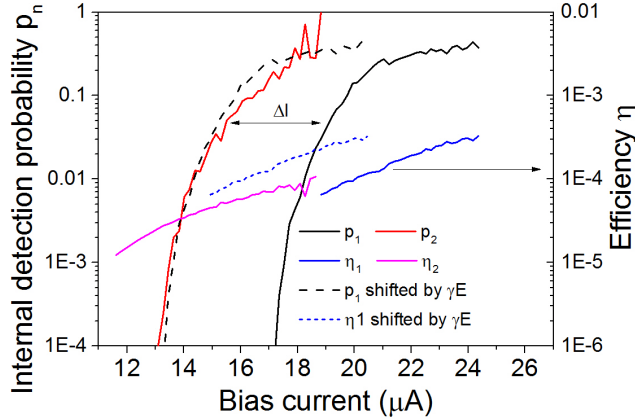


Figure 7.2: Experimental result of quantum tomography on a superconducting wire of 100 nm length. We find the efficiency as reported by our tomographic protocol in the one- and two-photon regime, as well as the coefficients p_1 and p_2 describing the internal nonlinear detection probabilities [67]. To compare the efficiency of the two photon regimes, we shift the efficiency curves by $\Delta I = \gamma E$ such that p_1 and p_2 overlap. This process is indicated by the arrow; the dotted lines show the shifted η and p_1 .

that a simple shift in current serves to describe the difference between the one- and two-photon regime. This observation is consistent with the results presented in Chapter 2. We then apply this shift, such that the one- and two-photon regimes line up (dotted lines in Figure 7.2). Note the excellent agreement between p_2 and p_1 over more than three orders of magnitude.

Finally, to obtain the size of the hotspot, we divide the efficiency $\eta(I)$ by its shifted equivalent $\eta(I + \Delta I)$, obtaining the ratio η_2/η_1 of detection probabilities from equation 7.3. For each detector, we find that for detection probabilities in the range of $p_1 = 0.1 - 1$, the ratio is independent of the precise detection probability. We take this value as characteristic for that length of the detector. We then repeat this process for all four detectors.

Figure 7.3 shows the result of this procedure, for our four detectors of different lengths. We find qualitatively that the ratio η_2/η_1 decreases when increasing the length of the wire, as is expected from equation 7.3. We find, however, that the fit of equation 7.3 to our experimental data is poor: it overestimates the ratio η_2/η_1 for the 100 nm device. Moreover, it is completely unable to account for the finite value of η_2/η_1 for our zero-length detector. The observation that this detector has a finite probability for two-photon detection forces us to consider the tapers which lead to the device. These tapers are fabricated under a 45 degree angle and serve to lead the current into the active part of the wire without introducing too much current

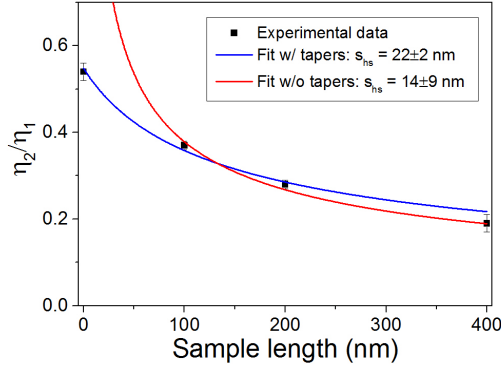


Figure 7.3: Result of the measurement of the hotspot size on a series of NbN detectors. The four data points are obtained by repeating the procedure outlined in Figure 7.2. The red line shows a fit of equation 7.3 to the experimental data, using the nominal length of the devices. The blue line shows a fit to the data taking into account an unknown extra length of the device, which represents the tapers leading to the narrow section of the bridge. For this fit, which has $\chi^2 = 3.6$, we find $s = 22 \pm 2$ nm and $l_{taper} = 74 \pm 12$ nm.

crowding.

To take into account the effect of the tapers, we replace the nominal value of L in equation 7.3 by $L + l_{taper}$, where l_{taper} is some characteristic length over which the leads of our system are also photodetecting, at the bias currents and detection probabilities which we are considering here. With this additional assumption, we are able to fit our data reasonably well ($\chi^2 = 3.6$). We find a value of $s_{hs} = 22 \pm 2$ nm, and a value of $l_{taper} = 74 \pm 12$ nm.

Figure 7.4 shows the dependence of the size of the hotspot on the overall detection probability. We find - suprisingly - that lower detection probabilities (i.e. lower currents) correspond to larger hotspots. Interestingly, we observe that the 0 nm bridge deviates from the behaviour of the other devices at low detection probabilities. The 100 nm bridge follows the trend of the 200 nm and 400 nm bridge up until $s_{hs} \approx 75$ nm, and then deviates as well. We explain this result by pointing to the limited size of these devices; the 100 nm curve starts to deviate at the point where the size of a hotspot becomes comparable to the size of the detector. For the 200 and 400 nm bridges, we find values of s as large as 200 nm at $p_2 = 2 * 10^{-3}$, corresponding to $I_b = 13.5 \mu\text{A}$. Decreasing the current further, we arrive in the regime where three-photon detection events become dominant, and our analysis breaks down.

Figure 7.5 shows the dependence of the ratio η_2/η_1 on the wavelength of the incident photons, using a 100 nm long detector from a different film.

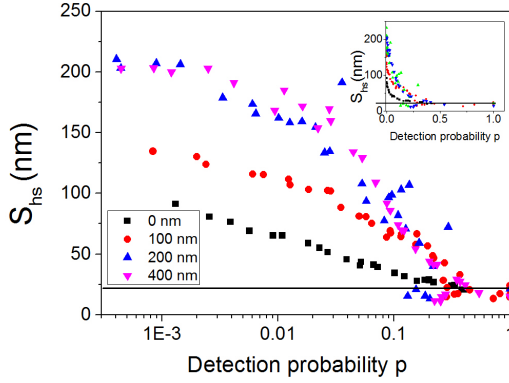


Figure 7.4: Dependence of hotspot size on detection probability. We plot the size of the hotspot as a function of the internal detection probability p_1 . *Inset*: the same data as in the main figure, but plotted on a linear scale. In both the main figure and the inset, the black line indicates the hotspot size of $s_{hs} = 22$ nm, which is found in the limit of high detection probability.

For this experiment, we used a filtered Fianium supercontinuum laser, which has a specified pulse duration for its seed laser of 7 ps. We note that the observed value of η_2/η_1 is independent of photon energy. This is a strong indication of the role of diffusion in the detection process: since the diffusion equation is linear, this result can be interpreted in a very natural way in this context. In the normal-core model, in contrast, one would expect a $1/\sqrt{\lambda}$ dependence, which would mean almost a factor 2 difference over the wavelength range at which we performed experiments.

We note that the value of η_2/η_1 which is observed here is slightly higher than for the data reported on in Figures 7.1-7.4: if converted to a value for s using the same method, this would give a value of $s = 35$ nm. We note, however, that the laser used in this experiment has a temporal profile which is not well-suited to this experiment. In fact, it is expected that the pulse duration should depend on wavelength, increasing strongly with the difference $|\omega - \omega_{pump}|$, where ω is the frequency of the required light, and ω_{pump} is the pump frequency, to a value of several tens of ps³. We note that no evidence of this is visible in our measurements. Moreover, we note that the 100 nm detector used for this experiment was from a different film than the ones reported on above, which is known to give rise to larger fluctuations in properties than between detectors on the same film. We stress the preliminary character of these measurements.

Using the diffusion coefficient $D = 0.5$ cm²/s, which is more or less constant for all SSPDs reported on in the literature, we may convert our

³This statement is based on private communication with Fianium Ltd.

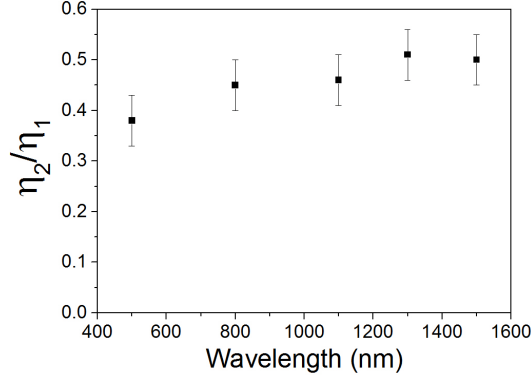


Figure 7.5: Values of η_2/η_1 for a 100 nm long device, measured with a filtered Fianium supercontinuum laser.

effective length to a time scale using the 2D-diffusion relation $s = \sqrt{Dt}$. For our high-detection probability value of $s = 22$ nm, we find $t_{hs} = 10 \pm 2$ ps. For the low-detection probability limit, we arrive at $t_{hs} = 800$ ps, which is comparable to the quasiparticle recombination time $t_r = 1000$ ps. We speculate that the recombination of quasiparticles could be the reason why the increase of the effective interaction distance saturates at 200 nm. More work at this point - especially on longer wires - is certainly necessary to obtain an answer to this question.

Next, we consider the observed detection probability dependence of s . By relying on the power-dependence of two-photon detection events, we postselect on those events where exactly two photons play a role. It is therefore natural to consider the quasiparticle density at a point inbetween the two photon absorption spots. Since diffusion occurs not only towards this point but in all directions, the quasiparticle density at the point where a detection event is supposed to occur will be lower for photons with high separation. If the required detection probability is lower, the absorption positions can therefore be further apart. This argument offers a qualitative explanation for the increase of s at lower detection probabilities, but a full theory would have to take into account the effect of the reduced bias current as well as all possible combinations of absorption positions.

Finally, we consider the measurement of the effective taper length $l_{taper} = 74 \pm 12$ nm. We consider three effects: the intrinsic spread in efficiency of the detector as a function of transverse position (which we considered in Chapter 5), the accuracy with which our constriction is defined, and the observed overall efficiency.

In Chapter 5, we demonstrated that the edges of the wire have a lower threshold current than the center part of the wire. This means that there

is a range of currents for which only the edges of the wire are efficiently photodetecting. This difference in threshold currents was calculated to be $\Delta I_{edge,center} = 0.14I_c$, which is in reasonable agreement with the value of $\Delta I_{edge,center} \approx 0.2I_c$ found experimentally. To make an order of magnitude estimate of the expected length over which the taper is still photodetecting, we adopt a zeroth-order approximation in which we consider the effect of the taper on the current density but not on any other photodetection properties of the wire. We find that the distance in the taper at which the edges of the wire are still photodetecting lies 30 nm away from the center of the constriction, pointing to a theoretical value of $l_{taper,th} = 60$ nm. Moreover, we must consider that at a given bias current, detection events in the taper will occur with lower probability, which we demonstrated results in a larger interaction length. We note, however, that this is a strong oversimplification as the photodetection will become less efficient because the wire is wider, which would lead to a lower estimate for l_{taper} .

Secondly, we must also consider the radius of curvature with which the central section of our zero-length bridge is defined, which is in the range of 5-10 nm. This would be added to any estimate of the photodetecting length. Thirdly, in Chapter 2, we measured a value of $\eta = 1.5 * 10^{-4}$ at high current for a detector nominally identical to this one. Taking the absorptance calculated in Chapter 5 and using the assumptions of uniform efficiency and illumination, we find $l_{taper} = 50$ nm. We therefore conclude that our measured value for the taper photodetection length is of the right order of magnitude.

7.5 Discussion

Multiphoton detectors suffer from overall low efficiency. Unfortunately, our results point to the fact that this efficiency cannot be strongly enhanced by increasing the length of the wire, at least for high detection probabilities. If the wire length is increased, the sample functions effectively as a series of independent nanodetectors one after each other, leading only to a linear enhancement in efficiency. A much better solution to enhance the multiphoton detection probability would be to introduce a thicker film for enhanced local absorption, or a cavity structure, since that enhances the absorption probability per photon, leading to quadratic instead of linear improvement in the two-photon regime.

The technological advantage of the low value of s_{hs} is that in any kind of spatially resolved two-photon imaging scheme, it is possible in principle to obtain far-subwavelength resolution using an appropriately current-biased nanodetector in two-photon mode. One could imagine, for example, running an asymmetric detector at such a current that only one edge is photodetecting. Then, one could sample the two-photon near field with a resolution of approximately 20 nm in one direction and some tens of nm in the other.

We demonstrated previously⁴ that the detection probability depends strongly on the position along the cross-section of the wire where the photon is absorbed. This applies more strongly to multiphoton detection events. It is therefore clear that our measured length is an ensemble average of all possible pairs of absorption locations, weighted by the probability that those absorption locations produce a detection event. At very low detection probabilities, the overall detection probability is exponentially dominated by detection events at the edge of the wire. We therefore conclude that at low detection probability ($p \lesssim 0.05$) [35], we have measured the effective interaction length between photons which are absorbed at the edges of the wire.

We expect that the hotspot size which we have measured is a size along the length of the wire. The reason for this is as follows: since we must satisfy current continuity in the wire, an absorbed photon causes a disruption across the entire width of the wire. Apart from the corrections due to the inhomogeneity of the threshold current mentioned in the previous paragraph, we therefore expect that the interaction distance which we have measured is the component of the absorption distance along the length of the wire. Since the width of our wire is much smaller than the observed hotspot length, however, we can safely assume that hotspots are circular, assuming an isotropic diffusion constant. A full study of these problems would require a thorough sampling of all possible multiphoton absorption events, which could be done most efficiently through a Monte Carlo simulation. This is however beyond the scope of the present work.

We note that the position-dependent detection efficiency carries in it a length scale as well: from Figure 5.4, we observe that there is a plateau of low threshold currents at the edges of the curve, which is approximately 30 nm wide. Since the threshold current is reduced when the hotspot is in contact with the edge of the film, this provides another, more indirect measure of the hotspot size. This measurement is in reasonable agreement with the one presented here.

A experiment similar to ours was performed in WSi [123], where a constant, bias-current independent value of $s_{hs} = 100$ nm was found. This result is supported by numerical simulations of quasiparticle multiplication and diffusion [32], which show that due to the lower density of states at the Fermi level and the lower gap, even a photon with a relatively small energy can make a significant part of the cross-section of the wire normal.

7.6 Conclusion

We have demonstrated a direct measurement of the hotspot size in a series of NbN superconducting single-photon detectors. We find a hotspot interaction size of 22 nm, which increases rapidly to a value of 200 nm when the detection

⁴See Chapter 5.

probability (or equivalently, the bias current) is decreased. We have shown that this length is independent of wavelength. We have interpreted this data in the context of the diffusion of quasiparticles. Our results show that far-subwavelength imaging with a suitably engineered SSPD is in principle possible.

Chapter 8

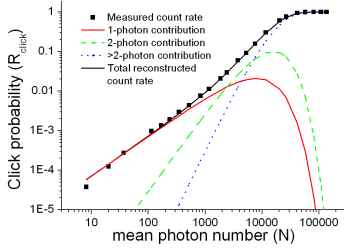
Conclusion and Future Work

8.1 Summary

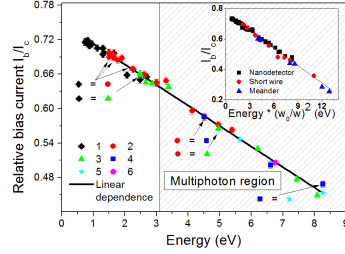
The main result of this thesis is strong experimental evidence for a diffusion-based vortex crossing detection mechanism in superconducting single-photon detectors. The physical picture which arises from our experiments is as follows: when a photon is absorbed, a cloud of quasiparticles is created. That cloud spreads, forming an obstacle which diverts some of the bias current towards the edges of the wire. This removes the energy barrier that otherwise prevents vortices from entering the film, causing a vortex to enter. This vortex then causes a transition to the normal state by the friction experienced as it is pulled across the wire by the Lorentz force.

We have provided the following experimental evidence for this picture (see Figure 8.1):

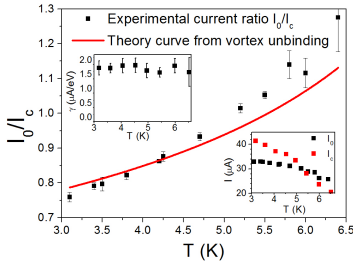
- We have demonstrated that the number of photons that excite the detector does not influence the detection response directly. Rather, only the overall energy of the excitation, combined with the applied bias current, sets the detection probability. This is evidence that it is the total amount of quasiparticles at the band-edge in some relevant volume that sets the detection probability.
- We find that the energy-current relation is linear in applied bias current and photon energy (see Figure 8.1b). This is strong evidence for the role of diffusion: in a model where there is no point in the wire that is in the normal state, the effect of the impinging photon on the superconductivity is only through the reduction of the Cooper pair density.
- We find that the temperature dependence of the device follows the temperature dependence of the energy scale for vortex entry into the



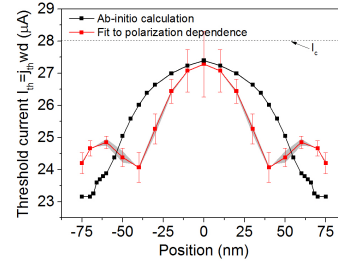
(a) From Chapter 2: Quantum detector tomography on an SSPD - the workhorse experiment of this thesis



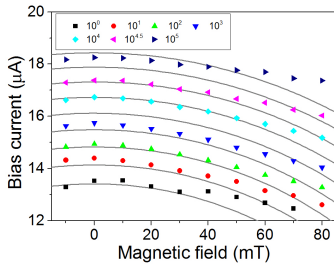
(b) From Chapter 4: The linear energy-current relation in SSPDs.



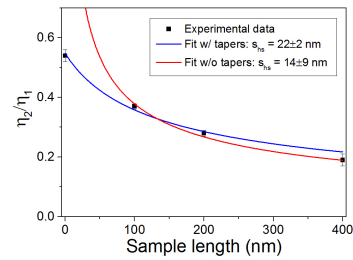
(c) From Chapter 4: Temperature dependence of the internal detection mechanism of an SSPD, which follows that of the energy scale for vortex entry (red line).



(d) From Chapter 5: The experimentally derived position-dependent internal detection efficiency, as well as a theory curve computed for the diffusion-based vortex model.



(e) From Chapter 6: The quadratic dependence of bias current on applied magnetic field, for constant detection probability.



(f) From Chapter 7: Measurement of the size of a hotspot in an SSPD.

Figure 8.1: The main results of this thesis. Full descriptions of each figure can be found in the respective chapters.

film (see Figure 8.1c). This is evidence for the role of vortices in the detection mechanism.

- We find that the detector is polarization-sensitive in its internal detection probability, which is evidence of a position-dependent internal detection efficiency (IDE) (See Figure 8.1d). We have reconstructed this position-dependent IDE with a resolution of approximately 10 nm. We find that the edges of the wire have a lower threshold current for photodetection than the center of the wire, leading to a regime where the wire is more efficiently photodetecting at the edges than in the center. The explanation for this is that the vortex barrier is lowered by the presence of quasiparticles, so if the quasiparticle cloud is in contact with the edge of the wire, the current required for vortex entry is reduced. This is further evidence for the role of vortices in the detection mechanism.
- We have measured the size of the excitation in the detector, which we found to be 22 nm (see Figure 8.1f). Our preliminary result is that this value is independent of wavelength, which fits with our physical picture. Moreover, this length scale is in reasonable agreement with the distance at which we observe strongly reduced threshold currents in our position-dependent IDE.

Moreover, we have studied the magnetic field dependence of the detection mechanism (see Figure 8.1e). While our explanation for that field dependence is conceptually separate from the model described above, it is entirely compatible with it. The reason for this is that our description, which is based on the Usadel equation, is concerned with the initial properties of the film, whereas the model described above is concerned with the dynamics of the detection event itself. We do observe that the permanent presence of a vortex in the material is strongly detrimental to the detection mechanism.

8.2 Detection Models

We discuss the implications of our results for the four models: the normal-core hotspot model, the diffusion-based hotspot model, the normal-state vortex model and the diffusion-based vortex model (see Section 1.2).

Although the normal-core model appears not to be applicable to NbN, recent simulations show [32] that in WSi the normal state might play a role in detection events. Moreover, recent experiments similar to Chapter 7 of this thesis show that in WSi the hotspot is well approximated as an object of constant size, indicating that there is no role for diffusion [123]. These results can be interpreted as evidence for the normal-core model in WSi, although the definitive experiment on this topic has not yet been performed. Moreover, it is known that for keV excitations, the normal-core model is valid [75, 85].

The diffusion-based hotspot model has the strong advantage that it generates the correct energy-current relation. It is, however, not able to capture all the physics of the detection event, such as the temperature dependence and the position dependence of the internal detection efficiency. However, this model has an important role as a toy model and a guide for experiments, since it is the most correct model for which an analytical expression is available. Moreover, more advanced models have not yet been able to reproduce the width dependence which is implied by this model [16].

Lastly, we turn to the two vortex-based models. Both models predict a position-dependent detection efficiency [32, 34], and both models have a role for vortices. Moreover, with the most recent refinements, the normal-state vortex model also has an energy-current relation which is able to account for the experimental results. Since it is clear that the models are quite evenly matched, it is best to set out some of the conceptual differences. In the normal-state vortex model, vortices arise naturally, whereas additional assumptions are needed to relate the size of the hotspot to the incoming photon energy. In the diffusion-based vortex model, on the other hand, the entry of vortices has to be computed separately from the rest of the model, while the hotspot is included naturally. This is due to the fact that the normal-state model was computed in the Ginzburg-Landau formalism, whereas the diffusion-based model was computed in the London formalism.

Apart from conceptual differences, the two models currently have one big experimental difference: in the diffusion-based vortex model, vortices always enter from the side of the wire, whereas in the normal-state based model, vortices can also form around the hotspot. This difference is amenable to further experiments.

8.3 Future Work

Based the discussion above, we envisage two lines of experiments. First, a series of measurements of the energy-current relation on detectors of different materials would answer the question whether the mechanisms which we have studied for NbN SSPDs are generic for all SSPDs, or whether there is a crossover to normal-state behaviour. This could be done by investigating WSi or one of the other amorphous materials, but another interesting candidate would be MgB₂, out of which SSPDs were fabricated only recently [101]. MgB₂ has a higher T_c than NbN and therefore represents a data point 'in the other direction' compared to WSi.

A second line of inquiry should look into the differences between the normal-state vortex model and diffusion-based vortex model. The difference in the vortex entry locations is most easily accessed via the magnetic field. Since the current density in the middle of the wire is not disturbed by the presence of a magnetic field, detection events which occur there should experience only a weak influence on an applied magnetic field. In the diffusion-

based model, in contrast, all detection events should be strongly influenced by the field since the effect of the applied magnetic field is strongest at the edges [35]. This experiment has been done in Chapter 7 of this thesis. We showed that the predictions of the version of the diffusion-based vortex model presented in [24, 25] are contradicted by experiments. However, there are at present no predictions from the more advanced versions of this model. Therefore what is needed to resolve this question is further refinement of the theoretical models.

There are still some open problems within the topic of SSPD detector physics. First, as mentioned previously, there is no good theoretical account of the width dependence yet. Second, while we have demonstrated a current scale which follows the temperature dependence of vortex entry, in principle in the diffusion-based vortex models, this current scale should be the critical current. There is no theoretical explanation for the experimentally observed regime in which the detector doesn't respond to single photons while operating close to the critical current.

Connected to this last problem is the issue of dark counts. We have seen repeatedly throughout this thesis that dark counts behave qualitatively different than photon counts. In particular, dark counts do not behave as $E = 0$ excitations. While part of this issue, presented in Chapters 3 and 4, is resolved by the position-dependent detection efficiency presented in Chapter 5, this is not a complete solution. Moreover, dark counts and photon counts also differ in their response to a magnetic field. This is still an open problem, for which measurements of very low-energy excitations would be useful [16].

8.4 Conclusion

In summary: we have studied the detection mechanism in superconducting single-photon detectors through quantum detector tomography. We have studied single and multiphoton excitations on a nanodetector and a series of bridge samples of varying lengths. We have demonstrated strong evidence for the role of vortices in the detection mechanism. We have investigated the temperature and position dependence of the detection mechanism. These results pave the way to a complete, quantitative understanding of superconducting single-photon detectors.

Samenvatting

Dit proefschrift beschrijft onderzoek naar het werkingsprincipe van supergeleidende fotondetectoren (SSPDs, naar het Engelse acroniem). Zulke detectoren hebben belangrijke technologische toepassingen, maar er is nog veel onbekend over het werkingsmechanisme. Om deze detectoren te onderzoeken maken we gebruik van *quantumdetectortomografie* (QDT). Dit is een methode om de respons van een fotondetector in de basis van aantaltoestanden (Fock-basis) te meten. In het eerste, inleidende hoofdstuk geven we een korte introductie op de stand van het vakgebied en van de technieken die in dit proefschrift gebruikt worden. We bespreken verder de verschillende theorieën die opgesteld zijn voor het detectiemechanisme van SSPDs.

In het tweede hoofdstuk demonstreren we hoe quantumtomografie gebruikt kan worden om een supergeleidende fotondetector te karakteriseren. We hebben de methode aangepast om hem geschikt te maken voor detectoren met een kleine absorptie. Door een extra factor in de vergelijkingen toe te voegen die deze absorptiekans beschrijft kunnen we de (interne) detectiekans na absorptie scheiden van de absorptiekans zelf. Door het toevoegen van deze extra variabele wordt het systeem van vergelijkingen dat onze respons beschrijft onbepaald; we lossen dit op door via een aanname van schaarsheid (sparsity) modelselectie te introduceren. We vinden dat de absorptiekans overeenkomt met de op basis van de experimentele geometrie verwachte waarde. We vinden verder dat de absorptiekans onafhankelijk is van de instelstroom door de detector. Uit deze twee waarnemingen trekken we de conclusie dat we daadwerkelijk de interne en externe processen in de detector gescheiden hebben. We laten zien dat de detector niet-lineair gedrag kan vertonen: het is mogelijk om de instelstroom zo te kiezen dat de detector sterker reageert op twee tegelijkertijd geabsorbeerde fotonen dan op basis van de detectiekans van individuele fotonen te verwachten is.

In het derde hoofdstuk beginnen we met de fysische interpretatie van de meetresultaten die verkregen zijn door QDT. In dit hoofdstuk wordt de *energie-stroomrelatie* geïntroduceerd, die verderop een cruciale rol zal spelen. De energie-stroomrelatie is het functioneel verband dat aangeeft hoeveel instelstroom nodig is om een foton van een gegeven energie met een vooraf gekozen detectiekans (typisch 1%) te detecteren. We laten zien dat enkel de totale energie van de excitatie belangrijk is voor de energie-stroomrelatie, en

niet de manier waarop die energie over een aantal fotonen verdeeld is. Met andere woorden: als de detector aangeslagen wordt door twee fotonen met een golflengte λ , dan reageert de detector precies zo als wanneer hij aangeslagen wordt met een foton met golflengte $\lambda/2$. We laten zien dat er een universele responscurve bestaat voor SSPDs: voor detectiekansen tussen de 10^{-4} en 0.3 is de detectiekans enkel een functie van een lineaire combinatie van de totale energie en instelstroom. We vinden dat de dark counts zich niet aan deze relatie houden.

Het vierde hoofdstuk is gewijd aan een meting van de energie-stroomrelatie. De verschillende modellen van het werkingsmechanisme in een SSPD zijn van elkaar te onderscheiden doordat ze elk een andere voorspelling doen voor deze energie-stroomrelatie. We maken gebruik van de in hoofdstuk 2 vastgestelde eigenschappen van multifotonexcitatie om het dynamisch bereik van onze meting op te rekken tot in het vacuum-ultraviolet. Door verschillende fotonaantallen binnen een enkel experiment met elkaar te vergelijken lukt het ons om de energie-stroomrelatie met een precisie van 50 nA te meten. We vinden dat de energie-stroomrelatie ook bij deze nauwkeurigheid lineair is. Hiermee sluiten we modellen uit waarin er een cilindervormig normaal domein in de detector aanwezig is, of laten we in ieder geval zien dat het normale domein geen rol speelt in de detectiegebeurtenis. Vervolgens meten we de temperatuurafhankelijkheid van de energie-stroomrelatie. We vinden dat deze de temperatuurafhankelijkheid volgt van de intreeënergie van een vortex in het materiaal. Hieruit trekken we de conclusie dat vortices een belangrijke rol spelen in de detectiegebeurtenis. We concluderen dat in het detectiemechanisme zowel diffusie van quasideeltjes als vortexdynamica een belangrijke rol spelen.

In hoofdstuk vijf onderzoeken we de energie-stroomrelatie op microscopisch niveau. Door de detector aan te slaan met licht van verschillende polarisaties en golflengtes kunnen we selectief excitatie aanbrengen op verschillende posities in de breedterichting van de draad. We nemen waar dat licht dat loodrecht op de draad gepolariseerd is een lagere instelstroom nodig heeft dan licht dat parallel aan de draad gepolariseerd is. Omdat de parallelle polarisatie meer in het midden geabsorbeerd wordt, leiden we hieruit af dat de grenswaarde van de instelstroom die nodig is om een detectiegebeurtenis te veroorzaken aan de randen van de draad lager is dan in het midden van de draad. Deze resultaten bieden een verklaring voor het verschijnsel dat de stroom die nodig is voor een efficiënte detector geen scherpe drempelwaarde heeft: bij lage stromen worden de randen van de detector actief, en naarmate de stroom hoger wordt, gaat langzaam steeds meer van het midden meedoen met het detectieproces. We vergelijken deze metingen met berekeningen in de context van een numeriek model dat diffusie van quasideeltjes, herverdeling van stroom onder invloed van de quasideeltjes en het binnendringen van vortices omvat. We zien sterke kwalitatieve overeenkomst: zowel het model als het experiment voorspellen een gebied midden in de draad waar de grenswaarde van de instelstroom min of meer constant is, gevolgd door een snel

dalende waarde aan de randen. De berekende waarde en de experimentele waarden liggen minder dan een factor 2 uit elkaar.

In het zesde hoofdstuk onderzoeken we hoe de detectiekans afhangt van een extern aangebracht magneetveld. We vinden drie regimes. Bij lage magneetvelden neemt de benodigde instelstroom voor een vaste detectiekans kwadratisch af met toenemend magneetveld. In een tussenregime wijkt de detector af van dit gedrag; de benodigde stroom neemt nog steeds af, maar minder sterk dan op basis van het kwadratisch verband verwacht zou worden. In het derde regime is de detectiekans slechts zwak afhankelijk van de instelstroom. We interpreteren het kwadratisch regime in termen van de oplossing van de Usadel-vergelijking voor een homogene stroomdragende draad in een magneetveld. We vinden goede overeenstemming tussen de gemeten en berekende waarden van de coëfficiënten die het functioneel verband tussen instelstroom en magneetveld beschrijven. Voor de andere twee regimes vinden we een kwalitatieve verklaring die steunt op het idee dat er permanent vortices in de draad aanwezig zijn. Uit deze resultaten trekken we de conclusie dat het onmogelijk is om het fundamentele detectiemechanisme efficiënter te maken door een magneetveld aan te leggen. Metingen waarbij dit wel gezien is, moeten geïnterpreteerd worden in termen van herverdeling van de stroom door bochten en andere obstakels in meanderstructuren.

In hoofdstuk zeven presenteren we een voorlopige dataset van metingen aan de interactielengte tussen twee excitaties naast elkaar in de draad. Op basis van eerdere experimenten verwachten we dat er een zekere afstand is waarbinnen de twee excitaties samen tot een detectiegebeurtenis leiden. We vinden dat deze afstand ongeveer 25 nm bedraagt voor de hoogste stromen die we in ons experiment kunnen bereiken. Bij lagere stromen neemt de interactieafstand linear af. Deze metingen zijn kwalitatief consistent met de modellen die we in eerdere hoofdstukken hebben onderzocht.

In het laatste hoofdstuk vatten we de belangrijkste conclusies uit het proefschrift samen.

Acknowledgements

Science is at heart a collective endeavour, so a sincere thanks to all who made this work possible is in order. First, I thank those who were involved in the supervision of my PhD project: Martin van Exter, Andrea Fiore and Dirk Bouwmeester. I thank my colleagues on the SSPD work: Michiel de Dood and Qiang Wang. Michiel has had a huge if informal guiding role during the last four years. I thank Qiang for the FDTD simulations which are a vital element in Chapter 5 of this thesis, and for many scientific discussions. I thank my students - Shawn Levie, Chris Lemmens, Marc van Kralingen, Bob Rengeling and Irina Komen, who all contributed to the content of this thesis. Marc, Bob and Irina worked on the challenging magnetic field experiments presented in Chapter 6.

When I started this project, I knew next to nothing about superconductivity. I thank Peter Kes, Jan Aarts, Andreas Engel, Denis Vodolazov and Eduard Driessen for filling that gap. I would in particular like to thank Andreas for scientific discussions on his numerical model and SSPD physics in general. I thank Richard Gill for scientific discussions about the statistical methods used in this thesis. I thank Michael Furtado for proofreading the manuscript of this thesis.

I thank the people from the PSN group in Eindhoven. In particular, I am indebted to Rosalinda Gaudio for producing the majority of samples on which the work in this thesis was done, and to Giulia Frucci for teaching me how to work with SSPDs. Furthermore, I thank Saeedeh Jahanmirinejad, Zili Zhou and Döndü Sahin for sample fabrication and many useful discussions. I thank Alessandro Gaggero, Francesco Mattioli and Roberto Leoni from CNR-IFN Rome for sample fabrication and scientific discussions.

The excellent support at LION is one of the things that makes it such a good place for science. I thank Henriette van Leeuwen, Marcel Hesselberth, Arno van Amersfoort, Rene Overgaw, Raymond Koehler, Emiel Wieggers, Fred Schenkel and Jeroen Mesman. I thank Daan Boltje in particular, whose last-minute wirebonding saved valuable measurement time on more than one occasion. I thank Doreen Wernicke from Entropy GmbH.

Finally, I would like to thank Vera, for being a constant support. Without her, this thesis would not have been possible.

Curriculum Vitae

Jelmer Renema was born on the 4th of July 1986 in Hoogeveen. He graduated from Groene Hart Lyceum secondary school in 2003 with a specialization in science and technology and went on to study physics at Leiden University. Jelmer obtained a BSc from that university; the final project was *Surface plasmon spectroscopy*. He then went on to do an MSc at Leiden University, with two projects: *Two-photon interference on Young's double slit* and *Magnetometry and entanglement with room-temperature caesium atoms*. After a year at the Niels Bohr Institute working on cold atomic ensembles he returned to Leiden to work on superconducting single-photon detectors in the group of Dirk Bouwmeester.

List of Publications

1. W.H. Peeters, J.J. Renema, M.P. van Exter *Engineering of two-photon spatial quantum correlations behind a double slit* Phys. Rev. A **79** (4), 043817 (2009)
2. W. Wasilewski, K. Jensen, H. Krauter, J.J. Renema, M.V. Balabas, E.S. Polzik *Quantum noise limited and entanglement-assisted magnetometry* Phys. Rev. Lett. **104** (13), 133601 (2010)
3. A. Louchet-Chauvet, J. Appel, J.J. Renema, D. Oblak, N. Kjaergaard, E.S. Polzik *Entanglement-assisted atomic clock beyond the projection noise limit* New J. Phys. **12** (6), 065032 (2010)
4. J.J. Renema, G. Frucci, Z. Zhou, F. Mattioli, A. Gaggero, R. Leoni, M.J.A. de Dood, A. Fiore, M.P. van Exter *Modified detector tomography technique applied to a superconducting multiphoton nanodetector* Opt. Exp. **20** (3), 2806-2813 (2012) (Chapter 2 of this thesis)
5. A.J.H. van der Torren, S.C. Yorulmaz, J.J. Renema, M.P. van Exter, M.J.A. de Dood *Spatially entangled four-photon states from a periodically poled potassium-titanyl-phosphate crystal* Phys. Rev. A **85** (4), 043837 (2012)
6. J.J. Renema, G. Frucci, M.J.A. de Dood, R. Gill, A. Fiore, M.P. van Exter *Tomography and state reconstruction with superconducting single-photon detectors* Phys. Rev. A **86** (6), 062113 (2013)
7. J.J. Renema, G. Frucci, Z. Zhou, F. Mattioli, A. Gaggero, R. Leoni, M.J.A. de Dood, A. Fiore, M.P. van Exter *Universal response curve for nanowire superconducting single-photon detectors* Phys. Rev. B **87** (17), 174526 (2013) (Chapter 3 of this thesis)
8. J.J. Renema, R. Gaudio, Q. Wang, Z. Zhou, A. Gaggero, F. Mattioli, R. Leoni, D. Sahin, M.J.A. de Dood, A. Fiore, M.P. van Exter *Experimental Test of Theories of the Detection Mechanism in a Nanowire Superconducting Single-Photon Detector* Phys. Rev. Lett. **112** (11), 117604 (2014) (Chapter 4 of this thesis)

9. J.J. Renema, R.J. Rengelink, I. Komen, Q. Wang, R. Gaudio, K.P.M. op 't Hoog, Z. Zhou, D. Sahin, A. Fiore, P. Kes, J. Aarts, M.P. van Exter, M.J.A. de Dood, and E.F.C. Driessen, *The Magnetic Field Response of Nanowire Superconducting Single-Photon Detectors* Submitted to Applied Physics Letters (Chapter 6 of this thesis)

List of Symbols and Material Parameters

Symbol	Name	Value/expression	Reference
$A(x)$	Local absorption probability	-	-
B	Magnetic field	-	-
B_0	Field scale	350 mT	-
B_Γ	Usadel field scale	$\sqrt{6}\hbar/ew\xi = 2.7$ T	^a
χ^2	Goodness of fit	$\chi^2 = \sum_i \frac{(y_{i,exp} - y_{i,fit})^2}{\sigma_i^2}$	-
c	Speed of light	$3.00 * 10^8$ m/s	-
C	Photon count rate	-	-
C_e	Hot electron density	-	-
C_{qp}	Quasiparticle density	-	-
c_i	Expansion coefficient	$c_i = e^{-N} \frac{N^i}{i!}$	^b
d	Thickness	4.9 nm	-
D	Diffusion constant	0.4 cm ² /s	-
Δ	Superconducting gap	1.9 meV @ 1.5 K	-
ε_0	Vortex entry energy	$\Phi^2/2\pi\mu_0\Lambda_\perp = 67.6$ meV	[25]
ϵ	Dielectric constant	-	-
E	Excitation energy	-	-
Φ_0	Elementary flux quantum	$h/2e = 2.067$ fWb	-
γ	Energy-current interchange	2.9 μ A/eV	^a
$\gamma'(x)$	Local value of γ	-	-
Γ	Intrinsic pair breaker	≈ 100 μ eV	-
η	Linear optical efficiency	-	-
h	Planck's constant	4.14 feV s	-

^aFor a 150 nm wide detector

^bFor coherent states

Symbol	Name	Value/expression	Reference
I_b	Bias current	-	-
I_c	Critical current	28 μA	^a
I_0	Reference current	$I_0 \approx 0.8I_c$	^b
I_{th}	Threshold current	$I_{th} = I_c - \gamma E$	-
I_Γ	Usadel current scale	$\sqrt{2\Delta}/eR(\xi) = 180 \mu\text{A}$	^a
j	Current density	-	-
j_c	Critical current density	40 GA/m^2	-
j^*	Rolloff current density	0.9 GA/m^2	-
k_b	Boltzman constant	$8.6 * 10^{-5} \text{eV}/\text{K}$	-
λ	Penetration length	430 nm, 500 nm	[28, 21]
λ	Optical wavelength	-	-
λ_c	Cutoff wavelength	-	-
Λ_\perp	Effective penetration length	50 μm	-
L	Wire length	-	-
l_{taper}	Taper effective length	74 nm	-
μ_0	Magnetic permeability of vacuum	$4\pi * 10^{-7} \text{N}/\text{A}^2$	-
n_{max}	Model selection cutoff	-	-
n_{se}	Density of supercond. electrons	-	-
N_0	Density of states	51 nm^3/eV	[28]
N	Mean photon number	-	-
ν_h	Reduced vortex entry energy	3-8, 40-110	[25, 26] ^c
ν	Vortex entry energy	$\varepsilon_0/k_bT = 250$	[25]
ν	Photon energy	-	-
p_n	Internal detection probability	-	-
$P(x)$	Local detection probability	-	-
ζ	QP conversion efficiency	0.25	[28]
R	Detection probability per pulse	-	-
R_\square	Sheet resistance	600 Ω	-
s	Hotspot size	22 nm	-
t	Reduced temperature	T/T_c	-
T	Temperature	-	-
T_c	Critical temperature	9.5 K	-
τ	Timescale for QP multiplication	1.6 ps	[28]
v_s	Supercond. velocity	-	-
v_c	Critical velocity	-	-
V	Visibility	-	-
w	Wire width	-	-
ξ	Coherence length	3.9 nm	-

^aFor a 150 nm wide detector^bFor low threshold values^cFor photon counts and dark counts, respectively

Bibliography

- [1] G. N. Goltsman, O. Okunev, G. Chulkova, A. Lipatov, A. Semenov, K. Smirnov, B. Voronov, A. Dzardanov, C. Williams, and R. Sobolewski, "Picosecond superconducting single-photon optical detector," *Appl. Phys. Lett.*, vol. 79, no. 6, p. 705, 2001.
- [2] M. Eisaman, J. Fan, A. Migdall, and S. Polyakov, "Single-photon sources and detectors," *Rev. Sci. Instrum.*, vol. 82, p. 071101, 2011.
- [3] C. Natarajan, M. Tanner, and R. Hadfield, "Superconducting nanowire single-photon detectors: physics and applications," *Supercond. Sci. Technol.*, vol. 25, no. 6, p. 063001, 2012.
- [4] F. Marsili, F. Najafi, E. Dauler, F. Bellei, X. Hu, M. Csete, R. Molnar, and K. Berggren, "Single-photon detectors based on ultranarrow superconducting nanowires," *Nano Lett.*, vol. 11, p. 2048, 2011.
- [5] R. Collins, R. Hadfield, V. Fernandez, S. Nam, and G. Buller, "Low timing jitter detector for gigahertz quantum key distribution," *Electron. Lett.*, vol. 43, no. 3, p. 180, 2007.
- [6] D. M. Boroson, J. J. Scozzafava, D. V. Murphy, and B. S. Robinson, "The Lunar Laser Communications Demonstration (LLCD)," *2009 Third IEEE International Conference on Space Mission Challenges for Information Technology*, no. Llcd, pp. 23–28, 2009.
- [7] K. M. Rosfjord, J. K. W. Yang, E. A. Dauler, A. J. Kerman, V. Anant, B. M. Voronov, G. N. Goltsman, and K. K. Berggren, "Nanowire single-photon detector with an integrated optical cavity and anti-reflection coating," *Opt. Express*, vol. 14, no. 2, pp. 527–34, 2006.
- [8] M. Hofherr, D. Rall, K. Il'in, M. Siegel, A. Semenov, H.-W. Hübers, and N. A. Gippius, "Intrinsic detection efficiency of superconducting nanowire single-photon detectors with different thicknesses," *J. Appl. Phys.*, vol. 108, no. 1, p. 014507, 2010.
- [9] A. J. Kerman, E. A. Dauler, W. E. Keicher, J. K. W. Yang, K. K. Berggren, G. Goltsman, and B. Voronov, "Kinetic-inductance-limited

- reset time of superconducting nanowire photon counters,” *Appl. Phys. Lett.*, vol. 88, no. 11, p. 111116, 2006.
- [10] V. Anant, A. J. Kerman, E. A. Dauler, K. W. Joel, K. M. Rosfjord, and K. K. Berggren, “Optical properties of superconducting nanowire single-photon detectors,” *Opt. Express*, vol. 16, no. 14, pp. 46–52, 2008.
- [11] E. F. C. Driessen, F. Braakman, E. Reiger, S. Dorenbos, V. Zwiller, and M. J. A. de Dood, “Impedance model for the polarization-dependent optical absorption of superconducting single-photon detectors,” *Eur. Phys. J. Appl. Phys.*, vol. 47, p. 10701, 2009.
- [12] E. Driessen and M. de Dood, “The perfect absorber,” *Appl. Phys. Lett.*, vol. 94, p. 171109, 2009.
- [13] V. Verma, F. Marsili, S. Harrington, A. Lita, R. Mirin, and S. Nam, “A three-dimensional, polarization-insensitive superconducting nanowire avalanche photodetector,” *Appl. Phys. Lett.*, vol. 101, p. 251114, 2012.
- [14] J. Kitaygorsky, “Photon and dark counts in NbN superconducting single-photon detectors and nanostripes,” Ph.D. dissertation, University of Rochester, 2008.
- [15] A. Semenov, G. Goltsman, and A. A. Korneev, “Quantum detection by current carrying superconducting film,” *Physica C*, vol. 351, pp. 349–356, 2001.
- [16] R. Lusche, A. Semenov, K. Il’in, M. Siegel, Y. Korneeva, A. Trifonov, A. Korneev, G. Goltsman, D. Vodolazov, and H.-W. Hübers, “Effect of the wire width on the intrinsic detection efficiency of superconducting-nanowire single-photon detectors,” *J. Appl. Phys.*, vol. 116, no. 4, 2014.
- [17] J. J. Renema, R. Gaudio, Q. Wang, Z. Zhou, A. Gaggero, F. Mattioli, R. Leoni, D. Sahin, M. J. A. de Dood, A. Fiore, and M. P. van Exter, “Experimental test of theories of the detection mechanism in a nanowire superconducting single photon detector,” *Phys. Rev. Lett.*, vol. 112, p. 117604, 2014.
- [18] A. Semenov, A. Engel, H.-W. Hübers, K. Il’in, and M. Siegel, “Spectral cut-off in the efficiency of the resistive state formation caused by absorption of a single-photon in current-carrying superconducting nano-strips,” *Euro. Phys. J. B*, vol. 47, no. 4, pp. 495–501, 2005.
- [19] A. Abrikosov, “Size effect on the critical field of superconductors of the second group,” *Dokl. Akad. Nauk. SSSR*, vol. 86, p. 489, 1952.
- [20] A. Engel, A. Aeschbacher, K. Inderbitzin, A. Schilling, K. Il’in, M. Hofherr, M. Siegel, A. Semenov, and H.-W. Hübers, “Tantalum nitride superconducting single-photon detectors with low cut-off energy,” *Appl. Phys. Lett.*, vol. 100, no. 6, p. 062601, 2012.

- [21] A. Kamlapure, M. Mondal, M. Chand, A. Mishra, J. Jesudasan, V. Bagwe, L. Benfatto, V. Tripathi, and P. Raychaudhuri, "Measurement of magnetic penetration depth and superconducting energy gap in very thin epitaxial NbN films," *Appl. Phys. Lett.*, vol. 96, no. 7, p. 072509, 2010.
- [22] C. P. Bean and J. D. Livingston, "Surface barrier in type-II superconductors," *Phys. Rev. Lett.*, vol. 12, pp. 14–16, 1964.
- [23] A. D. Semenov, P. Haas, H.-W. Hübers, K. Il'in, M. Siegel, A. Kirste, T. Schurig, and A. Engel, "Vortex-based single-photon response in nanostructured superconducting detectors," *Physica C*, vol. 468, no. 7-10, pp. 627–630, 2008.
- [24] L. Bulaevskii, M. Graf, C. Batista, and V. Kogan, "Vortex-induced dissipation in narrow current-biased thin-film superconducting strips," *Phys. Rev. B*, vol. 83, no. 14, p. 144526, 2011.
- [25] L. Bulaevskii, M. Graf, and V. Kogan, "Vortex-assisted photon counts and their magnetic field dependence in single-photon superconducting detectors," *Phys. Rev. B*, vol. 85, p. 014505, 2012.
- [26] R. Lusche, A. Semenov, Y. Korneeva, A. Trifonov, A. Korneev, G. Goltsman, and H. Hübers, "Effect of magnetic field on the photon detection in thin superconducting meander structures," *Phys. Rev. B*, vol. 89, p. 104513, 2014.
- [27] R. Lusche, A. Semenov, H. W. Huebers, K. Ilin, M. Siegel, Y. Korneeva, A. Trifonov, A. Korneev, G. Goltsman, and D. Vodolazov, "Effect of the wire width on the intrinsic detection efficiency of superconducting-nanowire single-photon detectors," *arXiv:1303.4546*, 2013.
- [28] A. Engel and A. Schilling, "Numerical analysis of detection-mechanism models of superconducting nanowire single-photon detector," *J. Appl. Phys.*, vol. 114, no. 21, 2013.
- [29] J. R. Clem and K. K. Berggren, "Geometry-dependent critical currents in superconducting nanocircuits," *Phys. Rev. B*, vol. 84, p. 174510, 2011.
- [30] D. Henrich, P. Reichensperger, M. Hofherr, J. Meckbach, K. Il'in, M. Siegel, A. Semenov, A. Zotova, and D. Y. Vodolazov, "Geometry-induced reduction of the critical current in superconducting nanowires," *Phys. Rev. B*, vol. 86, p. 144505, 2012.
- [31] H. L. Hortensius, E. F. C. Driessen, T. Klapwijk, K. Berggren, and J. Clem, "Critical-current reduction in thin superconducting wires due to current crowding," *Appl. Phys. Lett.*, vol. 100, p. 182602, 2012.

- [32] A. Engel, J. Lonsky, X. Zhang, and A. Schilling, “Detection mechanism in SNSPD: Numerical results of a conceptually simple, yet powerful detection model,” *arXiv:1408.4907*, 2014.
- [33] A. N. Zotova and D. Y. Vodolazov, “Photon detection by current-carrying superconducting film: A time-dependent Ginzburg-Landau approach,” *Phys. Rev. B*, vol. 85, p. 024509, 2012.
- [34] A. Zotova and D. Vodolazov, “Intrinsic detection efficiency of superconducting single photon detector in the modified hot spot model,” *Supercond. Sci. Technol.*, vol. 27, p. 125001, 2014.
- [35] D. Y. Vodolazov, “Current dependence of the red boundary of superconducting single-photon detectors in the modified hot-spot model,” *Phys. Rev. B*, vol. 90, p. 054515, 2014.
- [36] J. S. Lundeen, A. Feito, H. Coldenstrodt-Ronge, K. L. Pregnell, C. Silberhorn, T. C. Ralph, J. Eisert, M. B. Plenio, and I. A. Walmsley, “Tomography of quantum detectors,” *Nat. Phys.*, vol. 5, no. 1, pp. 27–30, 2008.
- [37] A. Feito, J. S. Lundeen, H. Coldenstrodt-Ronge, J. Eisert, M. B. Plenio, and I. A. Walmsley, “Measuring measurement: theory and practice,” *New J. Phys.*, vol. 11, no. 9, p. 093038, 2009.
- [38] L. Artiles and R. Gill, “An invitation to quantum tomography,” *J. R. Stat. Soc. B*, vol. 67, no. 1, pp. 109–134, 2005.
- [39] D. Bitauld, F. Marsili, A. Gaggero, F. Mattioli, R. Leoni, S. Jahanmirinejad, F. Lévy, and A. Fiore, “Nanoscale optical detector with single-photon and multiphoton sensitivity,” *Nano Lett.*, vol. 10, no. 8, pp. 2977–81, 2010.
- [40] Z. Zhou, G. Frucci, F. Mattioli, A. Gaggero, S. Jahanmirinejad, T. B. Hoang, and A. Fiore, *Phys. Rev. Lett.*, vol. 110, p. 133605, 2013.
- [41] A. J. Kerman, E. A. Dauler, J. K. W. Yang, K. M. Rosfjord, V. Anant, K. K. Berggren, G. N. Goltsman, and B. M. Voronov, “Constriction-limited detection efficiency of superconducting nanowire single-photon detectors,” *Appl. Phys. Lett.*, vol. 90, no. 10, p. 101110, 2007.
- [42] A. Zotova and D. Vodolazov, “Differences in the effects of turns and constrictions on the resistive response in current-biased superconducting wire after single photon absorption,” *Supercond. Sci. Technol.*, vol. 26, p. 075008, 2013.
- [43] M. K. Akhlaghi, A. H. Majedi, and J. S. Lundeen, “Nonlinearity in Single Photon Detection : Modeling and Quantum Tomography,” *Opt. Express*, vol. 19, pp. 21 305–21 312, 2011.

- [44] M. K. Akhlaghi and A. H. Majedi, "Semiempirical Modeling of Dark Count Rate and Quantum Efficiency of Superconducting Nanowire Single-Photon Detectors," *IEEE Trans. Appl. Supercond.*, vol. 19, no. 3, pp. 361–366, 2009.
- [45] E. Knill, R. Laflamme, and G. J. Milburn, "A scheme for efficient quantum computation with linear optics." *Nature*, vol. 409, no. 6816, pp. 46–52, 2001.
- [46] I. Afek, O. Ambar, and Y. Silberberg, "High-NOON states by mixing quantum and classical light." *Science*, vol. 328, no. 5980, pp. 879–81, 2010.
- [47] A. Gaggero, S. Jahanmirinejad, F. Marsili, F. Mattioli, R. Leoni, D. Bitauld, D. Sahin, G. J. Hamhuis, R. Nötzel, R. Sanjines, and A. Fiore, "Nanowire superconducting single-photon detectors on GaAs for integrated quantum photonic applications," *Appl. Phys. Lett.*, vol. 97, no. 15, p. 151108, 2010.
- [48] J. S. Lundeen, K. L. Pregnell, A. Feito, B. J. Smith, W. Mauerer, C. Silberhorn, J. Eisert, M. B. Plenio, and I. A. Walmsley, "A proposed testbed for detector tomography," *J. Mod. Optic.*, vol. 56, no. 2-3, 2009.
- [49] G. Brida, L. Ciavarella, I. P. Degiovanni, M. Genovese, L. Lolli, G. Mingolla, F. Piacentini, M. Rajteri, E. Taralli, and M. G. A. Paris, "Full quantum characterization of superconducting photon counters," *New J. Phys.*, vol. 14, p. 085001, 2012.
- [50] T. Amri, "Quantum Behavior of Measurement Apparatus," *arXiv:1001.3032*, 2010.
- [51] A. Divochiy, F. Marsili, D. Bitauld, A. Gaggero, R. Leoni, F. Mattioli, A. Korneev, V. Seleznev, N. Kaurova, O. Minaeva, G. Goltsman, K. G. Lagoudakis, M. Benkhaoul, F. Lévy, and A. Fiore, "Superconducting nanowire photon-number-resolving detector at telecommunication wavelengths," *Nature Photon.*, vol. 2, no. 5, pp. 302–306, 2008.
- [52] O. Haderka, M. Hamar, and J. Perina, "Experimental multi-photon-resolving detector using a single avalanche photodiode," *Eur. Phys. J. D*, vol. 28, no. 1, p. 11, 2003.
- [53] P. P. Rohde, J. G. Webb, E. H. Huntington, and T. C. Ralph, "Photon number projection using non-number-resolving detectors," *New J. Phys.*, vol. 9, no. 7, pp. 233–233, 2007.

- [54] E. A. Dauler, A. J. Kerman, B. S. Robinson, J. K. W. Yang, B. Voronov, G. Goltsman, S. A. Hamilton, and K. K. Berggren, "Photon-number-resolution with sub-30-ps timing using multi-element superconducting nanowire single photon detectors," *J. Mod. Optic.*, vol. 56, no. 2, p. 13, 2008.
- [55] F. Marsili, V. B. Verma, J. A. Stern, S. Harrington, A. E. Lita, T. Gerrits, I. Vayshenker, and B. Baek, "Detecting Single Infrared Photons with 93% System Efficiency," *Nature Photon.*, vol. 7, pp. 210–214, 2013.
- [56] A. Verevkin, J. Zhang, R. Sobolewski, A. Lipatov, O. Okunev, G. Chulkova, A. Korneev, K. Smirnov, G. N. Goltsman, and A. Semenov, "Detection efficiency of large-active-area NbN single-photon superconducting detectors in the ultraviolet to near-infrared range," *Appl. Phys. Lett.*, vol. 80, no. 25, p. 4687, 2002.
- [57] M. J. Stevens, B. Baek, E. A. Dauler, A. J. Kerman, R. J. Molnar, S. A. Hamilton, K. K. Berggren, R. P. Mirin, and S. W. Nam, "High-order temporal coherences of chaotic and laser light." *Opt. Express*, vol. 18, no. 2, pp. 1430–7, 2010.
- [58] C. Zinoni, B. Alloing, L. H. Li, F. Marsili, A. Fiore, L. Lunghi, A. Gerardino, Y. B. Vakhtomin, K. V. Smirnov, and G. N. Goltsman, "Single-photon experiments at telecommunication wavelengths using nanowire superconducting detectors," *Appl. Phys. Lett.*, vol. 91, no. 3, p. 031106, 2007.
- [59] M. Halder, A. Beveratos, M. Gisin, V. Scarani, C. Simon, and H. Zbinden, "Entangling independent photons by time measurement," *Nat. Phys.*, vol. 3, pp. 692–695, 2007.
- [60] J. J. Renema, G. Frucci, M. J. A. de Dood, R. Gill, A. Fiore, and M. P. van Exter, "Tomography and state reconstruction with superconducting single-photon detectors," *Phys. Rev. A*, vol. 86, p. 062113, 2012.
- [61] R. H. Hadfield, J. L. Habif, J. Schlafer, R. E. Schwall, and S. W. Nam, "Quantum key distribution at 1550 nm with twin superconducting single-photon detectors," *Appl. Phys. Lett.*, vol. 89, no. 24, p. 241129, 2006.
- [62] N. Mohan, O. Minaeva, G. N. Goltsman, M. B. Nasr, B. E. Saleh, A. V. Sergienko, and M. C. Teich, "Photon-counting optical coherence-domain reflectometry using superconducting single-photon detectors." *Opt. Express*, vol. 16, no. 22, pp. 18 118–30, 2008.

- [63] S. N. Dorenbos, E. M. Reiger, U. Perinetti, V. Zwiller, T. Zijlstra, and T. M. Klapwijk, “Low noise superconducting single photon detectors on silicon,” *Appl. Phys. Lett.*, vol. 93, no. 13, p. 131101, 2008.
- [64] A. Annunziata, D. Santavicca, J. Chudow, L. Frunzio, M. Rooks, A. Frydman, and D. Prober, “Niobium Superconducting Nanowire Single-Photon Detectors,” *IEEE Trans. Appl. Supercond.*, vol. 19, no. 3, pp. 327–331, 2009.
- [65] F. Mattioli, M. Ejrnaes, A. Gaggero, A. Casaburi, R. Cristiano, S. Pagano, and R. Leoni, “Large area single photon detectors based on parallel configuration NbN nanowires,” *J. Vac. Sci. Technol.*, vol. 30, no. 031204, 2012.
- [66] J. Zhang, W. Slysz, A. Pearlman, A. Verevkin, R. Sobolewski, O. Okunev, G. Chulkova, and G. Goltsman, “Time delay of resistive-state formation in superconducting stripes excited by single optical photons,” *Phys. Rev. B*, vol. 67, no. 13, p. 132508, 2003.
- [67] J. J. Renema, G. Frucci, Z. Zhou, F. Mattioli, A. Gaggero, R. Leoni, M. J. A. de Dood, A. Fiore, and M. P. van Exter, “Modified detector tomography technique applied to a superconducting multiphoton nanodetector,” *Opt. Express*, vol. 20, no. 3, pp. 2806–2813, 2012.
- [68] K. Il'in, M. Lindgren, M. Currie, A. Semenov, G. Goltsman, R. Sobolevski, S. Cherednichenko, and E. Gershenzon, “Picosecond hot-electron energy relaxation in NbN superconducting photodetectors,” *Appl. Phys. Lett.*, vol. 76, p. 2752, 2000.
- [69] D. Rall, P. Probst, M. Hofherr, S. Wünsch, K. Il'in, U. Lemmer, and M. Siegel, “Energy relaxation time in NbN and YBCO thin films under optical irradiation,” *J. Phys.: Conference Series*, vol. 234, no. 4, p. 042029, 2010.
- [70] A. Gurevich and V. Vinokur, “Comment on: Vortex-assisted photon counts and their magnetic field dependence in single-photon superconducting detectors,” *Phys. Rev. B*, vol. 86, no. 2, p. 026501, 2012.
- [71] A. Gurevich and V. Vinokur, “Size Effects in the Nonlinear Resistance and Flux Creep in a Virtual Berezinskii-Kosterlitz-Thouless State of Superconducting Films,” *Phys. Rev. Lett.*, vol. 100, no. 22, p. 227007, 2008.
- [72] J. J. Renema, G. Frucci, Z. Zhou, F. Mattioli, A. Gaggero, R. Leoni, M. J. A. de Dood, A. Fiore, and M. P. van Exter, “Universal response curve for nanowire superconducting single-photon detectors,” *Phys. Rev. B*, vol. 87, p. 174526, 2013.

- [73] A. Engel, K. Inderbitzin, A. Schilling, R. Lusche, A. Semenov, D. Henrich, M. Hofherr, K. Il'in, and M. Siegel, "Temperature-dependence of detection efficiency in NbN and TaN SNSPD," *IEEE Trans. Appl. Supercond.*, vol. 23, no. 3, p. 2300505, 2013.
- [74] D. Y. Vodolazov, "Saddle point states in two-dimensional superconducting films biased near the depairing current," *Phys. Rev. B.*, vol. 85, p. 174507, 2012.
- [75] K. Suzuki, S. Shiki, M. Ukibe, M. Koike, S. Miki, Z. Wang, and M. Ohkubo, "Hot-Spot Detection Model in Superconducting Nano-Stripline Detector for keV Ions," *Appl. Phys. Expr.*, vol. 4, no. 8, p. 083101, 2011.
- [76] A. Verevkin, A. Pearlman, W. Slysz, J. Zhang, M. Currie, A. Korneev, G. Chulkova, O. Okunev, P. Kouminov, K. Smirnov, B. Voronov, G. Goltsman, and R. Sobolewski, "Ultrafast superconducting single-photon detectors for near-infrared-wavelength quantum communications," *J. Mod. Optic.*, vol. 51, no. 9-10, pp. 1447-1458, 2004.
- [77] T. Yamashita, S. Miki, W. Qiu, M. Fujiwara, M. Sasaki, and Z. Wang, "Temperature Dependent Performances of Superconducting Nanowire Single-Photon Detectors in an Ultralow-Temperature Region," *Appl. Phys. Expr.*, vol. 3, no. 10, p. 102502, 2010.
- [78] H. Bartolf, A. Engel, A. Schilling, K. Il'in, M. Siegel, H.-W. Hübers, and A. Semenov, "Current-assisted thermally activated flux liberation in ultrathin nanopatterned NbN superconducting meander structures," *Phys. Rev. B*, vol. 81, p. 024502, 2010.
- [79] A. Korneev, P. Kouminov, V. Matvienko, G. Chulkova, K. Smirnov, B. Voronov, G. N. Goltsman, M. Currie, W. Lo, K. Wilsher, J. Zhang, W. Slysz, A. Pearlman, A. Verevkin, and R. Sobolewski, "Sensitivity and gigahertz counting performance of NbN superconducting single-photon detectors," *Appl. Phys. Lett.*, vol. 84, no. 26, p. 5338, 2004.
- [80] A. Korneev, V. Matvienko, O. Minaeva, I. Milnostnaya, I. Rubtsova, G. Chulkova, K. Smirnov, V. Voronov, G. Goltsman, W. Slysz, A. Pearlman, A. Verevkin, and R. Sobolewski, "Quantum efficiency and noise equivalent power of nanostructured, NbN, single-photon detectors in the wavelength range from visible to infrared," *IEEE Trans. Appl. Supercond.*, vol. 101, pp. 49-54, 2005.
- [81] R. Lusche, A. Semenov, K. Il'in, Y. Korneeva, A. Trifonov, A. Korneev, H.-W. Hübers, M. Siegel, and G. Goltsman, "Effect of the wire width and magnetic field on the intrinsic detection efficiency of superconducting nanowire single-photon detectors," *IEEE Trans. Appl. Supercond.*, vol. 23, 2013.

- [82] A. Kadin, M. Leung, and A. Smith, "Photon-assisted vortex depairing in two-dimensional superconductors," *Phys. Rev. Lett.*, vol. 65, p. 3193, 1990.
- [83] H. B. Coldenstrodtt-Ronge, J. S. Lundeen, K. L. Pagnell, A. Feito, B. J. Smith, W. Maurer, C. Silberhorn, J. Eisert, M. B. Plenio, and I. A. Walmsley, "A proposed testbed for detector tomography," *J. Mod. Optic.*, vol. 56, no. 2-3, pp. 432-441, 2009.
- [84] K. Il'in, D. Rall, M. Siegel, A. Engel, A. Schilling, A. Semenov, and H. Huebers, "Influence of thickness, width and temperature on critical current density of Nb thin film structures," *Physica C*, vol. 470, p. 953, 2010.
- [85] K. Inderbitzin, A. Engel, and A. Schilling, "Soft x-ray single-photon detection with superconducting tantalum nitride and niobium nanowires," *IEEE Trans. Appl. Supercond.*, vol. 23, p. 2200505, 2013.
- [86] K. Burnham and D. Anderson, *Model selection and multimodel inference*. Springer, 1998.
- [87] A. Kerman, D. Rosenberg, R. Molnar, and E. Dauler, "Readout of Superconducting nanowire single-photon detectors at high count rates," *J. Appl. Phys.*, vol. 113, p. 144511, 2013.
- [88] E. Reiger, S. Dorenbos, V. Zwiller, A. Korneev, G. Chulkova, I. Milostnaya, O. Minaeva, G. Gol'tsman, J. Kitaygorsky, D. Pan *et al.*, "Spectroscopy with nanostructured superconducting single photon detectors," *IEEE J. Sel. Top. Quantum Electron.*, vol. 13, no. 4, pp. 934-943, 2007.
- [89] C. M. Natarajan, A. Peruzzo, S. Miki, M. Sasaki, Z. Wang, B. Baek, S. Nam, R. H. Hadfield, and J. L. O'Brien, "Operating quantum waveguide circuits with superconducting single-photon detectors," *Appl. Phys. Lett.*, vol. 96, no. 21, p. 211101, 2010.
- [90] H. Takesue, S. Nam, Q. Zhang, R. Hadfield, T. Honjo, K. Tamaki, and Y. Yamamoto, "Quantum key distribution over a 40-dB channel loss using superconducting single-photon detectors," *Nature Photon.*, vol. 1, p. 343, 2007.
- [91] N. Gemmill, A. McCarthy, B. Liu, M. Tanner, S. Dorenbos, V. Zwiller, M. Paterson, G. Buller, B. Wilson, and H. R.H., "Singlet oxygen luminescence detection with a fiber-coupled superconducting nanowire single-photon detector," *Opt. Express*, vol. 21, p. 5005, 2013.
- [92] T. Yamashita, S. Miki, H. Terai, and Z. Wang, "Low-filling-factor superconducting single photon detector with high system detection efficiency," *Opt. Express*, vol. 22, p. 27122, 2013.

- [93] L. Maingault, P. Cavalier, R. Lamaestre, L. Frey, and J. Villegier, "Quantum efficiency and polarization effects in nbn superconducting single photon detectors," *Proc. ASC 2008 in IEEE Trans. Appl. Supercond.*, 2008.
- [94] D. Sahin, A. Gaggero, Z. Zhou, S. Jahanmirinejad, F. Mattioli, R. Leoni, J. Beetz, M. Lermer, M. Kamp, S. Höfling, and A. Fiore, "Waveguide photon-number-resolving detectors for quantum photonic integrated circuits," *Applied Physics Letters*, vol. 103, no. 11, p. 111116, 2013.
- [95] C. Natarajan, L. Zhang, H. Coldenstrodt-Ronge, G. Donati, S. Dorenbos, V. Zwiller, I. Walmsley, and R. Hadfield, "Quantum detector tomography of a time-multiplexed superconducting nanowire single-photon detector at telecom wavelengths," *Opt. Express*, vol. 21, pp. 893–902, 2013.
- [96] D. Sahin, "Waveguide single-photon and photon-number resolving detectors," Ph.D. dissertation, University of Eindhoven, 2014.
- [97] M. Tinkham, *Introduction to superconductivity*. McGraw-Hill, 1996.
- [98] A. N. Tikhonov, "On the stability of inverse problems," *Dokl. Akad. Nauk SSSR*, vol. 39, no. 5, pp. 195–198, 1943.
- [99] V. B. Verma, A. E. Lita, M. R. Vissers, F. Marsili, D. Pappas, R. Mirin, and S. W. Nam, "Superconducting nanowire single photon detectors fabricated from an amorphous $\text{Mo}_{0.75}\text{Ge}_{0.25}$ thin film," *arXiv:1402.4526*.
- [100] Y. P. Korneeva, M. Y. Mikhailov, Y. P. Pershin, N. N. Manova, A. V. Divochiy, Y. B. Vakhtomin, A. A. Korneev, K. V. Smirnov, A. G. Sivakov, A. Y. Devizenko, and G. N. Goltsman, "Superconducting single-photon detector made of MoSi film," *Superconductor Science and Technology*, vol. 27, no. 9, p. 095012, 2014.
- [101] H. Shibata, "Fabrication of a MgB_2 nanowire single-photon detector using $\text{Br}_2\text{-N}_2$ dry etching," *Appl. Phys. Expr.*, vol. 7, no. 10, p. 103101, 2014.
- [102] A. Eftekharian, H. Atikian, M. Akhlagi, A. Jafari Salim, and A. Hamed Majedi, "Quantum ground state effect on fluctuation rates in nano-patterned superconducting structures," *Appl. Phys. Lett.*, vol. 103, p. 242601, 2013.
- [103] A. Engel, A. Schilling, K. Il'in, and M. Siegel, "Dependence of count rate on magnetic field in superconducting thin-film TaN single-photon detectors," *Phys. Rev. B*, vol. 86, p. 140506, 2012.

- [104] A. Anthore, H. Pothier, and D. Esteve, “Density of states in a superconductor carrying a supercurrent,” *Phys. Rev. Lett.*, vol. 90, p. 127001, 2003.
- [105] K. D. Usadel, “Generalized diffusion equation for superconducting alloys,” *Phys. Rev. Lett.*, vol. 25, pp. 507–509, 1970.
- [106] “Quantum design application note 1070-207: Using PPMS superconducting magnets at low fields.”
- [107] E. F. C. Driessen, P. C. J. J. Coumou, R. R. Tromp, P. J. de Visser, and T. M. Klapwijk, “Strongly disordered TiN and NbTiN *s*-wave superconductors probed by microwave electrodynamics,” *Phys. Rev. Lett.*, vol. 109, p. 107003, 2012.
- [108] P. C. J. J. Coumou, E. F. C. Driessen, J. Bueno, C. Chapelier, and T. M. Klapwijk, “Electrodynamic response and local tunneling spectroscopy of strongly disordered superconducting tin films,” *Phys. Rev. B*, vol. 88, p. 180505, 2013.
- [109] B. Plourde, D. van Harlingen, D. Y. Vodolazov, R. Besselink, M. Hesselberth, and P. H. Kes, “Influence of edge barriers on vortex dynamics in thin weak-pinning superconducting strips,” *Phys. Rev. B*, vol. 64, p. 014503, 2011.
- [110] K. Il’in and M. Siegel, “Magnetic field stimulated enhancement of the barrier for vortex penetration in bended bridges of thin TaN films,” *Physica C*, vol. 503, pp. 58–61, 2014.
- [111] G. Stan, S. B. Field, and J. M. Martinis, “Critical field for complete vortex expulsion from narrow superconducting strips,” *Phys. Rev. Lett.*, vol. 92, p. 097003, 2004.
- [112] K. Il’in, D. Heinrich, Y. Luck, Y. Liang, and M. Siegel, “Critical current of Nb, NbN and TaN thin-film bridges with and without geometrical nonuniformities in a magnetic field,” *Phys. Rev. B*, vol. 89, p. 184511, 2014.
- [113] B. Sacépé, C. Chapelier, T. I. Baturina, V. M. Vinokur, M. R. Baklanov, and M. Sanquer, “Disorder-induced inhomogeneities of the superconducting state close to the superconductor-insulator transition,” *Phys. Rev. Lett.*, vol. 101, p. 157006, 2008.
- [114] Y. Noat, V. Cherkez, C. Brun, T. Cren, C. Carbillet, F. Debontridder, K. Il’in, M. Siegel, A. Semenov, H.-W. Hübbers, and D. Roditchev, “Unconventional superconductivity in ultrathin superconducting NbN films studied by scanning tunneling spectroscopy,” *Phys. Rev. B*, vol. 88, p. 014503, 2013.

- [115] J. Bueno, P. C. J. J. Coumou, G. Zheng, P. J. de Visser, T. M. Klapwijk, E. F. C. Driessen, S. Doyle, and J. J. A. Baselmans, "Anomalous response of superconducting titanium nitride resonators to terahertz radiation," *Applied Physics Letters*, vol. 105, no. 19, pp. –, 2014.
- [116] G. Berdiyrov, M. Milosevic, and F. Peeters, "Spatially dependent sensitivity of superconducting meanders as single-photon detectors," *Appl. Phys. Lett.*, vol. 100, p. 262603, 2012.
- [117] D. Henrich, L. Rehm, S. Dorner, M. Hofherr, K. Il'in, A. Semenov, and M. Siegel, "Detection efficiency of a spiral-nanowire superconducting single-photon detector," *IEEE Trans. Appl. Supercond.*, vol. 23, no. 3, pp. 2 200 405–2 200 405, 2013.
- [118] Q. Wang and M. J. de Dood, "An absorption-based superconducting nano-detector as a near-field optical probe," *Opt. Express*, vol. 21, p. 3682, 2013.
- [119] A. Jukna, J. Kitaygorsky, D. Pan, A. Cross, A. Perlman, I. Komissarov, O. Okunev, K. Smirnov, A. Korneev, G. Chulkova *et al.*, "Dynamics of hotspot formation in nanostructured superconducting stripes excited with single photons," *Acta. Phys. Pol. A*, vol. 113, no. 3, pp. 955–958, 2008.
- [120] A. Semenov, A. Engel, K. Il'in, G. Gol'tsman, M. Siegel, and H.-W. Hübers, "Ultimate performance of a superconducting quantum detector," *Eur. Phys. J. Appl. Phys.*, vol. 21, no. 03, pp. 171–178, 2003.
- [121] R. Gaudio, K. op 't Hoog, Z. Zhou, D. Sahin, and A. Fiore, "Inhomogeneous critical current in nanowire superconducting single-photon detectors," *Submitted to Appl. Phys. Lett.*, 2014.
- [122] S. P. Chockalingam, M. Chand, J. Jesudasan, V. Tripathi, and P. Raychaudhuri, "Superconducting properties and hall effect of epitaxial NbN thin films," *Phys. Rev. B*, vol. 77, p. 214503, 2008.
- [123] F. Marsili, M. J. Stevens, A. Kozorezov, V. B. Verma, C. Lambert, J. A. Stern, R. Horansky, S. D. Dyer, M. D. Shaw, R. P. Mirin *et al.*, "Hotspot dynamics in current carrying wsi superconducting nanowires," in *CLEO: QELS_Fundamental Science*. Optical Society of America, 2014, pp. FM4B–7.

Index

- Critical current, 9, 42, 105
 - Criterion, 95
 - Current crowding, 10, 74, 94
 - Enhancement by vortices, 101
 - Magnetic field dependence, 101
 - Temperature dependence, 8, 45
- Dark counts, 34, 94, 101, 102
 - Comparison with photon counts, 27, 42, 102
 - Comparison with theory, 91
- Detection models in SSPDs, 3, 38
 - Comparison between Normal-state and Diffusion-based vortex models, 9, 68, 118
 - Comparison with experiments, 30, 36, 42
 - Comparison with literature, 36
 - Diffusion-based hotspot model, 4, 36, 42, 117
 - Diffusion-based vortex model, 7, 42, 74, 110
 - Energy-current relation of various models, 4
 - Normal-core hotspot model, 3, 36, 42, 104, 117
 - Normal-state vortex model, 9, 42, 68, 113
- Energy-current relation, 3, 91
 - Diffusion-based hotspot model, 5
 - Diffusion-based vortex model, 8
 - Measurements of, 30, 42
 - Microscopic, 64, 66
 - Normal-core hotspot model, 4
 - Normal-state vortex model, 9
 - Numerical computation, 76
 - Other materials, 118
 - Role of threshold criterion, 89
- Hotspot size, 52, 103
 - As function of bias current, 109
 - As function of wavelength, 110
 - Derivation of formula used to measure, 106
 - Measurement, 108
- Linear efficiency, 40
 - Comparison to semiclassical efficiency, 21
- Magnetic field response
 - As a test of the models, 118
 - Comparison to theory, 99
 - High-field response, 99
 - Low-field regime, 95
 - passim*, 94
- Multiphoton excitations
 - Advantages, 33
 - Equivalence to single-photon excitations, 40
 - Internal position dependence of, 72
 - Introduction to, 11
- Nanodetector
 - Advantages, 12, 32
 - Comparison with meander, 42
 - Introduction to, 12
 - Role of inhomogeneous form, 52, 77, 108, 111
- NbN

- Comparison with WSi, 102, 113
- Deposition conditions, 105
- intrinsic pair breaker, 99
- sheet resistance, 95
- Numerical simulations
 - Energy-current relation, 76
 - Of the internal detection event, 8, 9, 74
 - Of the polarization dependence, 81
 - Optical absorption, 77
- Position-dependent internal detection efficiency, 60
 - Computation, 81
 - Examples, 83
 - Experimental resolution, 82
 - Implications for macroscopic properties, 86
 - passim*, 59
 - Relation with overall detection efficiency, 91
- Quantum detector tomography, 69, 107
 - Accuracy, 51, 55
 - Akaike Criterion, 47
 - Comparison to Karlsruhe rolloff formula, 52
 - Comparison with semiclassical results, 50
 - Derivation, 18
 - Example, 49
 - Introduction to, 10
 - Model selection, 20, 22, 47
 - Role of dynamic range, 70
 - Role of threshold criterion, 40, 89
 - Separation between p_i and η , 20, 71
- Reference current, 40, 64, 90
 - Comparison between theory and experiment, 90
 - Temperature dependence of, 45
- Substrate, 56, 77
- Superconducting Single-Photon Detectors
 - Applications, 25
 - As ion/x-ray detectors, 45
 - As spectrometers, 54
 - Comparison with other detectors, 1
 - Electro-thermal mechanism, 10
 - Introduction to, 1
 - Optical properties of, 10, 60, 77
 - Slow roll-off, 64, 87
 - Timescales in, 27, 110
- Temperature dependence, 38
 - Comparison to literature, 52
 - Diffusion-based hotspot model, 5
 - Diffusion-based vortex model, 8
 - Of the magnetic field response, 98
- Universal curve, 30, 64, 88, 107
- Vortices, 6, 118
 - Diffusion-based vortex model, 7
 - Edge barrier, 7, 75
 - Entry at high magnetic field, 101
 - Forces on, 7
 - Normal-state vortex model, 9
 - Temperature-dependence of entry energy, 45
- Width dependence, 42, 118
- WSi, 113, 118